博　士　論　文

Rheology and Structure of Model Smectite Clay Using Molecular Dynamics
(分子動力学法を用いたスメクタイト粘土モデルのレオロジーと構造)

2024 年 7 月

大阪大学大学院理学研究科宇宙地球科学専攻
林 朱元

Contents

Abstract

Smectite clay is commonly found in the shallow part of the upper crust and plays a critical role in controlling the rheology and stability of clay-rich faults. Despite extensive studies on its frictional properties and fabric development, the underlying mechanisms are not fully understood. While shear experiments characterize smectite clay as frictionally stable, field observations and clay suspension experiments reveal conditional instability. It is crucial to examine whether the clay system can exhibit instability under varying conditions.

Given smectite clay's ability to carry charge and absorb water, conventional understanding based on friction at the contact surface may not fully explain its shear resistance. A particle-level study on the microscopic shear mechanism can provide deeper insights into the macroscopic behavior of clay-rich faults. In this study, we perform shear simulations on a model clay system using molecular dynamics, where clay platelets are simplified as oblate ellipsoids interacting via the Gay-Berne potential. The primary aim is to investigate the effect of different factors on the rheology and structure of the model clay system, focusing on strain rate, normal stress, and energy anisotropy.

The current model successfully reproduces key features of the clay system in both rheology and structure and captures unstable flow behavior under various scenarios. The 3D clay system shows velocity-strengthening behavior, which can be described by the Herschel-Bulkley model. Shear banding occurs at low strain rates, with particles in the shear zone aligning in a preferred orientation. The result suggest that the clay-rich faults are predominantly controlled by a thin shear band at realistic strain rates. The system's structure can be quantitatively described by nematic order and the parallel radial distribution function. At low strain rates, the structural development occurs in two stages: particles rearrange to align with shear as shear stress increases to the peak, followed by shear banding as shear stress reaches a steady-state value. The shear process in the simulation is consistent with experimental observations.

In a 2D clay system under high normal stress, a similar structure and rheology to the 3D system are observed. However, at low normal stress, shear is characterized by the collective movement of clusters, which results in significant fluctuations in volume and particle alignment. Stable shear bands form at much lower strain rates in the 2D system, and intermediate strain rates are governed by long-lived fluctuating nonlinear velocity profiles. Higher energy anisotropy enhances shear resistance but also promotes cluster formation.

We also tested the instability of a confined 2D clay system with a moving upper plate. The system exhibited clear stick-slip motion together with global velocity-strengthening behavior. The stress peak during stick-slip is close to the static yield stress. Increasing normal stress results in a decreasing stress drop. Wall slip near the upper plate is observed at low normal

stress, and the shear zone is wider at higher normal stress.

Our results suggest that the typical characteristics of clay gouge, including velocity-strengthening behavior and fabric development during shear, can be observed in this simple model clay system. The shear behavior of clay can be described using a yield stress fluid model, beyond conventional considerations of sliding friction. Despite a monotonic global flow curve showing that the shear stress increases with finite strain rates, the model clay system can exhibit instability, including shear banding and stick-slip motion at low strain rate and during shear startup.

List of Symbol

This list of symbols is not exhaustive. Symbols that only appear locally in the text are not included here.

Roman Symbol

a	Frictional parameter
B	Characteristic stacking size
b	Frictional parameter
d_c	Characteristic slip distance
E_k	Kinetic energy
$g^{\parallel}$	Parallel radial distribution function
h_{12}	Approximated distance between two interacting ellipsoids
K	Herschel-Bulkley model parameter
k	Spring stiffness
k_B	Boltzmann constant
L_{band}	Shear band thickness
L_x	The X dimension of the simulation cell
L_y	The Y dimension of the simulation cell
L_z	The Z dimension of the simulation cell
m	Particle mass
m_0	Mass unit
N	Number of particles
N_{upper}	Number of particles in the upper plate
n	Herschel-Bulkley model parameter
n_p	Porosity
P	System pressure
P_f	Pore fluid pressure
T	System temperature
Q	Orientation tensor
R^2	Coefficient of determination
r, r_{ij}	Center-to-center distance between particles
S	Nematic order parameter
U	Potential Energy
$\boldsymbol{u}_i$	Unit vector long the symmetry axis of

	particle i
V	System volume
v_{pl}	Spring pulling velocity on upper plate
v_x, v_y, v_z	Linear velocity of particle in X, Y, and Z direction
x_i, y_i, z_i	Coordinates of particle i

Greek symbol

α	Rheology parameter
β	Rheology parameter
γ	Shear strain
$\dot{\gamma}$	Strain rate
δt	Time step
ϵ_0	Energy unit
θ	Particle orientation
κ	Aspect ratio
κ'	Energy ratio
λ	Structural parameter
μ	Coefficient of friction
τ	Shear stress
τ_y, σ_y	Yield stress
τ_0	Time unit
σ_0	Length unit
σ_{eff}	Effective normal stress
σ_{ee}	Diameter of the ellipsoid clay particle
σ_{ff}	Thickness of the ellipsoid clay particle
σ_n	Normal stress
σ_y^s	Static yield stress
φ	Volume fraction

1 Introduction

1.1 Earthquake as unstable slip

1.1.1 Earthquake

Earthquakes occur due to the stress accumulation in fault zones. When this stress reaches a critical point, the fault slips suddenly, releasing the energy as seismic waves, which cause the shaking we can feel on the ground. Japan is located at the intersection of four tectonic plates: the Eurasian Plate, the North American Plate, the Pacific Plate, and the Philippine Sea Plate. The frequent earthquakes in this region result from the relative motion of these tectonic plates. Slip events along plate boundaries such as the subduction megathrust can be especially dangerous and can generate large magnitude earthquakes and other secondary disasters. For example, during the 2011 Tohoku-Oki Earthquake, a large slip occurred in the shallow part of the subduction zone, triggering a devastating tsunami (Chester et al., 2013). Since the rheology and strength of a fault is governed by the gouge material, understand the frictional properties of different geomaterials is crucial for understanding and predicting hazardous events such as large slips and earthquakes.

1.1.2 Rock friction

The formation of fault is governed by the shear failure of rocks, which can be described by the Coulomb criterion (Anderson, 1905):

$$\tau = C_0 + \mu\sigma_{eff}, \sigma_{eff} = \sigma_n - P_f \quad (1.1)$$

where τ is the shear stress, C_0 is the cohesion strength, μ is the friction coefficient, σ_{eff} is the effective normal stress, σ_n is the normal stress and P_f is the pore pressure. Assuming the cohesion is relatively small compared to shear stress and normal stress, it is often neglected after significant displacement, simplifying the shear stress equation to:

$$\tau = \mu_{ss}\,\sigma_{eff} \quad (1.2)$$

where μ_{ss} is the steady sliding friction coefficient. Extensive studies on various rock types, gouge materials, and surface roughness have been performed to determine the friction coefficient in different faults. Laboratory friction measurements summarized by Byerlee (1978) indicate that the friction ranges from 0.6~0.85, independent of rock type. This friction range, known as the Byerlee's law, has been supported by various field observations on angle (dip) of the fault and stress state measurements (Sibson, 1985; Collettini and Sibson, 2001).

1.1.3 Stable and unstable slip

Change in frictional resistance during shear can lead to unstable slip. This dynamic

instability can occur repetitively with stress accumulation in stationary stick phase followed by a sudden slip with stress drop in slip stage. This regular stick-slip motion can be captured using a block-slider model where the load is applied through a spring with constant stiffness k. The stiffness k may represent the elastic properties of the fault zone environment and is associated with the size of the local slip region.

In this model, the frictional force first reaches a maximum and then decreases when the slip begins. Simultaneously, the load force applied by the spring decreases with a slope of -k. If the reduction in resistance force F with slip distance u is faster than -k, the force imbalance will accelerate the sliding motion, resulting in an unstable slip. The condition of instability is $\left|\frac{\partial F}{\partial u}\right| > k$, which is controlled by both the frictional properties of the slider and the elastic properties of the loading environment. Stick-slip behavior in rocks is frequently observed in friction experiments and is considered to be the mechanism of earthquake (Brace and Byerlee, 1966).

The earthquakes can be seen as stick-slip events characterized by repeating instability on preexisting faults. Subsequent studies have shown that the stick-slip behavior is commonly observed when the friction has a negative velocity dependence, a behavior known as velocity weakening (Rabinowicz, 1965).

1.1.4 Rate and state dependent friction

The theory of rate and state dependent friction (RSF) is widely adopted in modern earthquake studies (Dieterich, 1978; Ruina, 1983, Perrin et al., 1995). Based on laboratory experiments, this empirical theory can reproduce the transient frictional changes in response to step changes in sliding velocity as shown in Figure 1.1. A Dieterich type formulation is expressed as follows (Marone, 1998):

$$\tau = \mu\sigma_{eff} = \left[\mu_0 + aln\left(\frac{V}{V_0}\right) + bln\left(\frac{V_0\theta}{d_c}\right)\right]\sigma_{eff}, \qquad \frac{d\theta}{dt} = 1 - \frac{V\theta}{d_c} \tag{1.3}$$

where θ is an internal state variable, the parameter a describes the instantaneous change in shear stress when the velocity changes from a value V_0 to V, b describes the change in friction during the subsequent evolution to a new steady state over a critical distance d_c, and μ_0 is the friction coefficient at the velocity of V_0.

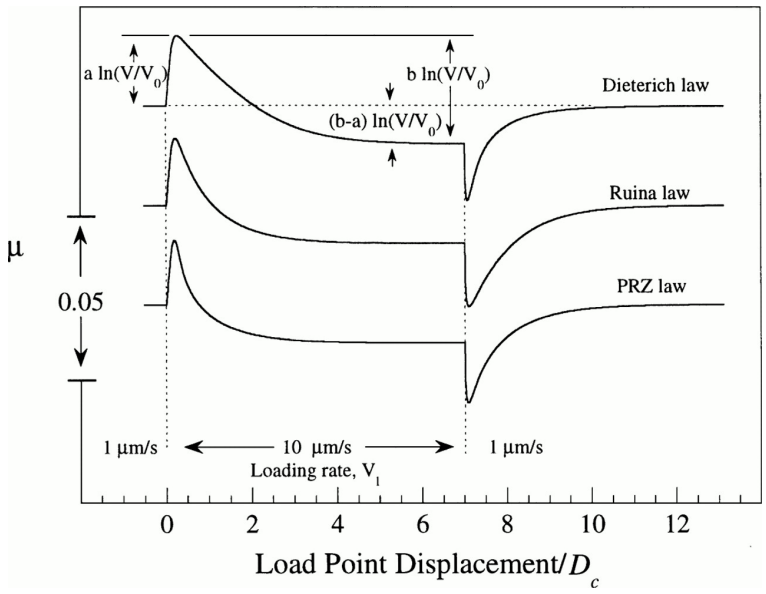

Figure 1.1: Friction vs. normalized displacement for different rate and state friction laws. (Marone, 1998)

At steady state $(d\theta/dt = 0)$, $\theta_{ss}(V) = d_c/V$. The steady state shear stress is then:

$$\tau = \left[\mu_0 + (a-b)ln\left(\frac{V}{V_0}\right)\right]\sigma_{eff} \tag{1.4}$$

A Stepwise change in velocity results in a change in shear stress at controlled effective normal stress, which gives:

$$(a-b) = \frac{\Delta\mu_{ss}}{ln\left(\frac{V_2}{V_1}\right)} = \frac{\Delta\mu_{ss}}{\Delta lnV} \tag{1.5}$$

The value of (a-b) describes the velocity dependence of the friction coefficient. A positive value indicates the friction coefficient increases with increasing stress (velocity-strengthening), which implies greater shear resistance during acceleration, preventing the nucleation of unstable slip. Conversely, a negative value indicates decreasing friction with increasing velocity (velocity-weakening), which can lead to slip instability and is associated with the nucleation of earthquake.

1.2 Smectite clay

1.2.1 Importance of clay minerals

Clay minerals are stable byproduct from chemical weathering of various primary minerals on the Earth's surface. Smectite clay, such as montmorillonite, is abundant in the top part of the upper crust and is commonly found in shallow subduction zones (Carpenter et al., 2011; Collettini et al., 2019; Deng and Underwood, 2001; Ikari et al., 2011; Jeppson and Tobin 2015;

Lockner et al., 2011; Wojatschke et al., 2016; Wu et al., 1975). Drilling investigation in the slipped region of the 2011 Tohoku-Oki earthquake revealed that the fault zone consists of about 80% clay minerals, mainly smectite (Kameda et al., 2016). Smectite clay is thought to play a crucial role in controlling tectonic phenomena, particularly in shallow subduction systems, such as determining the location of seismic and aseismic zones (Saffer and Marone, 2003; Okuda et al., 2023). The low frictional strength and low rigidity of clay-rich sediments has been considered in explaining different fault slip motions in subduction zone, from slow rupture processes to propagation of large earthquakes (Ito and Obara, 2006; Behnsen and Faulkner, 2013; Volpe et al., 2024). Therefore, systematic studies on the rheological behavior of clay-water systems are essential to understanding different slip events at shallow depths.

1.2.2 Clay types

Clay is a type of phyllosilicate mineral with a layered sheet structure (Mitchell and Soga, 2005). The basic structure of clay consists of silicate tetrahedral sheets $[Si_2O_5]^{2-}$ (T) and gibbsite octahedral sheets $[Al(OH)_3]$ (O) (Figure 1.2). The two kinds of sheets are connected by substituting two hydroxyl ions (OH) in octahedral sheet with Oxygens and share the Oxygens with the tetrahedral sheet. Different types of clay vary in their stacking sequences, cation substitutions and bonding characteristics.

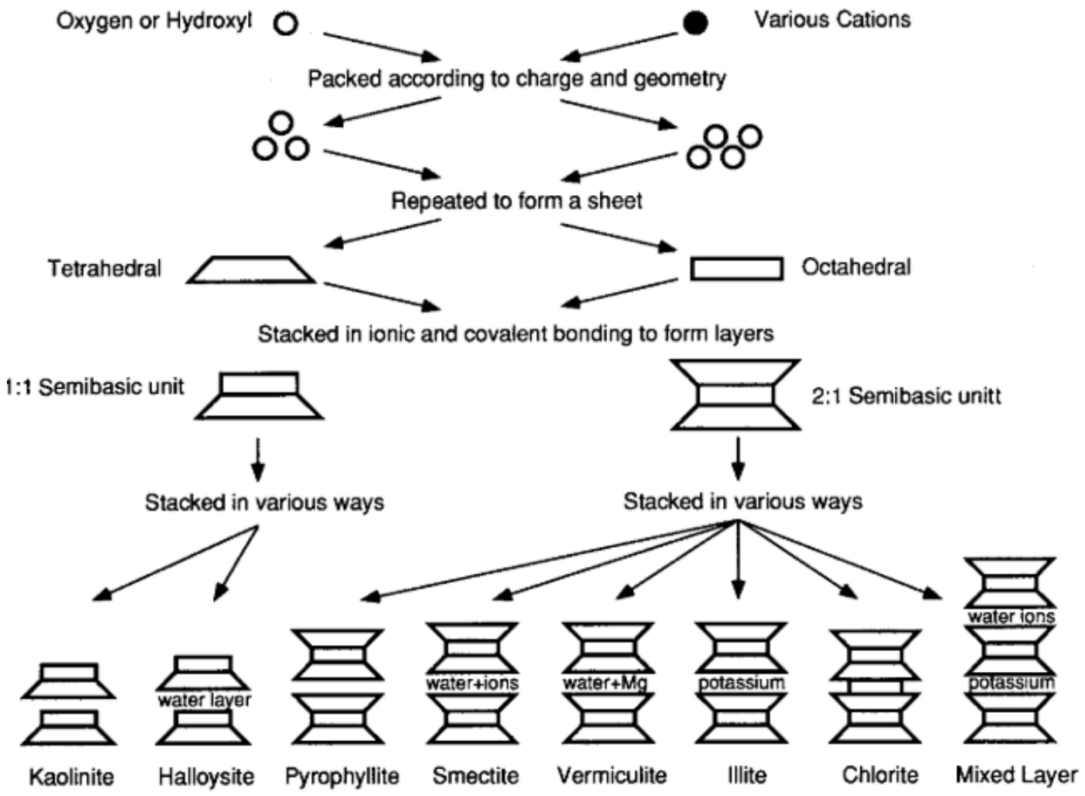

Figure 1.2: The structure of different clay minerals (Mitchell and Soga, 2005)

1.2.3 Structure and size of smectite clay

The Smectite clay is a type of 2:1 clay mineral, characterized by a T-O-T structure, which consists of one octahedral sheet sandwiched between two tetrahedral sheets. The most common type of smectite is montmorillonite.

The charge-carry ability of smectite clay result from cation substitutions, with Al^{3+} substituting Si^{4+} in the tetrahedral sheet and Mg^{2+} or Fe^{2+} substituting Al^{3+} in the octahedral sheet. This creates an overall negative charge on the clay surface, which can be balanced by exchangeable cations between the layers (Emmerich et al., 2009). For montmorillonites, the spacing between charged surface can be widen, allowing water molecules to enter the interlayer space and form structured water layers. Macroscopically, this causes the mineral to swell significantly (Ho et al., 2019).

The thickness of montmorillonite, characterized by its T-O-T structure, is 0.95 nm. During hydration, the basal interlayer spacing (d-spacing) increase by about 0.3 nm for every water layer formed in interlayer space (Shen and Bourg, 2021). The size of the clay in laboratory experiments is often measured in the extending diameter direction (Segad et al., 2012). With a fixed thickness, clay can have a wide size distribution ranging from 5 to 750 nm with an average size of 250 nm (Michot et al., 2004). Commercial montmorillonite and bentonite are commonly used in shear experiments. Moore and Lockner (2007) reported using montmorillonite with diameters generally less than 500 nm, while Haines et al. (2009) used crashed montmorillonite with a mean size of 83 um under unsaturated condition. Observations on individual Na-montmorillonite platelets show that their shapes are highly irregular (Cadene et al., 2005).

1.2.4 Smectite clay interaction

The classical description of clay interactions is based on the Derjaguin–Landau–Verwey–Overbeek (DLVO) theory, which models charged parallel planes and involves van der Waals attraction and electrostatic diffuse double layer repulsion (Derjaguin 1941; Verwey, 1947). The DLVO model has been successful in qualitatively explaining some behaviors in clayey soils and clay suspensions (Gupta, 2011; Mitchell and Soga, 2005). However, it simplifies interactions by using a mean field approximation and neglects detailed interactions among ions, water molecules and clay surfaces. Experimental observations indicate that the DLVO model becomes increasing inaccurate at short distance (Gilbert et al., 2015; Guven, 1992; Quirk, 1986). It fails to account for the short-range repulsion and the highly structured water layers (Ebrahimi et al., 2014).

This limitation has been addressed in subsequent studies, such as the primitive model, which considers ion density fluctuations between two plates that is neglected in the DLVO model (Pellenq et al., 1997; Carrier et al., 2013). The primitive model assumes structureless charged planes immersed in a bath of counter-ions within a dielectric continuum. It predicts the attraction through ion correlation force for colloidal particles of the same charge, which explains the flocculation and tactoid formation in clay suspension. Carrier (2013) demonstrated that an explicit primitive model is able to replicate the result from full atomistic molecular dynamics simulations.

1.2.5 Microstructure formed by smectite clay

Clay interactions can lead to the formation of various microstructures. Clay platelets tend to stack face-to-face, forming tactoids consisting of 3-8 single platelets (Segad et al., 2012). At low volume fractions in clay suspensions, larger scale structures such as aggregation and gel network can also formed (Michot et al., 2004; Mouzon et al., 2016). Fukukawa et al. (2009) demonstrated that the size of montmorillonite aggregates can reach up to 1200 nm in artificial seawater.

In shear experiments at high normal stress and low water content, aggregation or large structure cannot be clearly identified after shear from scanning electron microscope (SEM) images (Haines et al., 2013, Moore and Lockner, 2007).

1.3 Frictional properties of smectite clay

1.3.1 Friction of smectite clay

Phyllosilicate minerals exhibit lower friction coefficients ranging from 0 to 0.3, in contract to the range of 0.6~0.85 predicted by the Byerlee's law (Colletini et al., 2019). Field observations indicate that faults rich in phyllosilicate display distinct deformation features diverging from faults controlled by strong minerals (Colletini et al., 2019; Tesei et al., 2013; Faulkner et al., 2003). For instance, deformation in mature faults often localizes within interconnected phyllosilicate zones and exhibits relatively low dip angles (Faulkner et al., 2003).

Recent summaries on laboratory data shows the sample saturation and the experimental procedures have critical influences on measuring the friction properties of montmorillonite, as depicted in Figure 1.3 (Morrow et al., 2017). The friction coefficient increases with effective normal stress within the range of 0.1~0.3 when montmorillonite is fully saturated (the pore pressure must be well controlled during shear). Conversely, under dry, unsaturated, and overpressure conditions, friction coefficient can be in a higher range 0.2~0.6 and typically

decreases with normal stress, albeit the value is still lower than the Byerlee's law. Mixing different types of clay with stronger minerals generally decreases the overall friction with higher clay content (Tembe et al., 2010; Ashman and Faulkner, 2023)

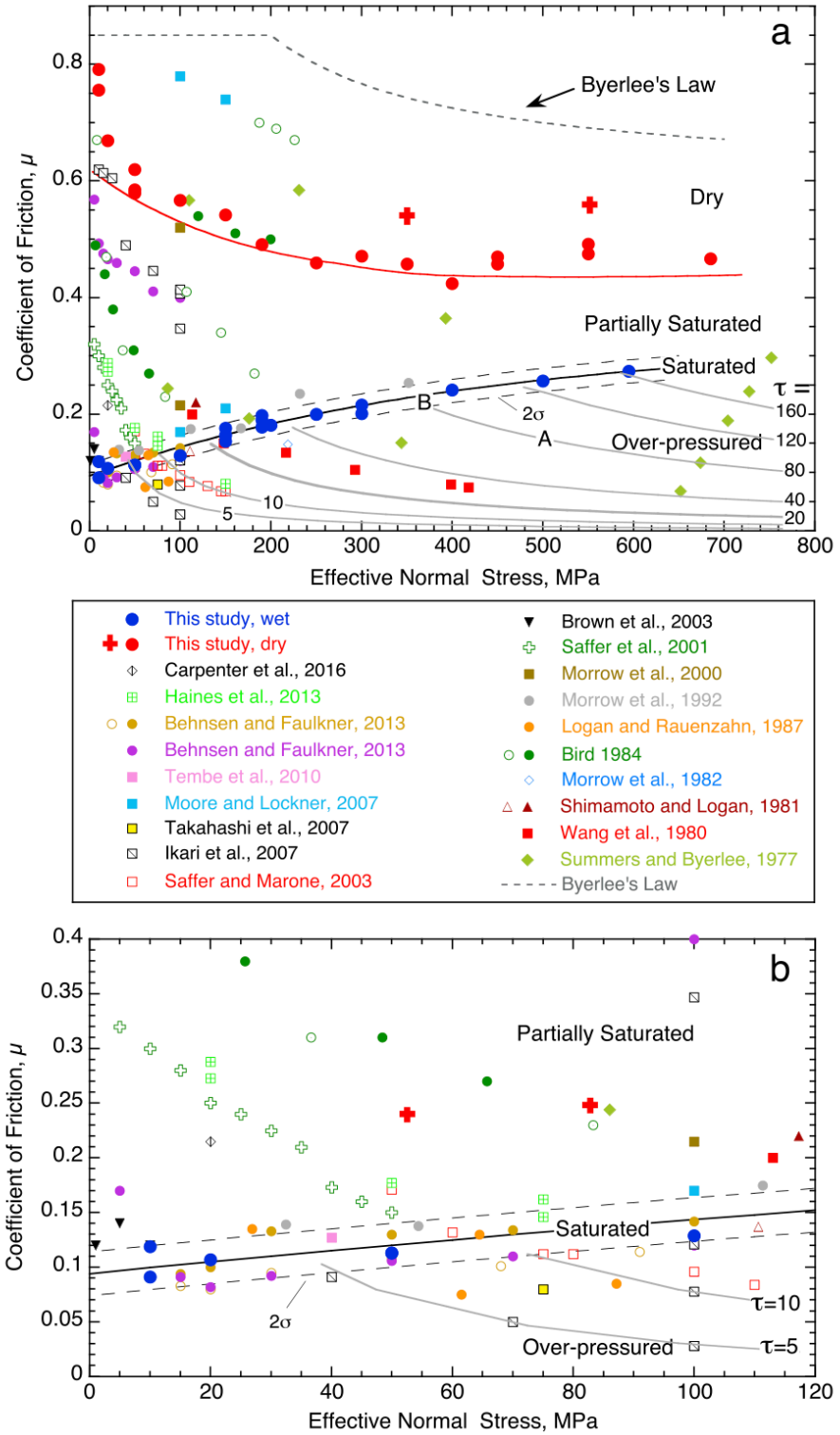

Figure 1.3: Coefficient of friction of montmorillonite (Morrow et al., 2017)

1.3.2 Velocity dependence of smectite clay

Montmorillonite typically exhibits velocity-strengthening behavior with a positive (a-b) in shear experiments. Under dry conditions, the value ranges from 0.004 to 0.009 for normal stress below 100 MPa (Morrow et al., 2017; Ikari et al., 2007), whereas the value decrease to a range of 0 to 0.001 under saturated conditions (Morrow et al., 2017; Tembe et al., 2010).

In subduction zones, montmorillonite transforms into to another type of clay mineral, illite, at temperatures between 120 ºC and 150ºC with increasing depth. This mineral transformation occurs at the plate boundary is generally in accordance with a transition from the shallow conditionally stable zone to a deeper unstable slip zone which generates earthquakes (Saffer and Marone, 2003). Studies indicate that both types of clay exhibit velocity strengthening behavior at room temperature, with illite generally showing a higher friction (Saffer and Marone, 2003; Ikari et al., 2009). Recent studies have shown that illite can exhibit velocity weakening behavior at higher temperature, which may control the transition from shallow aseismic zone to the seismogenic zone at depth (Okuda et al., 2023).

1.3.3 Slow earthquake in clay-rich zone

Slow earthquakes have been discovered in subduction zones due to advance in observation techniques (Ide et al., 2007). The slow earthquakes show significantly lower slip rates comparing to regular earthquakes, with longer duration lasting from several minutes to months. Slow earthquakes typically occur in transition zones adjacent to seismogenic zones.

In the shallow part of the Nankai trough, slow earthquakes have been observed in clay-rich transition zones (Takemura et al., 2022; Yokota and Ishikawa, 2020). This behavior contrasts with the velocity-strengthening characteristics observed in friction experiments at low temperature for both smectite and illite. Ikari (2019) shows that slow earthquake can be reproduced in clay-rich samples when sheared at rate comparable to the tectonic plate movements (cm/yr). Some studies suggest the clay minerals may become velocity weakening after certain process such as lithification or the introduction of material heterogeneity (Ikari and Hupers, 2021; Bedford et al., 2022).

1.4 Clay as yield stress material

1.4.1 Yield stress material

At high water content, the clay-water system becomes a dilute suspension. These suspensions exhibit interesting non-Newtonian behavior, as they cannot flow below a certain threshold stress (Coussot and Proust, 1996; Manga and Bonini, 2012). Similar phenomena

are observed in a broad range of yield stress materials, including gels, emulsions, colloidal glasses, and foams (Bonn et al., 2017).

The elementary model used to describe yield stress is the Bingham model (Bingham, 1922):

$$\tau = \tau_y + \eta_p \dot{\gamma} \tag{1.6}$$

where τ_y is the yield stress and η_p is a model parameter. This model is later generalized into the Herschel-Bulkley model as (Herschel and Bulkley, 1926):

$$\tau = \tau_y + K\dot{\gamma}^n \tag{1.7}$$

where K and n are additional parameters, with n =1 corresponding to the Bingham model. Experimental data from a broad range of yield stress materials, including clay suspensions, gives n<1, typically in the range of 0.2~0.8 (Bonn et al., 2017). This corresponds to shear thinning behavior where the apparent viscosity $\eta_{app} = \frac{\tau}{\dot{\gamma}} = \tau_y/\dot{\gamma} + K\dot{\gamma}^{n-1}$ decreases with increasing strain rate for n<1 (Olsson and Teitel, 2012).

Experimental studies on clay-water system demonstrate that both the yield stress and viscosity increase with solid content (Boukpeti et al., 2012). The result suggests the power law dependence on strain rate applies for system within a wide range of water content from fluid-like suspensions to saturated clayey soils.

However, the physical origin of the yields stress is not fully understood. For particle systems with only repulsive force, yield stress is primarily controlled by volume fraction (Ikeda et al., 2013). For clay suspension and other general colloidal gel with adhesion or attraction force, the underlying physical process can be more complex (Larson, 1999, Zaccarelli, 2007, Chaudhuri et al., 2012). One possible explanation for the emergence of yield stress involves the formation of percolating particle network with strong bonds (Larson, 1999).

1.4.2 Thixotropy

Some yield stress materials exhibit thixotropic behavior, where both the yield stress and viscosity can depend on the shear history of the material. Thixotropy is a time-dependent process where the microstructure of the material builds up during rest and contributes to the macroscopic yield stress (Coussot et al., 2002). During shear, the microstructure can be partly destroyed causing decrease in viscosity or strength (Figure 1.4).

The thixotropy nature of clay suspension have an important application in drilling fluid to provide sufficient low viscosity during drilling operations while maintaining the yield stress and structure to hold the rock fragments in the suspension (Skadsem et al., 2019; Ragouilliaux et al., 2006). Thixotropy can also be observed at high solid content in clayey soil (Ren et al., 2021). The shear strength of the soil decreases after shear but can revert to the initial strength after enough resting time. Zhang et al. (2017) demonstrated that soil structure evolves from

dispersed to flocculated during rest with homogenization in pore size distribution.

Unstable flow phenomena, such as stick-slip motion and shear band, have been observed in clay suspension and other thixotropy yield stress fluid (Pignon et al., 1996; Varnik et al., 2003; Chaudhuri et al., 2012). Kameda and Hamada (2022) incorporated thixotropy in a spring-slider model and successfully reproduced stick-slip motion.

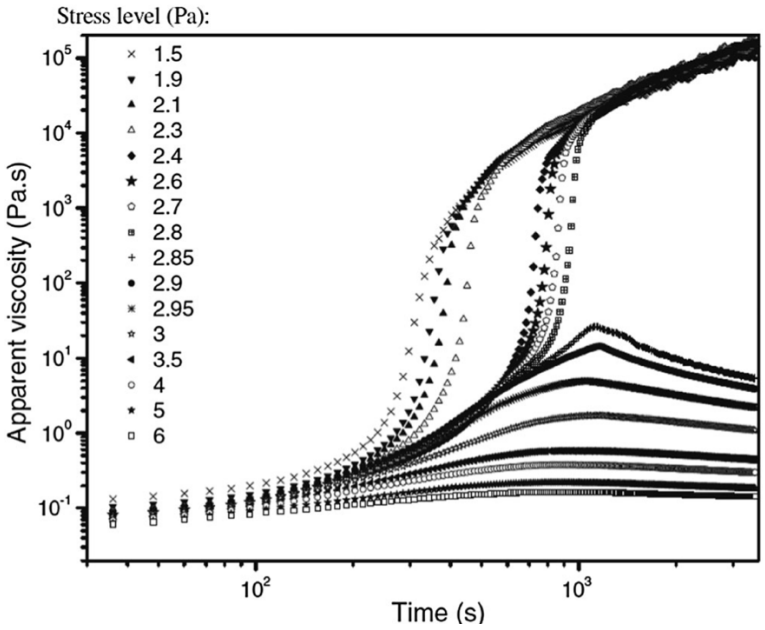

Figure 1.4: Temporal evolution of apparent viscosity of a drilling mud with different applied stress (Ragouilliaux et al., 2006)

1.5 Fabric development and particle orientation

Both field and laboratory studies have revealed some interesting fabric evolution that can affect the frictional strength of clay-rich faults (Haines et al., 2013; Kenigsberg et al., 2019; Kenigsberg et al., 2020; Logan and Rauenzahn, 1987: Niemeijer et al., 2010; Saffer and Marone, 2003). For example, scaly clay foliation was observed in a core sample taken from the shallow source fault of the 2011 Tohoku-Oki earthquake (Chester et., 2013).

The development and evolution of fabrics in clay-rich gouge have been studies in laboratory experiments. The extent of particle alignment can be characterized by the fabric intensity using X-ray texture goniometry techniques (Haines et al., 2009). For montmorillonite, the fabric intensity increases systematically with shear strain before reaching a steady state at large enough strain. The fabric intensity is stronger at higher normal stress. Macroscopic fabrics including Riedel shears and boundary-parallel shears develop systematically with the shear strain in crushed montmorillonite (Kenigsberg et al., 2019). Figure 1.5 shows a smooth

boundary layer with the sub-micron thickness on a Reidel shear surface, where particles align perfectly parallel to the surface (Haines et al., 2013). The result suggests that clay particles reoriented along planes perpendicular to the maximum principal stress. Shear under dry and water-saturated condition yields different surface textures: water-saturated gouge exhibit well-developed shiny shear surface with grained orientated parallel to the shear plane, whereas dry samples appear rough and grainy (Moore and Lockner, 2007).

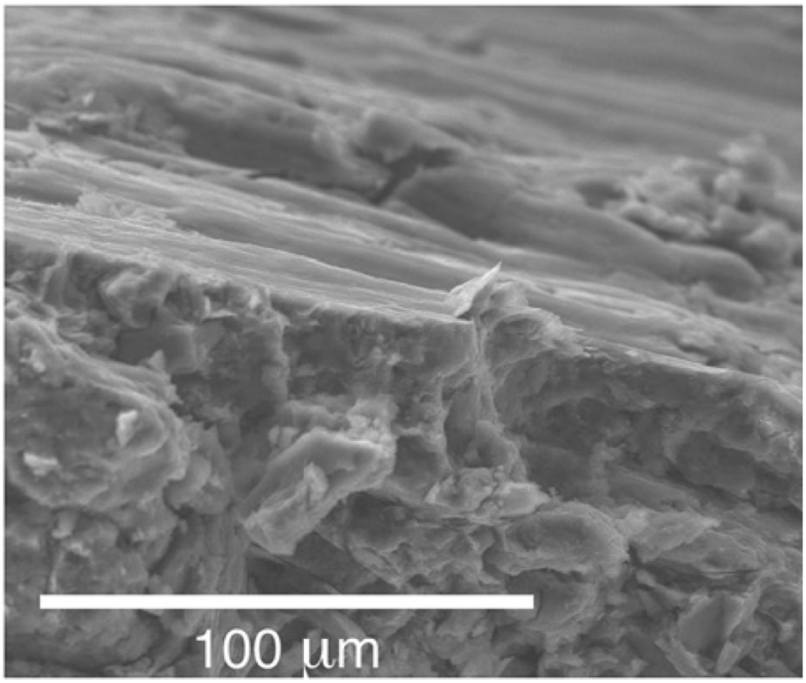

Figure 1.5: SEM image of Reidel shear surface of montmorillonite (Haines et al., 2013)

1.6 Model clay system

Advancements in understanding clay interaction and swelling have been propelled by the development of molecular dynamics (MD). MD simulations can reproduce the force field of clay together with explicit atomistic structures of clay, ions, and solvent molecules. However, such fully atomistic models are often limited to small systems due to high computational cost (Underwood and Bourg, 2020). Current simulations on clay swelling or the interlayer sliding behavior typically focus on interactions between two clay platelets in the bulk water (Ho et al., 2019; Wei et al., 2021).

Attempts have been made to simplify complex interactions between clay platelets and the irregular, high aspect ratio shape. The early studies focused on the structure and phase diagram of dilute clay dispersion using well-characterized synthetic clay like Laponite. Dijkstra et al. (1995) employed an infinitesimally thin disk with a quadrupole potential to

model clay platelets with electric double layers, successfully reproducing the sol-gel transition similar to the experimental observations. Subsequent studies constructed platelet model from multiple charged sites interacting via electrostatic potential (Delhorme et al., 2014; Kutter et al., 2000; Odriozola et al., 2004; Ruzicka et al., 2010; Thruesson et al., 2017). The resulting interaction can be viewed as a generalization of DLVO potential for platelets.

Recently, microscopic level clay model is adopted by the geomechanics community in order to deepen the understanding on fine-grained clayey soil behaviors. The shape of the platy minerals can be simplified as rods in 2D and cuboids in 3D. Figure 1.6 shows a common approach to constructing one clay platelet with sphere aggregates in simulations with interaction based on DLVO theory or laboratory measurements (Aminpour and Sjoblom 2019; de Bono et al., 2022). These studies focused on compression and shearing of a denser system under controlled confining pressure. In particular, the Gay-Berne (GB) potential has been used to study clay aggregation with the shape simplified to oblate ellipsoid (Bandera et al., 2021; Ebrahimi et al., 2014). The GB potential has both short-range repulsion and mid-range attraction. It is commonly used in liquid crystal studies with the ability to account for both the shape and interaction anisotropy of clay platelets.

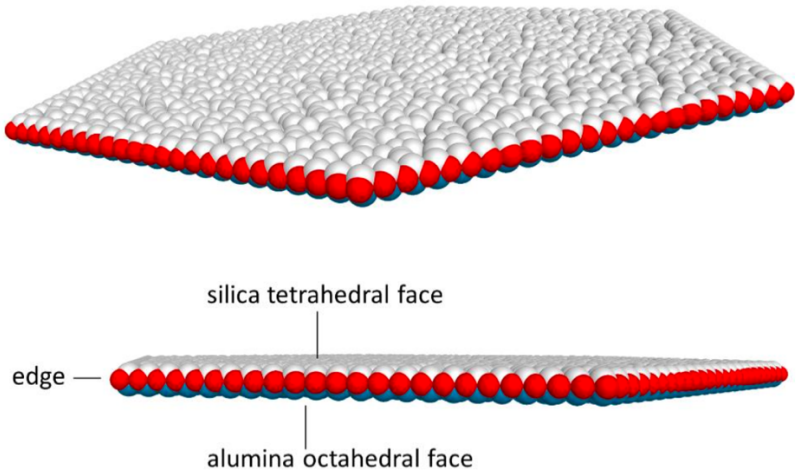

Figure 1.6: clay platelet model built with spheres in discrete element method simulation (de Bono et al., 2022)

1.7 The objective of this thesis

As discussed above, shear in smectite clay exhibit distinct features such as low shear resistance and particle alignment, contrasting with strong minerals such as quartz. Despite the frictionally stable behavior of smectite from shear experiments, signs of unstable shear can be observed from field, laboratory, and thixotropic studies. The origins of these characteristics

remain elusive. Given that smectite clay can carry charges and absorb water, conventional understanding based on friction at contact surface may not adequately explain shear resistance of smectite. Thus, more effort is needed to bridge particle-level mechanisms with macroscopic behaviors.

Coarse-grained simulations using simplified shape and interactions have been proved to be a useful tool in recent clay studies on compressed clay systems. While existing simulations with shear applied through deviatoric stress are limited to small strain deformation, few studies have utilized this approach to study the rheology or friction of clay under large deformation using similar approach. To consider clay in a fault zone condition, the system at low porosity and higher normal stress must be studied.

In this thesis, we employ the coarse-grained molecular dynamics simulation to examine the shear behavior of a simple model clay system. We focus on the shallow subduction zone where smectite clay is abundant. By studying the microscopic shear process in the model system, we aim to elucidate the rheology and the structure development of clay and clay-rich faults. Another aim is to provide insights into the relationship between shear behavior and microstructure. We investigate the effect of strain rate, normal stress, and energy anisotropy to achieve a more comprehensive understanding of the model clay system.

1.8 The structure of this thesis

In Chapter 2, we construct a three-dimension (3D) model to explore the stress and fabric development during shear process. We investigate the formation of shear band at low strain rate and its relationship with particle orientation. Additionally, we analysis the structure recovery after shear. The results of the model system are then compared with experimental observations of shear process and shear resistance. In Chapter 3, we investigate the constant strain rate shear in a two-dimension (2D) system with focus on the effect of normal stress and energy anisotropy. We discuss the interplay between shear stress and change in microstructure and compare the 2D results with 3D from frictional properties, structure, and shear band. In Chapter 4, we investigate the shear instability of the system by performing shear in a confined 2D system. We discuss the effect of normal stress and relationship between the unstable flow and yield stress.

2 Rheology and structure development of model smectite clay during shear in a 3D system

2.1 Introduction

In this chapter, we investigated the rheology and the structure development of a model clay system. Our primary focus is on exploring the feasibility of using a simple particle-level model to study the shear process of the clay system. We begin by introducing the previous application of the Gay-Berne potential in clay studies and the phase behavior of the GB system.

2.1.1 Gay-Berne potential for clay interaction

Ebrahimi et al. (2014) proposed a novel modeling approach to describe the montmorillonite interaction using the Gay-Berne potential, simplifying the shape to oblate ellipsoid. The GB potential is an anisotropic form of the Lenard-Jones potential for non-spherical particles, providing the short-range repulsion and mid-range attraction needed in clay interaction.

The parameters for the GB potential were first calibrated from full atomistic MD simulation of clay platelets in different orientations (face-to-face and edge-to-edge). The position and depth of the potential well were fitted to match the free energy minimum of two clay platelets in bulk water with explicit ions and water molecules. The GB potential serves as a good generalization to capture the detailed information from smaller scale.

Previous simulations using this method have successfully reproduced the aggregation and compression behavior of clay soils (Ebrahimi et al., 2014; Ebrahimi et al., 2016). The compression curves of natural clay were predicted accurately. The aggregation size distribution observed in these simulations matches the result from electron microscopy and X-ray scattering experiments. The elastic properties with GB aggregates are comparable to nano-indentation results, indicating s the elastic stiffness increases with the size of the platelet and external pressure.

2.1.2 Phase behavior of discotic GB system

The GB potential was extensively used in simulation studies of liquid crystal before its application to clay modelling. The repulsion and attraction in GB potential enable it to capture various thermodynamic phase behavior and self-organization of molecules. The oblate ellipsoid shape used for clay models resembles discotic liquid crystal molecules.

Discotic liquid crystals form intermediate phases between the liquid and solid state, with phase diagrams distinct from the more popular rod-like liquid crystals (Caprion et al., 2003; Cienega-Cacerez et al., 2014). The discotic GB system exhibits an isotropic phase at low density, with random particle orientation and position. At intermediate density and high

temperature, the system transit into a nematic phase with increasing orientational order. At high density, the system self-organizes into a columnar phase where discs pile up by stacking on each other. Highly structured phase with long-range orientational and positional order can be obtained.

Clay minerals, sharing shape anisotropy with discotic liquid crystals, also exhibit phase transition at high water content. Studies on dilute suspensions shows clay can transit from isotropic to nematic phase with increasing clay content, displaying permanent birefringent textures (Michot et al., 2004). However, natural clay does not form highly structured columnar phase at high density due to its wide size distribution and irregular shape. Recent clay simulations using GB potentials have considered mixtures with particles of different aspect ratios to avoid artificial crystallization (Bandera et al., 2021., Ebrahimi et al., 2016).

2.1.3 Shortcomings of previous studies

While Gay-Berne potential and other mesoscale model with simplified shapes and interactions have proven useful in recent studies on dense clay systems, these studies mainly focused on reproducing the behavior of clay system under triaxial conditions with controlled confining pressure (Asadi et al., 2022; Bandera et al., 2021; Bayesteh et al., 2021; de Bono et al., 2022; Ebrahimi et al., 2016). Shear was often performed by applying small axial strain increment and measuring the deviatoric stress of the system. These studies are important to understanding the failure of clay soil under small deformation (strain usually smaller than 1).

However, in the natural environments, clay minerals are often found in mature fault gouges or subduction zones, where the fracture surfaces have already formed and are well defined. The clay inside the fault gouge can experience much longer strain comparing to the triaxial system. Typical experiments on clay friction use thin gouge layers sheared between two sliding blocks. Currently, few studies have applied the new mesoscale method to study the rheology or friction of clay under large deformations. The validity of the GB potential in reproducing the frictional behavior of smectite clay remains unclear. In dilute systems, Yamamoto et al. (2005) used the GB potential to study the suspension rheology of disk-like particles under simple shear. This study predicts shear thinning behavior in viscosity and particle alignment in the flow direction at high strain rates. To simulate clay under fault zone conditions, a system with lower porosity and higher normal stress must be studied.

2.1.4 The objective of this chapter

In this chapter, we apply a simple clay model in 3D using non-spherical particles with the Gay-Berne potential to study the shear process in molecular dynamics simulations. We focus on the influence of strain rate and normal stress on shear behavior at room temperature. In

Section 2.2, we present the details of the method and the setup of the simulation. In Section 2.3, we present the result during compression, shear, and rest, with the structure development probed from porosity, particle orientation, velocity profile, and parallel radial distribution function. In Section 2.4, we discuss shear resistance and the shear process of the model system in comparison to experiments and natural faults. In Section 2.5, we summarize the results.

2.2 Method

The molecular dynamics enables us to simulate the time evolution of particles under different physical conditions. The simulations are carried out using the LAMMPS simulation package (Brown et al., 2009; Thompton et al., 2022). The molecules are visualized using the OVITO software (Stokowski, 2009).

The temperature and the pressure can be controlled to the desired values using specific algorithms referred to as "thermostat" (temperature control) and "barostat" (pressure control), respectively. In this study, the temperature is always controlled using the thermostat, while the barostat is optional. System with active barostat have constant pressure and changeable volume (constant pressure condition). If the barostat is not active, the system volume is constant, and the pressure can change (constant volume condition). More details on the simulation method of molecular dynamics are presented in Appendix 2-A.

2.2.1 Gay-Berne potential

Particle interactions in MD are often defined with the potential energy as a function of separating distance and the interacting force are calculated from the negative slope of the potential. In the present study, smectite clay platelets are simplified as rigid oblate ellipsoids interacting via the Gay-Berne potential defined by (Coussaert and Baus, 2002; Gay and Berne, 1981; Luckhurst and Simmonds, 1993):

$$U = 4\epsilon_0 \times \epsilon_1(\kappa) \times \epsilon_2(\kappa') \left\{ \left(\frac{\sigma_{ff}}{h_{12} + \sigma_{ff}} \right)^{12} - \left(\frac{\sigma_{ff}}{h_{12} + \sigma_{ff}} \right)^{6} \right\} \tag{2.1}$$

where ϵ_0 determines the energy scale, ϵ_1 characterizes the shape anisotropy defined by the aspect ratio κ, ϵ_2 characterizes the orientation anisotropy in terms of the energy ratio κ'. The aspect ratio κ is the ratio between thickness σ_{ff} and diameter σ_{ee} of a disc-like ellipsoid. Here σ_{ee} sets the length scale of σ_0. The energy ratio κ' is the ratio of potential well depth for two different configurations: end-to-end (ee) and face-to-face (ff). With $\kappa' < 1$, the potential favors ff over ee configuration and promotes stacking. h_{12} is the approximated distance between two interacting particles. The positive term $\left(\frac{\sigma_{ff}}{h_{12}+\sigma_{ff}} \right)^{12}$

represents the short-range repulsion and the negative term $-\left(\frac{\sigma_{ff}}{h_{12}+\sigma_{ff}}\right)^6$ represents the mid-range attraction between two particles. More details on the Gay-Berne potential are given in Appendix 2-B.

Previous studies show that the GB potential is a good approximation for the interaction between two clay platelets derived from the full atomistic MD for end-to-end and face-to-face configurations (Ebrahimi et al., 2014). For simplicity, here we do not pursue the perfect match with the full atomistic MD results but use the parameter values assumed in some recent MD studies. Based on the interaction between two montmorillonite platelets with diameter of ~6 nm in face-to-face configuration (Shen and Bourg, 2021), the potential well of -0.5 eV is chosen for aspect ratio $\kappa = 1/5$. This value corresponds to the free energy minimum at the salinity of 0.3~0.5M NaCl, where the spacing between two hydrated smectite is approximately 1.55 nm. This is the position of the second water interlayer. The soft contact distance is also defined from $\sigma_{ff} = 1.5$ nm.

The system consists of ellipsoids of three different aspect ratios, 1/5, 1/6, 1/7. They have the same population, and are referred to as particle type A, B, and C. They have the same thickness (1.5 nm), but different diameters (7.5, 9.0, 10.5 nm) determined by the aspect ratio. The energy ratio κ' is set to 1/5 for all the particles. The parameter used in the Gay-Berne potential is summarized in Table 2-1.

Parameters	Value
Length scale $\boldsymbol{\sigma_0}$ (nm)	7.5
Particle thickness $\boldsymbol{\sigma_{ff}}$ (nm)	1.5
Particle diameter $\boldsymbol{\sigma_{ee}}$ (nm)	7.5, 9, 10.5
Aspect ratio $\boldsymbol{\kappa}$	1/5, 1/6, 1/7
Energy scale $\boldsymbol{\epsilon_0}$ (eV)	0.0148
Energy ratio $\boldsymbol{\kappa'}$	1/5

Table 2-1 Gay-Berne potential parameters.

2.2.2 Configuration and setup of simulation

The simulation is performed using 4096 particles inside a triclinic box with periodic boundary conditions. Translational and rotational equations of motion are integrated using the velocity Verlet algorithm with a dimensionless time step $\delta t^* = 0.00025$ if not specified. To optimize the computational time, the interaction potentials are truncated at a cutoff of $1.6\sigma_0$.

Initially, each platelet is placed on a simple cubic lattice with the number density of 0.2. The

initial orientation and the initial velocity are assigned randomly. For the following time evolution, Langevin thermostat is used to control the reduced temperature at T* = 1.75 (equivalent to 300.41K). The total force acting on each particle is then (Schneider and Stoll, 1978):

$$F = F_c + F_f + F_r \tag{2.2}$$

where F_c is the force calculated from the interaction potential, $F_f = \Gamma mv$ is a frictional drag force, and F_r is a random force resulting from collisions with solvent particles. Frictional drag is given as $F_f = \Gamma mv$, where Γ is the damping constant, m is the particle mass, and v is the particle velocity. The amplitude of the random force is $\sqrt{2m\Gamma k_B T}$, where k_B is the Boltzmann constant and T is the target temperature.

In the earliest stage of time evolution (duration of t* = 1000 in the dimensionless unit), the system evolves at constant volume to randomize the platelet configuration. Subsequently, the system is compressed and equilibrated under the constant pressure condition using the Nosé-Hoover style barostat. This method assumes the flexible simulation cell. In other words, each dimension of the simulation cell is adjusted to control each normal stress in the X, Y, and Z directions, respectively (Shinoda et al., 2004). The target values are P*=100, 300, 1000, 3000, 6000, and 10000 in the dimensionless unit, which correspond to 0.56, 1.69, 5.62, 16.85, 33.71, and 56.18 MPa. We assume a fully saturated and fully drained system and therefore the normal stress in the present simulation should be interpreted as the effective normal stress i.e., $P = \sigma_n = \sigma_{eff}$. For each stage of pressure elevation, the pressure first increases linearly in t* = 200 and is kept constant in the subsequent equilibration process of t* = 2000 similar to Ebrahimi et al. (2014).

After this compression and relaxation process, the system is sheared at a constant strain rate. The shear is applied by deformation of the simulation cell instead of driven by the movement of plate. Flow velocity is in the X direction with the velocity gradient in the Z direction. The Lees-Edwards boundary condition is used in the Z direction to adapt to the shear strain (Evans and Morriss, 2007). The particle velocity in the X direction is updated when one goes across the $\pm$Z boundaries as:

$$v_{x\_new} = v_x \pm \dot{\gamma} L_z \tag{2.3}$$

Here L_z is a system dimension in the Z direction and $+ \ / \ -$ are for particles leaving from the bottom/top boundary, respectively. In addition, the particle interaction across the Z boundary is computed with the additional distance of $\pm\dot{\gamma}L_z$ in the X direction. Standard periodic boundary conditions are applied in the X and the Y directions.

The frictional drag force in the Langevin thermostat is applied with the bias of linear velocity profile during shear in the flow direction x as:

$$F_{f\_x} = \Gamma m(v_x - \dot{\gamma} z) \tag{2.4}$$

where v_x is the x component of a particle's velocity, $\dot{\gamma}$ is the strain rate, and z is the z coordination of a particle.

During shear, the Nosé-Hoover barostat is only applied in the Z direction to control the normal stress. The dimensionless strain rates are given as $\dot{\gamma}^*$ = 1, 0.4, 0.1, 0.04, 0.01, and 0.001 (6.93×10^8, 2.77×10^8, 6.93×10^7, 2.77×10^7, 6.93×10^6, and 6.93×10^5 /s) at the dimensionless normal stresses of P* = 300, 1000, 3000, 6000, and 10000 (1.69, 5.62, 16.85, 33.71, and 56.18 MPa). A reduced time step δt^* = 0.000125 is used in the case with P = 56.18 MPa and $\dot{\gamma} = 6.93\times10^5$ /s. We pay more attention to the system at P = 5.62 MPa, which is comparable to the effective normal stress of 7.0 MPa at the shallow subduction zone that accommodated the large slip in the 2011 Tohoku-Oki earthquake (Chester et al., 2013).

To examine the structural change after the flow cessation, the sheared system is hold again and relaxed without shear for the duration of t* = 1000. In this hold period, we consider two different conditions: constant volume and constant pressure. At the constant pressure condition, the normal stress in the Z direction is controlled at the same value throughout the shear and the hold. The result is reported in the real unit for comparison with the previous studies.

2.2.3 Structural analysis:

Structural analysis tools on the bulk system can be used with the application of periodic boundary. The extend of particle alignment in the system can be determined from the orientational tensor:

$$Q = \frac{1}{2N}\sum_{i=1}^{N}(3u_i \otimes u_i - I) \tag{2.5}$$

where u_i is the unit vector along the symmetry axis of particle i (i.e., the normal vector of platelet i), ⊗ denotes the tensor product, I denotes the identity matrix, and N is the total number of ellipsoids in the system. The nematic order parameter S is then defined as the largest eigenvalue of the orientational tensor Q. When the nematic order parameter vanishes (S = 0), the orientation of each platelet is randomly distributed, whereas S = 1 means that all the platelets are perfectly aligned. The corresponding eigenvector is referred to as the director of the system, which is regarded as the averaged symmetry vector of the platelets.

The parallel radial distribution function (PaRDF) is used to characterize the spatial structure of the platelet mixture (Busselez et al., 2014; Caprion et al., 2003; Cienega-Cacerez et al., 2014). The PaRDF is the radial distribution function along the symmetry axis of particle i (i.e., the normal vector of platelet i) $\hat{\boldsymbol{u}}_i$ and expresses the extent of stacking structure (tactoid formation) of platelets. It is defined as:

$$g^{\parallel}(r) = \frac{V}{N^2 2\pi(\sigma_{ee})^2 h}\langle \sum_i \sum_{j\neq i} \delta(r - r_{ij}^{\parallel})\theta(\frac{\sigma_{ee}}{2} - |r_{ij}^{\perp}|)\rangle \quad (2.6)$$

where V is the volume of the simulation box, N is the number of ellipsoid particles, h is the cylinder height used to discretize the volume. $r_{ij}^{\parallel} = |\boldsymbol{r}_{ij}^{\parallel}| = |\boldsymbol{r}_{ij} \cdot \hat{\boldsymbol{u}}_i|$ is the center-to-center distance between particle i and j along the symmetry axis of particle i, and $r_{ij}^{\perp} = |\boldsymbol{r}_{ij}^{\perp}| = |\boldsymbol{r}_{ij} - \boldsymbol{r}_{ij}^{\parallel}|$ is the corresponding perpendicular component. $\theta(x)$ is the Heaviside step function. We use the diameter of the smallest particle type A (aspect ratio 1/5) for σ_{ee} in the mixture system The sum regarding j is taken only for the particles within the perpendicular distance of the particle radius $(\sigma_{ee}/2)$. The PaRDF gives the normalized probability density of finding another particle along the symmetry axis direction of the center particle at the distance of r. The search is restricted inside a column region where σ_{ee} is the diameter of the searching column. A schematic figure of PaRDF is shown in Figure 2.13 in Appendix 2-C.

2.3 Result

2.3.1 Porosity and nematic order under compression

Examples of the system configuration are shown in Figure 2.1 at the normal stress of 5.62 MPa. A similar configuration at a higher normal stress of 33.71 MPa is shown in Figure 2.14 in Appendix 2-D.

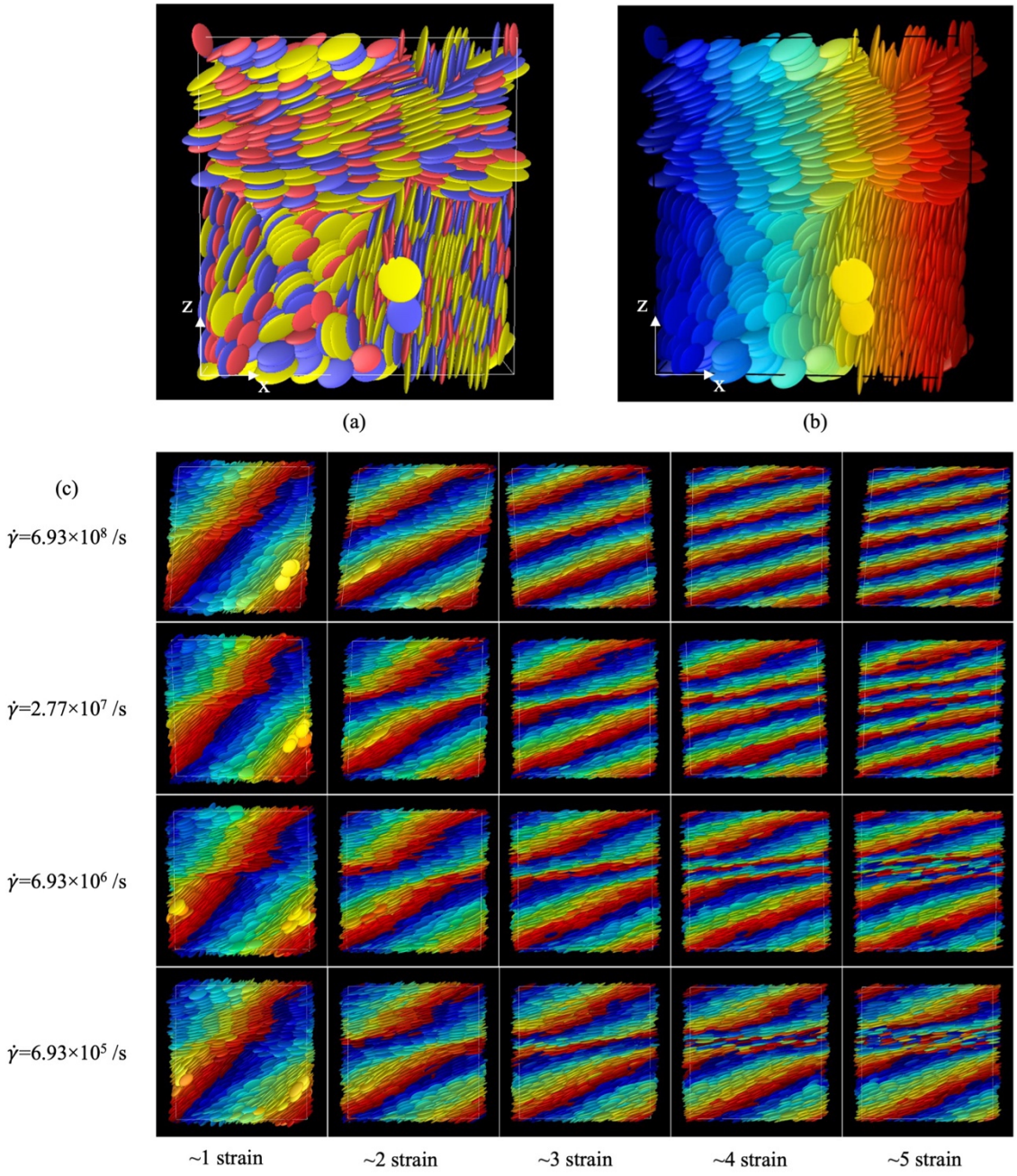

Figure 2.1: Examples of compression and shear configurations at normal stress P = 5.62MPa, a view on the XZ plane. (a) Compressed system colored by different particle aspect ratio, where red, blue, and yellow correspond to particle aspect ratio of 1/5, 1/6, and 1/7. (b) Mixture system colored by the x coordinate of particles at strain of 0, the same coloring is used for (c). (c) Two scenarios are observed with homogeneous shear at high strain rate ($\dot{\gamma} \geq$ 2.77×10^7 /s) and the shear band at low strain rate ($\dot{\gamma} \leq$ 6.93×10^6 /s). Shear localization appear after the strain of 2 and is more obvious at lower strain rate.

The system is first compressed to reach equilibrium at the given normal stress. The target values are 0.56, 1.69, 5.62, 16.85, 33.71, and 56.18 MPa, respectively. The compaction process is monitored via the porosity $n_p = (1 - V_{particle}/V_{system})$, which decreases from 0.48 at P = 0.56 MPa to 0.33 at P = 56.18 MPa (Figure 2.2(a)). The range of porosity in our simulation is similar to some experimental data: e.g., oven-dried Na-smectite (Likos and Lu, 2006) and partially saturated bentonite at higher normal stress (Baille et al., 2010), while Na-Ca-smectite (MX80) saturated with pure water at low normal stress showed higher porosity (Marcial et al., 2002).

Figure 2.2(b) shows that the nematic order increases from 0.37 to 0.47 during compression, indicating increasing order in orientation at higher normal stress. A similar trend is observed in both experimental and simulation studies (Ebrahimi et al., 2016; Perdigon-Aller et al., 2005). Recent mesoscale simulations on clay matrix also suggest less orientational anisotropy for the larger system size (Asadi et al., 2022; Bandera et al., 2021).

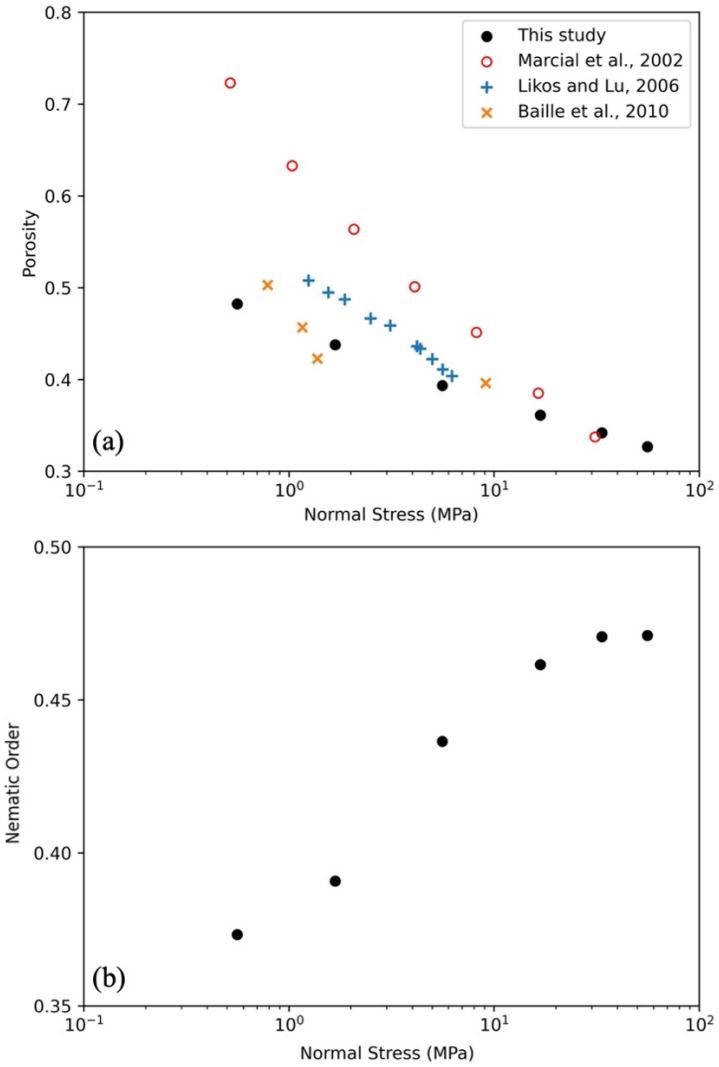

Figure 2.2: Porosity and nematic order as a function of normal stress during compression. Solid circle: present study, compressed to the normal stress of 0.56, 1.69, 5.62, 16.85, 33.71, and 56.18 MPa. Hollow circle: saturated Na-Ca-smectite (Marcial et al., 2002). Plus: oven-dried Na-smectite (Likos and Lu, 2006). Cross: partially saturated bentonite (Baille et al., 2010).

2.3.2 Shear

2.3.2.1 Shear stress and structure development

The stress-strain curves are shown in Figure 2.3(a). Each curve shows a peak and the subsequent weakening with increasing shear strain until a residual strength is reached. The stress peaks around the 200% shear strain for strain rates below 2.77×10^{8} /s. At higher strain rates, both the peak stress and the steady-state value increase. This trend is common to

experiments on crushed montmorillonite that show overshoot in the stress-strain relationship (Haines et al., 2013; Kenigsberg et al., 2019).

The evolution of porosity is shown in Figure 2.3(b). At lower strain rates, the porosity decreases with strain before reaching the steady-state value. At higher strain rates, the system first dilates and then compresses, with the peak of dilation occurring during the first 200 % strain. The porosity is larger at higher strain rates, but it may take even larger shear strains (larger than 10) to reach the steady state. We find that the peaks in shear stress and porosity at early strains coincide at higher strain rates.

The nematic order parameter S increases from 0.4 to near 1.0 for all the strain rates, suggesting that the system becomes more orientationally ordered by the shear (Figure 2.3(c)). A closer look at a region above S = 0.9 (Figure 2.3(d)) shows that the nematic order increases rapidly to above 0.9 within the 200% shear strain and then continues to increase slowly until reaching the steady-state value. Systems at higher strain rates reach the similar nematic order above S = 0.98, while relatively low nematic order is realized at the two lower strain rates (6.93×10^{6} and 6.93×10^{5} /s).

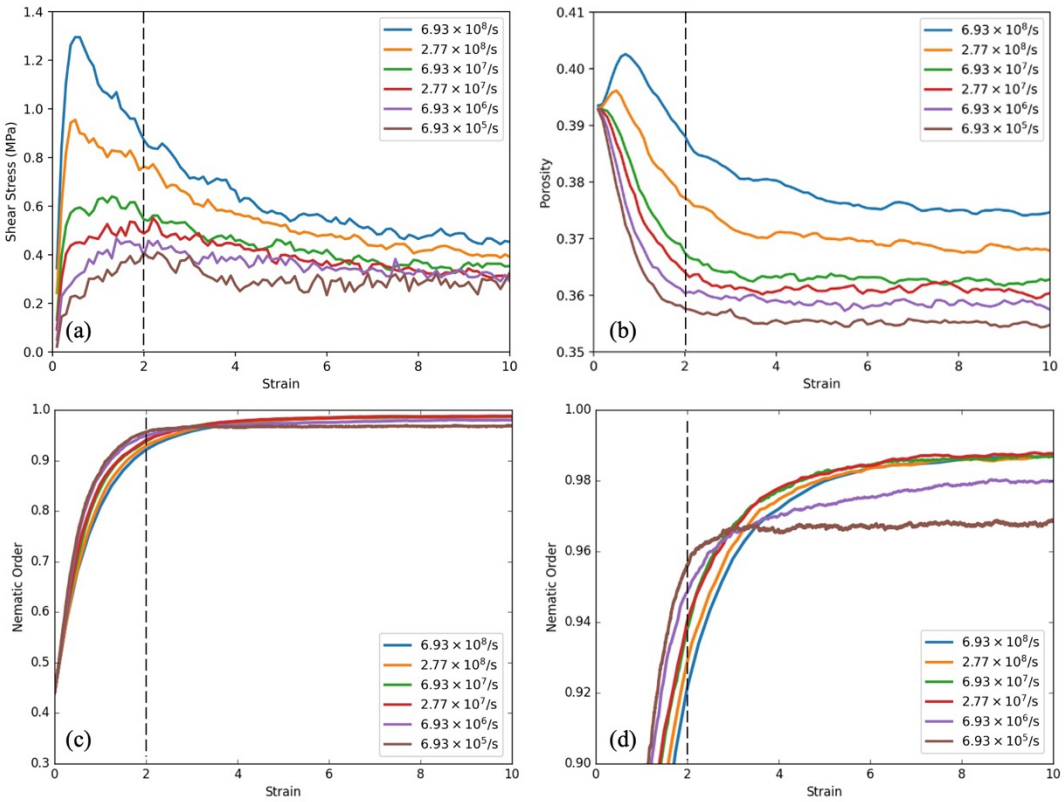

Figure 2.3: Example of (a) shear stress, (b) porosity, and (c, d) nematic order parameter as a function of shear strain for all strain rates at the normal stress of 5.62 MPa. Dashed line is a

guide to the eye for the position of peak shear stress around the strain of 200% for lower strain rate cases. The two highest strain rates experienced the peak stress at early strain, close to the position of dilation in porosity. (d) A zoom at larger nematic order shows the two lowest strain rates reached slightly lower order.

2.3.2.2 Steady-state rheology

The shear stress averaged over the strain of 8 to 10 in each run is used as the steady-state shear stress for further comparison. The result for different strain rates and different normal stresses is summarized in Figure 2.4(a). The steady-state shear stress can be characterized by the following equation:

$$\tau = \tau_y + K\dot{\gamma}^n \tag{2.7}$$

where the yield stress τ_y denotes the shear stress at the zero-strain rate limit, K is a constant and n is the exponent. Equation (2.7) is referred to as the Herschel-Bulkley (HB) model, which is an empirical law describing non-Newtonian rheology such as the flow of mud and clay suspensions (Coussot and Proust, 1996; Manga and Bonini 2012). The HB model is reduced to the Newtonian fluid with τ_y=0 and n=1, and K is then the dynamic viscosity of the fluid.

The yield stress τ_y increases with the normal stress (Figure 2.4(b)). An approximation with the linear dependence on normal stress gives the coefficient of friction, which turns out to be very small: 0.0135. The residual shear stress at the vanishing normal stress is about 0.25 MPa. The exponent n is below unity in all the cases, indicating the shear thinning behavior. We find the tendency that the exponent n decreases with normal stress (Figure 2.4(c)). Note that the correction of strain rate with shear band does not significantly affect the stress-strain rate relationship as shown in Figure 2.15 in Appendix 2-E.

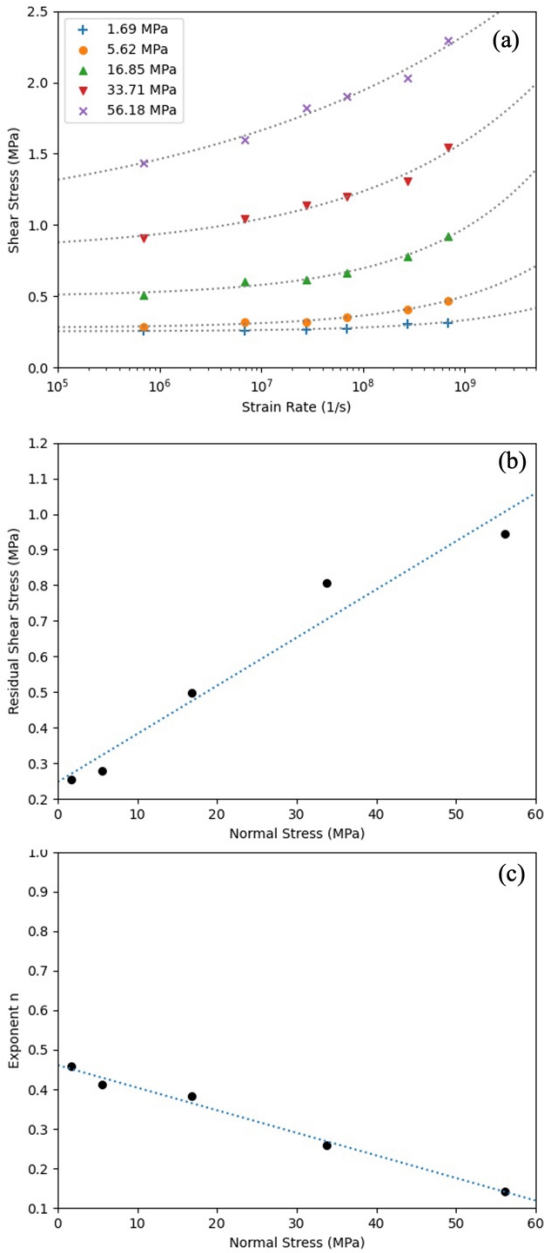

Figure 2.4: (a) Shear stress as a function of strain rate at different normal stresses, fitted with Herschel-Bulkley model. (b) The residual shear stress at zero strain rate limit increases with normal stress. The dotted line is the approximation with a linear model. (c) The exponent decrease with normal stress. The dotted line is the approximation with a linear model.

The steady-state coefficient of friction is defined by:

$$\mu = \tau/\sigma_n \tag{2.8}$$

The coefficient of friction is apparently small in the range of 0.025 to 0.187 and decreases with increasing normal stress and increases with strain rate (Figure 2.5(a)). The porosity decreases with normal stress and increases with strain rate (Figure 2.5(b)). This is consistent with experiments where dilation is observed in response to the increasing shear velocity (Ikari et al., 2009).

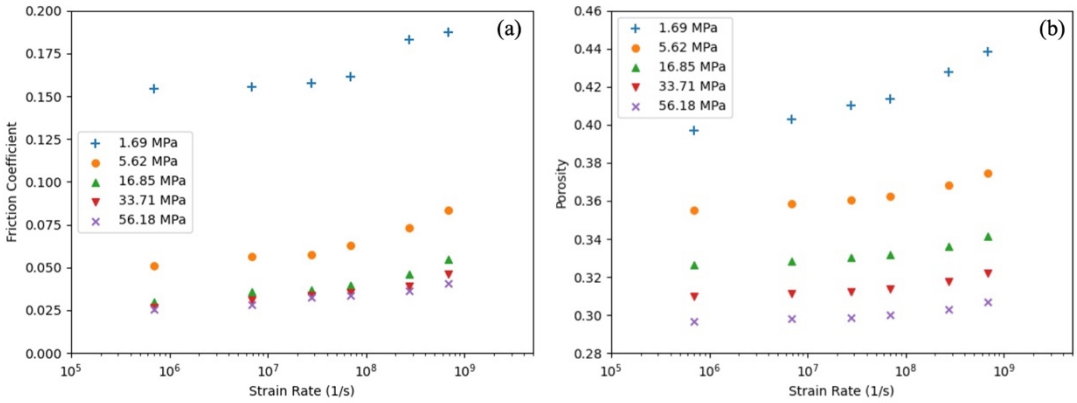

Figure 2.5: Friction coefficient and porosity as a function of strain rate at different normal stresses.

2.3.2.3 Shear banding

Visual inspection shows that shear banding is more apparent at lower strain rates, while homogeneous shear is more common at higher strain rates (Figure 2.1). The velocity profile at P = 5.62 MPa is shown in Figure 2.6 with samples divided into 20 layers along the Z direction. In each velocity profile, the flow velocity is averaged over each strain increment of 0.5. At higher strain rates ($\dot{\gamma} \geq 2.77\times10^{7}$ /s), the velocity profile is relatively linear. At lower strain rates ($\dot{\gamma} \leq 6.93\times10^{6}$ /s), shear localization is observed.

The average angle between the symmetry axis of the particle and the Z axis is used to represent the structural rearrangement during shear deformation (Figure 2.6). The samples are divided into 20 layers along the Z direction. The black line at strain 0 shows the initial orientation profile. At high strain rate ($\dot{\gamma} \geq 2.77\times10^{7}$ /s), the velocity profile is linear, and the orientation profile becomes homogeneous at large strains. The dashed line indicates the steady-state value is about 10°. In the presence of shear band ($\dot{\gamma} \leq 6.93\times10^{6}$ /s), the particle orientation is approximately 10° inside the shear band, while it is larger outside the band. A preferred orientation of 10° in the XZ plane and 0° in the YZ plane are observed at high strain rate (see Figure 2.16 in Appendix 2-F). Recent studies show that the preferred orientation is controlled by particle shape at low porosity (Börzsönyi et al., 2012; Marschall et al., 2020, Nagy et al., 2017). Shear banding also explains the low nematic order at low strain rates shown

in Figure 2.3(d), the overall orientation order is lower than in the homogeneous cases.

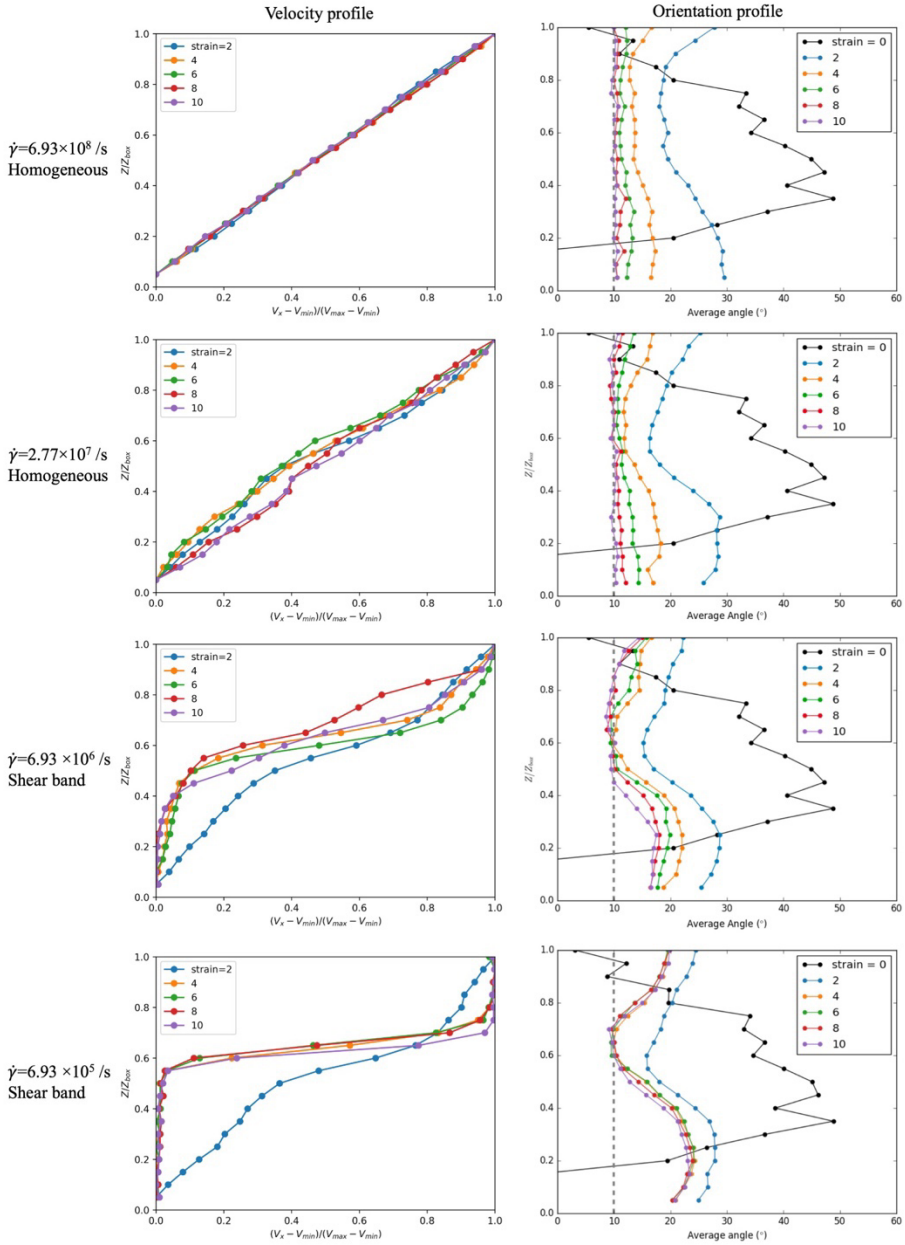

Figure 2.6: Inspection on shear banding from velocity profile (left column) and particle orientation profile (right column) at the normal stress of 5.62 MPa. The velocity profile is close to linear at high strain rates ($\dot{\gamma} \geq$ 2.77×10^7 /s), whereas shear band is formed at lower strain rates ($\dot{\gamma} \leq$ 6.93×10^6 /s). The orientation profile shows average angle between the symmetry axis of platelet and the Z axis along the height. The black line represents the initial structure. The particle orientation approaches 10 degrees uniformly at high strain rate while only particles inside certain region approaches 10 degrees at low strain rate. The region of shear band coincides with the region of preferred particle orientation.

2.3.2.4 Shear band formation

The formation of shear band can be further quantified using the velocity profile and the particle orientation. Here we quantify the deviation from the linear velocity profile using the quantity below:

$$R^2 = 1 - \frac{\sum_i (v_i - f_i)^2}{\sum_i (v_i - \bar{v})^2} \tag{2.9}$$

where i denotes the discretized Z coordinate with 20 layers, v_i is the average X velocity in layer i, $\bar{v}$ is the X velocity averaged over the entire system, and f_i is the X velocity calculated from the linear velocity profile. When $R^2 \simeq 1$, the velocity profile is close to linear: i.e., homogeneous shear is realized.

Since the velocity outside the shear band is not strictly zero, determining the clear shear band from the velocity profile alone can be difficult. Therefore, we also use the information on the particle orientation. When the particles are sheared, their orientation angles tend to be near 10°. As shown in Figure 2.6, the region with preferred orientation angle (8°~12°) overlaps with the larger strain-rate zone shown in the velocity profile. In the following analysis, the thickness of preferred orientation zone (8°~12°) is used to define the width of localized shear zone L_{band}.

The evolution of R^2 and the shear band width is shown in Figure 2.7, where the band width is divided by the system height and shown as a percentage. At the lowest strain rate, shear banding starts around the strain of 2~3 as seen in the decrease of R^2. The normal stress does not significantly affect the onset of shear banding. In addition, the final band width of 30% is independent of the normal stress. Comparing to the nematic order change shown in Figure 2.3(d), the particle orientation does not change significantly after the formation of shear band. At intermediate strain rate, the final band width increases and is wider at lower normal stress.

Interestingly, at high normal stress and high strain rate conditions ($\dot{\gamma} \geq 2.77\times10^7$ /s), R2 first decreases and then increases. This nonmonotonic behavior suggests that the system tends to form the shear band initially, but then returns to homogeneous shear. Simultaneously, more particles are aligned in the preferred orientation and the orientation band expands. The nematic order shown in Figure 3(d) also suggests that particle rearrangement continues in the later stage of shear. Restoration to homogeneous shear is not observed at lower strain rates where the shear band appears to be stable.

At higher strain rate and lower normal stress, the linear velocity profile ($R^2 \simeq 1$) is maintained throughout the shear. The homogeneous shear is defined if the system satisfies the two criteria: 1) R^2 is above 0.9 throughout the shear, and 2) the zone of preferred orientation angle extends to the entire system (100%) at the end of simulation (strain of 10).

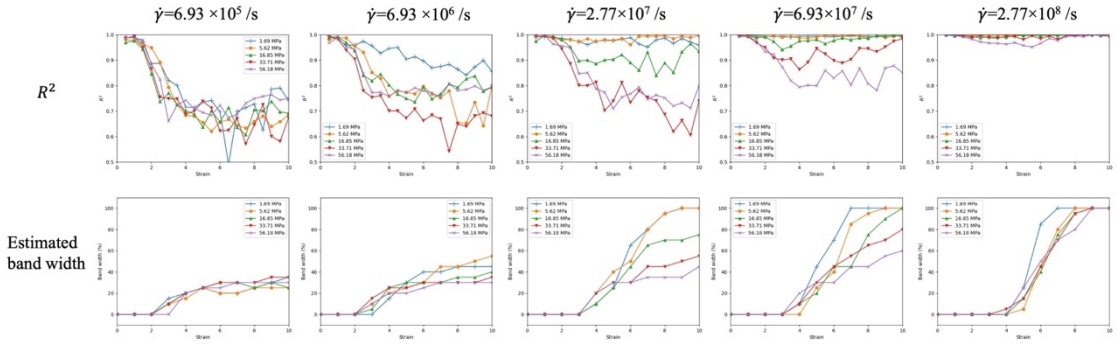

Figure 2.7: The change in deviation from linear velocity profile characterized by R^2 (top row) and the estimated shear band width determined from preferred orientation band (bottom row) at different strain rate for each normal stress. The preferred orientation is normalized by the sample height and shown in percentage. A low R^2 and finite band width at lower strain rates shows the shear is localized. At higher strain rates, R^2 is closer to 1 and band wdith can reach the full sample height suggesting a more homogeneous shear.

The phase diagram of shear banding is shown in Figure 2.8. At lower strain rates and/or higher normal stress, shear is accommodated in the shear band. Conversely, lower effective normal stress and higher strain rate can facilitate the particle rearrangement to increase the shear band width. This tendency is common to general yield stress materials (Berthier, 2003).

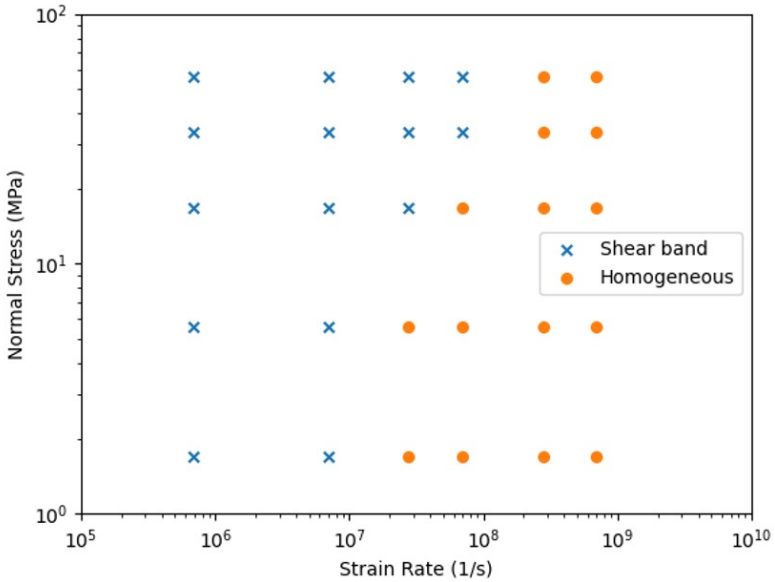

Figure 2.8: The phase diagram of shear band in the range of normal stress and strain rate investigated. Shear band is more likely to occur at lower strain rate and higher normal stress.

2.3.2.5 Stacking structure

Figure 2.9(a) shows the change in PaRDF with increasing strain. The initial configuration at zero strain has a short-range correlation with seven pronounced peaks. The peak height decreases with the parallel distance and diminishes to unity around r = 1.5. Both the peak height and the peak number decreases during shear: i.e., the decrease in the parallel order. At the shear strain of 10, the peaks have a much lower magnitude and only the first three peaks are recognizable. Namely, the parallel stacking of clay particle is reduced by the shear.

In each RDF, peaks larger than 1.05 can be fitted with the exponential function:

$$g_{peak} - 1 = A * \mathrm{e}^{-r/B} \tag{2.10}$$

where B defines the characteristic length for parallel stacking. The fitting result for P = 5.62MPa and $\dot{\gamma}$ = 6.93×10^8 /s is shown as an example in Figure 2.9(b) in a semi-log plot. The peaks at zero strain do not strictly follow the exponential line with higher values at greater distances. After the shear is applied, the peaks first decrease rapidly and reach the lowest curve around the shear strain of 2. Then, in the following 8 strains the peaks increase again gradually but only slightly. In other words, the parallel stacking order does not decrease monotonically with the shear strain. However, since the number of appreciable peaks decreases with the shear, the fitting here may not give a sufficient estimate.

The same analysis is conducted for cases with the strain rate larger than 2.77×10^7 /s at P = 5.62MPa. In Figure 2.9(c), the characteristic stacking size B is shown as a function of shear strain at different strain rates. The result is approximated by an exponential function of the strain:

$$B = C * e^{-\gamma/D} + E \tag{2.11}$$

where γ is the shear strain, D denotes the characteristic strain, and E denotes the residual value at $\gamma = +\infty$. The fitting function (Equation 2.10) generally provides a good estimation but underestimates the stacking size at the strain of 10 for all strain rates. The steady-state stacking size E decreases with strain rate, this again shows the stacking order is reduced by the shear (Figure 2.9(c) inset).

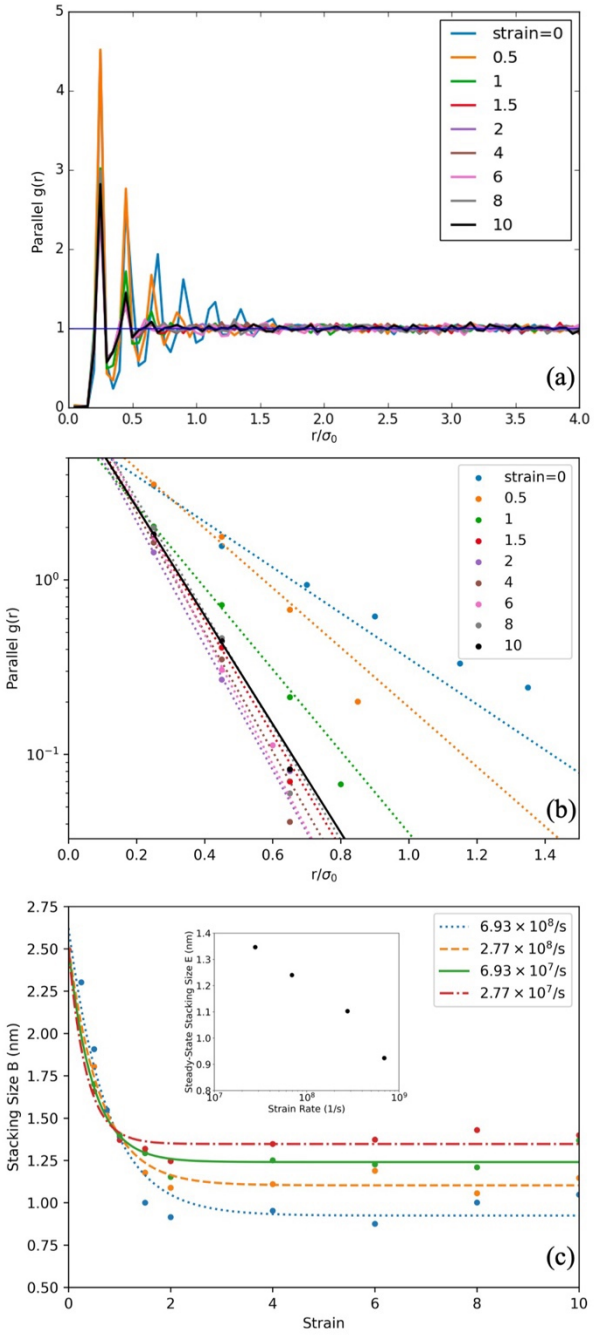

Figure 2.9: Change in the parallel stacking strcture during shear. (a) The parallel stacking structure is first probed with PaRDF for the system at P = 5.62 MPa and $\dot{\gamma} = 6.93\times10^{8}$ /s. Each curve represents a PaRDF at a certain strain. The peak height and the peak number decrease with shear strain. (b) The peak value as a function of distance is fitted with an exponential function from equation (9). (c) A characteristic stacking size B is determined from the change in PaRDF and decreases to a residual value during shear following equation (10). The inset shows the steady-state stacking size E decreases with strain rate.

2.3.3 Aging at rest

Clay can form complex microscopic structure and exhibits thixotropy. Thixotropy is a time-dependent increase of viscosity depending on the shear stress. From a microscopic view, thixotropy is caused by a time-dependent restructuring of fabric of the particles in a suspension referred to as aging. Since thixotropy acts as a positive feedback, stick-slip behavior is expected in clay-rich materials (Kameda and Hamada, 2022).

Here, we study such time-dependent restructuring in our model clay. Structural analysis using PaRDF is conducted on a system at rest after shear at the normal stress P = 5.62 MPa. Shear rate is set to zero after the shear strain of 10 is applied. For the system at rest, we test two different conditions: constant normal stress and constant volume. These two conditions may correspond to drained or undrained conditions at the laboratory scale, respectively.

The characteristic stacking size B increases during rest, indicating the restoration of the parallel stacking structure during rest (Figure 2.10). Previous experiments on samples taken from a phyllosilicate-rich fault have observed frictional healing with the hold time, but the healing rate is much smaller than that in phyllosilicate-free materials (Tesei et al., 2012). For clay suspensions and analog yield-stress materials, the logarithmic increase of peak stress with the waiting time is predicted (Bonn et al., 2017). Here we follow these ideas to use the logarithmic function to describe the restoration of stacking size B as a function of the resting time:

$$B = a + b * \log_{10}(t_{rest}) \tag{2.12}$$

Here the coefficient b is interpreted as the restoration tendency of stacking size. This logarithmic model serves as a reasonable representation of the data for the constant volume condition in Figure 2.10(a), whereas the logarithmic behavior is less apparent for the constant pressure condition in Figure 2.10(b).

Figure 2.10(c) shows the slope b as the function of the porosity at the end of the rest. Although the rest period starts from the same porosity for the two different conditions, the system is further compressed to decrease the porosity at the constant pressure condition. Contrastingly, the porosity is kept fixed during the rest period under the constant volume condition. The restoration coefficient b is larger at higher porosities. Namely, the restoration of stacking structure is faster with more space to reorganize. However, at constant pressure condition, the pore volume decreases after the cessation of shear. Due to little space for reorganization, the restoration is hindered. The result suggests the extent of restoration is more controlled by the porosity of system at rest.

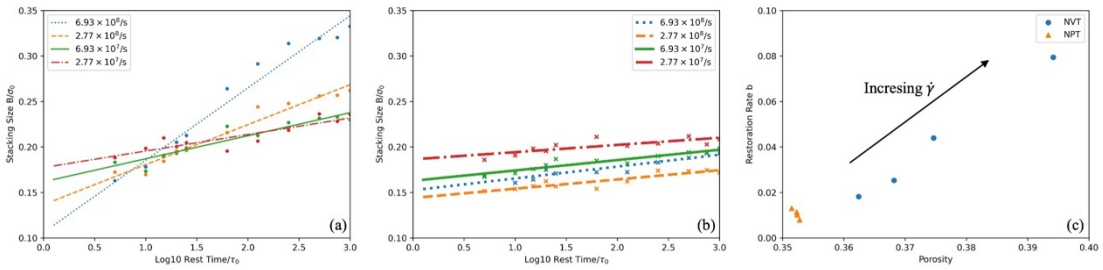

Figure 2.10: The characteristic stacking size increases with the rest time under (a) the constant volume condition and (b) the constant normal stress condition. The lines represent the logarithmic equation (11). (c) The slope b, the restoration rate of the stacking size, increases with the system porosity.

2.4 Discussion

2.4.1 Comparison with previous friction data

The strain rate dependence of shear stress in this study follows the HB model with a finite yield stress at the zero-strain rate limit. This yield stress increases linearly with normal stress, with μ of 0.0135. In comparison, similar linear fitting for yield stress has been used for natural cation-exchanged montmorillonite, which suggests a larger μ of 0.11 to 0.26 (Behnsen and Faulkner, 2013). Morrow et al. (2017) found that μ increased from 0.1 to 0.28 between 10 and 600 MPa for wet montmorillonite.

Our model clay system exhibits a velocity strengthening behavior, which is consistent with previous experimental studies on wet smectite (Behnsen and Faulkner, 2013; Brown et al., 2003; Ikari et al., 2007; Moore and Lockner, 2007; Morrow et al., 1992). In these experiments, the velocity dependence of steady-state friction is estimated in the framework of the rate and state dependent friction law:

$$(a-b) = \frac{\Delta\mu_{ss}}{\ln\left(\frac{V_2}{V_1}\right)} \tag{2.13}$$

where $\Delta\mu_{ss}$ is the change in steady-state friction, and V_1 and V_2 are different steady-state shear velocity. In the present simulation, the steady-state shear velocity is given as $\dot{\gamma}L_{z\_ss}$, where L_{z_ss} is the average box height in the strain of 8-10. As shown in Figure 2.11, the estimated (a-b) values are all positive in the investigated range. They generally increase with strain rate and decreases with normal stress. At the lowest strain rate of 6.93×10^{5} /s, the (a-b) values are in the range of 0 to 0.003. This is larger than the experimental values for wet montmorillonite in the range of 0 to 0.001 at the effective normal stress below 100 MPa

(Morrow et al., 2017). Similarly, Tembe et al. (2010) reported the value of 0.0005 at the effective normal stress of 40 MPa. The discrepancy may be attributed to the strain rate much larger than the experimental values. Recalling the HB model of Eq. (2.7), the (a-b) value is then $\frac{d\mu_{ss}}{dln(V)} = \frac{1}{\sigma_{eff}} \frac{d\tau_{ss}}{dln(\dot{\gamma})} = \frac{Kn}{\sigma_{eff}} \dot{\gamma}^n$, suggesting the (a-b) value is overestimated at higher strain rate. This tendency is consistent with the increase in (a-b) with sliding velocities for partially hydrated montmorillonite (Ikari et al., 2007). The (a-b) value extrapolated from the HB model fit at 56.18 MPa using sliding velocities of 0.1 to 1.0 μm/s is 2.27×10^{-4}, which is comparable to the above experimental data.

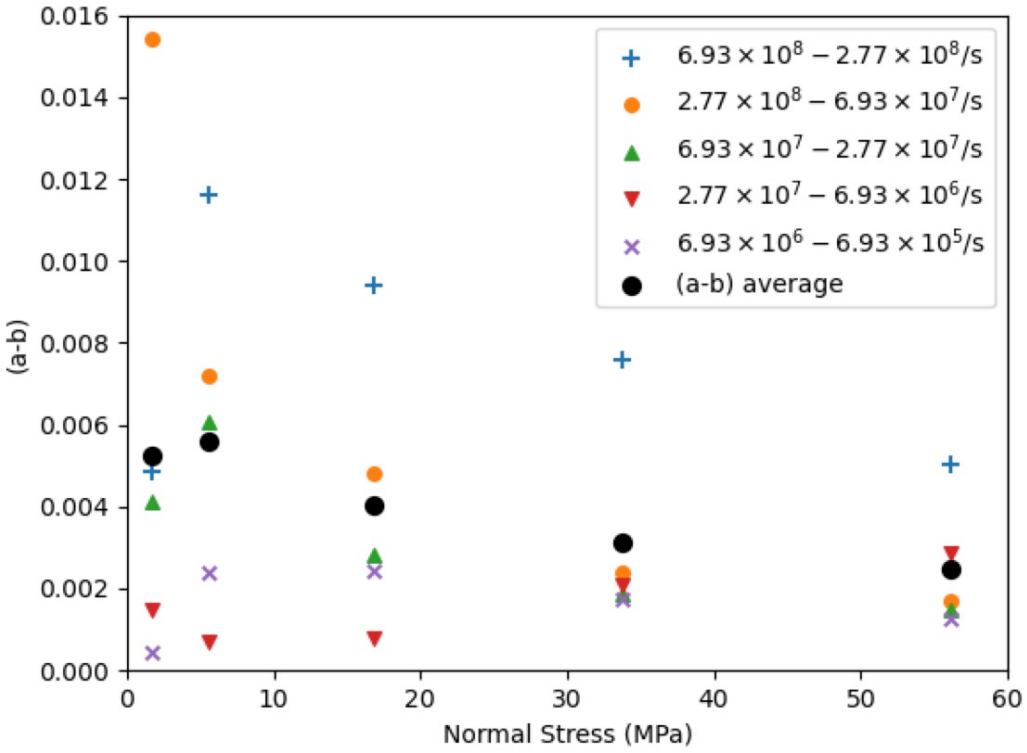

Figure 2.11: The velocity dependence of friction, (a-b), as a function of normal stress for different strain rate. The average (a-b) values are given in black circles.

2.4.2 Structure development during shear

In this section, the change in shear stress is compared to the structural change. At lower strain rates, the porosity decreases rapidly in the initial stage of shear (strain 0 to 2) as shown in Figure 2.3(b). The nematic order and the PaRDF also change drastically in this stage

(Figures 2.3(c) and 2.7(c)). The visual inspection (Figure 2.1), the velocity profile, and the orientation angle profile (Figure 2.7) show the homogeneous shear for the first 200% strain (i.e., $\gamma \leq 2$) and the shear band for the later period, $\gamma > 2$.

The system behavior during shear at low strain rates can be classified into two stages. In stage I, the shear stress increases along with the pronounced structural rearrangement in compaction, particle reorientation, and alignment. The parallel stacking structure declines and the shear is relatively homogeneous. These processes occur in the initial stage of shear ($\gamma \leq 2$). Subsequently, in stage II, the system gradually approaches the steady state. The shear stress decreases to the steady-state value with the formation of shear band. The changes in particle orientation and porosity are relatively small in stage II.

Kenisberg et al. (2019) hypothesized a micromechanical process of clay-rich gouge under shear, following pioneering work of Logan and Rauenzahn (1987) and Haines et al. (2013). Particle reorientation and compaction occur when the shear strain is relatively small. Fabrics such as Riedel shear, boundary shear, and Y shear start to form after the stress peak and reduce the shear stress. Further weakening with progressive shear is controlled by the development of such fabrics and compaction. The structural evolution in the present simulation at low strain rates is somewhat consistent with these experimental observations, although the present system may be too small to accommodate various kinds of spatial structures.

At the lowest strain rate, the above scenario may hold irrespective of the normal stress. As shown in Figure 2.17 in Appendix 2-G, the overall shape of the stress-strain curve is independent of the normal stress. In addition, decrease in shear stress and shear localization occur simultaneously, independent of the normal stress (Figure 2.7). Therefore, the timing of shear localization may not be controlled by the normal stress.

However, the above scenario for structure development does not apply to higher strain rates. As shown in Figure 2.3a and Figure 2.17(b) in Appendix 2-G, the shear stress peaks occur at smaller strain at lower normal stress. However, compaction continues to larger strain values depending on the normal stress. Therefore, stage I cannot be simply defined according to the stress peak. The shear is also more homogeneous at high strain rate without apparent shear banding. We suggest the uniform shear can extend the period of compaction and overall structure rearrangement.

2.5 Conclusion

The rheology and structure of a model smectite clay are studied using molecular dynamics, simplifying the particle shape to an oblate ellipsoid, and employing the Gay-Berne potential for interaction. Despite these simplifications, the model successfully captures several key features of a clay system. The system exhibits velocity-strengthening behavior, which can be

described by the Herschel-Bulkley law. The estimated (a-b) values align with experimental results and increase with strain rates.

Shear localization is observed at lower strain rates and higher normal stresses, where shear is concentrated in a small region with particles aligning in a preferred orientation. At high strain rates, shear becomes more uniformly distributed.

The structure development at low strain rates aligns with the micromechanical processes in previous experimental studies. Initially, particles rearrange to align with shear ($\gamma \leq 2$), causing shear stress to increase to a maximum. Subsequently, a shear band forms, and the shear stress decreases to a steady-state value.

We introduce the parallel radial distribution function (PaRDF) to analyze changes in the parallel stacking structure. The characteristic stacking size decreases with shear strain and undergoes logarithmic healing during rest period. The amplitude of restoration rate increases with the porosity of the resting system. Although this offer insights into the healing process in natural faults, one must note that the timescale is very different. More extensive studies are needed to connect simulation healing behavior to healing processes in natural clay-rich faults.

While the model is simple, it proves useful for studying the rheology and microstructure of clay systems. Future improvements could include adopting a broader size distribution in a larger system to explore large-scale structures. Additionally, varying shear configurations beyond steady-state shear could provide more information on the stability and rheology of the model clay system. Understanding the effects of particle shape and interaction may help us generalize these results to other phyllosilicate minerals.

Appendix 2-A Molecular dynamics

Appendix 2-A-1 System dynamics

The molecular dynamics enables us to simulate the time evolution of particles under different physical conditions. First, the initial conditions are created by setting the dimension of the simulation cell and the properties of particles to be used in the simulation. The pairwise interactions are defined by setting potentials as a function of relative distance and orientation between particles with a cutoff distance. In the current study, the particle is non-spherical, the particle mass is assigned, and the shape and size are determined by the length of particle axis. The particles are then created with initial position and velocity.

The simulation is performed by solving the Newton-Euler equation for translational and rotational motion. We consider a system with N particles with the position of particle i determined by coordinates of the particle center r_i and orientation ξ_i.

For each step, the total potential energy of a particle is computed as:

$$U_i = \sum_{j=1, j\neq i}^{N} U_{ij} \tag{2.14}$$

The force and torque acting on a particle is then:

$$\boldsymbol{F}_i = \sum_{j=1, j\neq i}^{N} \frac{-\partial U_{ij}}{\partial \boldsymbol{r}_{ij}}, \boldsymbol{T}_i = \sum_{j=1, j\neq i}^{N} \boldsymbol{r}_{ij} \times \boldsymbol{F}_{ij} \tag{2.15}$$

where r_{ij} is the center-to-center distance between particle i and j. For non-sphere particles, the equation of translational and rotational motion is updated as:

$$\boldsymbol{F}_i = m_i \frac{d\boldsymbol{v}_i}{dt}, \boldsymbol{T}_i = \boldsymbol{I}_i \frac{d\boldsymbol{\omega}_i}{dt} \tag{2.16}$$

where $\boldsymbol{I}_i$ is the inertia tensor and $\boldsymbol{v}$ and $\boldsymbol{\omega}$ are linear and angular velocity, respectively. In numerical simulations, the quaternion provides a simpler representation for particle orientation and rotation in the three-dimensional system comparing to Euler angles. A unit quaternion $\boldsymbol{q} = q_w + q_i\boldsymbol{i} + q_j\boldsymbol{j} + q_k\boldsymbol{k}$ have a norm $\|\boldsymbol{q}\| = \sqrt{q_w^2 + q_i^2 + q_j^2 + q_k^2} = 1$. The unit vector $\boldsymbol{i}$, $\boldsymbol{j}$, and $\boldsymbol{k}$ is along the X, Y, and Z axis of the system, respectively. For rotation of degree θ around a unit rotation vector (a, b, c) in three-dimensional space, the quaternion gives:

$$\begin{aligned} q_w &= \cos\left(\frac{\theta}{2}\right) \\ q_i &= \mathrm{a} * \sin\left(\frac{\theta}{2}\right) \\ q_j &= \mathrm{b} * \sin\left(\frac{\theta}{2}\right) \\ q_k &= \mathrm{c} * \sin\left(\frac{\theta}{2}\right) \end{aligned} \tag{2.17}$$

In 2D space, the rotation vector is restricted to (0,0,1).

The orientation of particle can be written as an ordinary quaternion $\boldsymbol{p} = (0, x, y, z)$. The quaternion rotation with q performs $\boldsymbol{p}' = \boldsymbol{q}\boldsymbol{p}\boldsymbol{q}^{-1} = \boldsymbol{R}\boldsymbol{p}$, The rotation matrix can then be written as:

$$\boldsymbol{R} = \begin{bmatrix} 1 - 2(q_j^2 + q_k^2) & 2(q_i q_j - q_k q_w) & 2(q_i q_k + q_j q_w) \\ 2(q_i q_j + q_k q_w) & 1 - 2(q_i^2 + q_k^2) & 2(q_j q_k - q_i q_w) \\ 2(q_i q_k - q_j q_w) & 2(q_j q_k + q_i q_w) & 1 - 2(q_i^2 + q_j^2) \end{bmatrix} \tag{2.18}$$

For particle with initial orientation vector (0,0,1), the orientation after rotation written in quaternion (q_w, q_i, q_j, q_k) simply gives $(2(q_i q_k + q_j q_w), 2(q_j q_k - q_i q_w), 1 - 2(q_i^2 + q_j^2))$.

Appendix 2-A-2 Calculation of properties

The system reaches the steady state when physical quantities become time independent after a sufficient long time or large strain in the simulation. After the steady state is reached, the physical quantities fluctuate around the mean value. The total kinetic energy of the system consist of non-spherical particles is:

$$E_k = \frac{1}{2}\sum_{i=1}^{N} m_i v_i^2 + \boldsymbol{I}_i \boldsymbol{\omega}_i^2 \tag{2.19}$$

And the temperature of the system is then:

$$T = \frac{2E_k}{N_{dof} k_B} \tag{2.20}$$

where $N_{dof} = 2n_{dim}N - n_{dim}$ is the total degree of freedom in n_{dim} dimensions including both rotation and translational freedom. k_B is the Boltzmann constant.

The pressure of the entire system is calculated as:

$$P = \frac{N k_B T}{V} + \frac{1}{Vd}\sum_{i=1}^{N} r_i \cdot f_i \tag{2.21}$$

where V is the volume of the system, r_i and f_i is the position and the force vector of particle i. The second term is calculated from the virial theorem (Clausius, 1870). The (I, J) components of stress tensor of the system is given by (Vitek and Egami, 1987):

$$\sigma_{IJ} = \frac{1}{V}\sum_{k=1}^{N} m_k v_{kI} v_{kJ} + r_{kI} \cdot f_{kJ} \tag{2.22}$$

where I, J are x, y and z in three dimensions.

Appendix 2-B Gay-Berne potential

Appendix 2-B-1 Description of the potential

The Gay-Berne potential is used to describe the interaction between clay platelets with shape and energy anisotropy. Each clay platelet is treated as an effective oblate ellipsoid. Then the pair potential in the complete form can be written as (Coussaert and Baus, 2002; Gay and Berne, 1981; Luckhurst and Simmonds, 1993):

$$U(\boldsymbol{r}_{12}, \boldsymbol{u}_1, \boldsymbol{u}_2) = \epsilon_0 \epsilon(\boldsymbol{u}_1, \boldsymbol{u}_2, \hat{\boldsymbol{r}}_{12}) \times \varphi\left(\frac{\sigma_{ff}}{r_{12} - \sigma(\boldsymbol{u}_1, \boldsymbol{u}_2, \hat{\boldsymbol{r}}_{12}) + \sigma_{ff}}\right) \tag{2.23}$$

where $\hat{\boldsymbol{r}}_{12}$ is the unit vector along the center-to-center vector $\mathbf{r}_{12}$ between two particles, $r_{12} = |\boldsymbol{r}_{12}|$. $\boldsymbol{u}_1$ and $\boldsymbol{u}_2$ are unit vectors along the symmetry axis of particle 1 and 2. ϵ_0 and σ_0 set the energy and length scale. σ_{ff} is the particle thickness, $\sigma_0 = \sigma_{ee}$ is the particle diameter. $\varphi(y) = 4(y^{12} - y^6)$ is the dimensionless 12-6 Lennard-Jones potential. The term $r_{12} - \sigma(\boldsymbol{u}_1, \boldsymbol{u}_2, \hat{\boldsymbol{r}}_{12})$ is the previous h_{12} for distance approximation in simplified form.

Each part in Equation (2.23) is given as:

$$\sigma(\boldsymbol{u}_1, \boldsymbol{u}_2, \hat{\boldsymbol{r}}_{12}) = \sigma_0\{w(\boldsymbol{u}_1, \boldsymbol{u}_2, \hat{\boldsymbol{r}}_{12}; \chi)\}^{-1/2} \tag{2.24}$$

$$w(\boldsymbol{u}_1, \boldsymbol{u}_2, \hat{\boldsymbol{r}}_{12}; \chi) = 1 - \frac{\chi}{2}\left\{\frac{\left(\hat{\boldsymbol{r}}_{12} \cdot (\boldsymbol{u}_1 + \boldsymbol{u}_2)\right)^2}{1 + \chi \boldsymbol{u}_1 \cdot \boldsymbol{u}_2} + \frac{\left(\hat{\boldsymbol{r}}_{12} \cdot (\boldsymbol{u}_1 - \boldsymbol{u}_2)\right)^2}{1 - \chi \boldsymbol{u}_1 \cdot \boldsymbol{u}_2}\right\} \tag{2.25}$$

$$\epsilon(\boldsymbol{u}_1, \boldsymbol{u}_2, \hat{\boldsymbol{r}}_{12}) = \{1 - \chi^2(\boldsymbol{u}_1 \cdot \boldsymbol{u}_2)^2\}^{-\upsilon/2} \times w(\boldsymbol{u}_1, \boldsymbol{u}_2, \hat{\boldsymbol{r}}_{12}; \chi')^{\mu} \tag{2.26}$$

The zeros of the potential are determined by Eqs. (2.24) and (2.25). The anisotropy of the Gay-Berne potential is captured by the powers of υ and μ in Eq. (2.26), where the first factor on the right-hand side favors alignment in the direction parallel to the symmetry axis.

For discotic molecules, we follow the convention to use $\upsilon = 2$ and $\mu = 1$ (Caprion et al., 2003; Cienega-Cacerez et al., 2014; Coussaert and Baus, 2002). The aspect ratio $\kappa = \sigma_{ff}/\sigma_{ee}$ is the ratio of particle thickness (face-to-face) to particle diameter (end-to-end), $\kappa < 1$ corresponds to a discotic molecule and $\kappa = 1$ corresponds to spherical molecule. The energy ratio $\kappa' = \epsilon_{ee}/\epsilon_{ff}$ is the ratio of the corresponding well depth between the end-to-end configuration and the face-to-face configuration, then:

$$\chi = \frac{\kappa^2 - 1}{\kappa^2 + 1}, \chi' = \frac{\kappa' - 1}{\kappa' + 1}, \epsilon_0 = (1 - \chi^2)\epsilon_{ee} \tag{2.27}$$

The system considered in this work are mixtures of three type of particles A, B and C with the same thickness and different diameter, corresponding to aspect ratio κ of 1/5, 1/6, and 1/7. The slight polydispersity is introduced to avoid crystallization in mono-dispersed system. The type with the smallest aspect ratio (1/5) is used as a reference component with mass $m_A = 1$ and diameter $\sigma_{A,ff} = \sigma_0 = 1$. The energy ratio $\kappa' = 1/5$ is used for all particles.

At specific orientation, the GB potential can be simplified as a function of center-to-center distance r_{12}, the face-to-face and edge-to-edge configuration is shown in Figure 2.12. The system considers ellipsoid mixture of three different aspect ratio (particle type A, B, and C: 1/5, 1/6, 1/7) with the same population. The ellipsoids are characterized with the same thickness and different diameters determined by the aspect ratio, together with deeper potential well in face-to-face configuration determined by the energy ratio $\kappa' = 1/5$.

For interaction between different particle types, the following mixing rule is used after Cienega-Cacerez et al. (2016):

$$\epsilon_{ij} = \sqrt{\epsilon_i \epsilon_j}, \sigma_{ij} = \frac{\sigma_i + \sigma_j}{2} \tag{2.28}$$

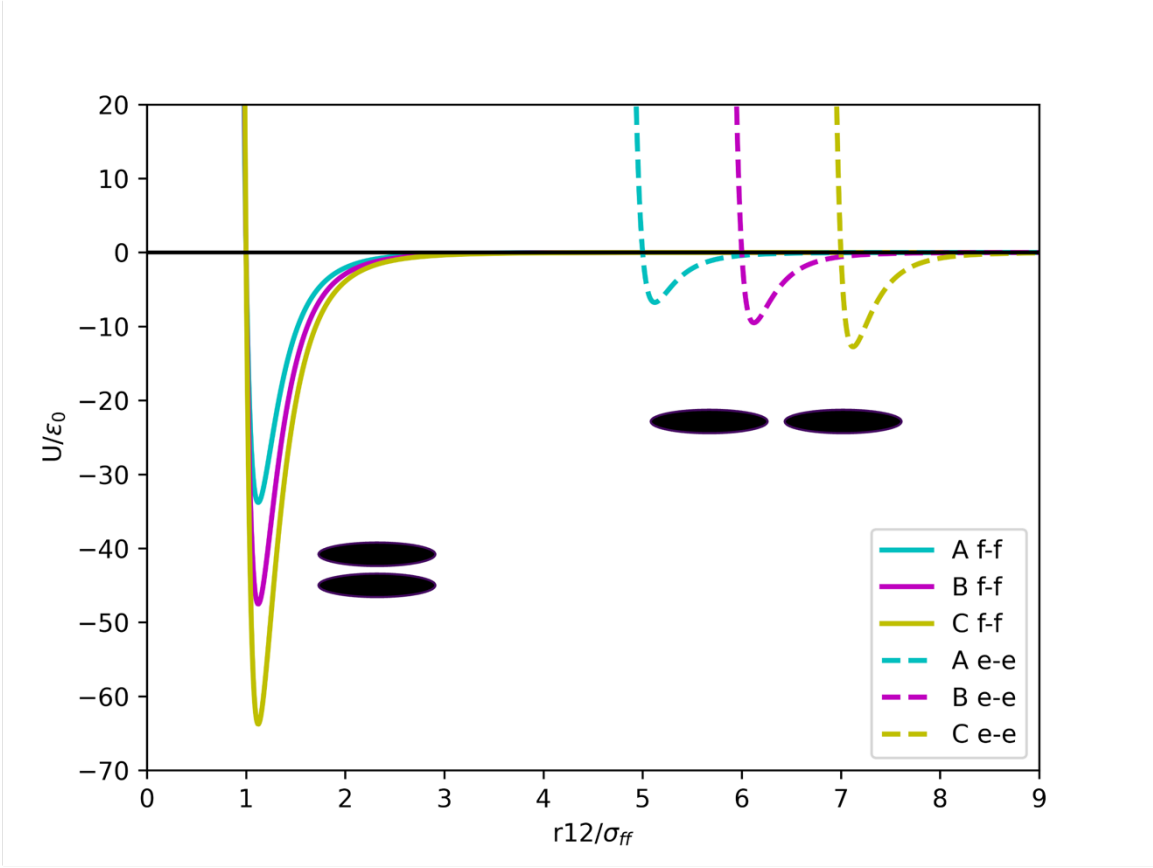

Figure 2.12: The (dimensionless) Gay-Berne potential vs the (dimensionless) distance for two typical configurations of ellipsoid particles. Three particle types (A, B, and C) correspond to the aspect ratio of 1/5, 1/6 and 1/7, respectively. Solid lines represent the potential for face-to-face configuration, labeled with "f-f" in the legend. Similarly, dashed lines represent potential for edge-to-edge configuration, labeled with "e-e". The energy ratio between the two configurations ("e-e" and "f-f") is 1/5 for all the particles. In these specific configurations, the GB potentials is a function of separating distance r only.

Appendix 2-B-2 Unit of the simulation

The distance scale is 7.5×10^{-9} m (7.5 nm) corresponding to the diameter of the ellipsoid type A.

The mass scale is 8.77×10^{-23} kg calculated from molecular mass. Shen & Bourg used a unit cell with molecular formular $Si_8Al_{(3.2)}Mg_{(0.8)}O_{20}(OH)_4$, the molar mass of the unit cell is 718.48 g/mol. 54 cell is used to build a hexagonal platelet with diameter of 6 nm, giving a molar mass of 38.7979 kg/mol. In the current study, we assume the diameter of a model clay ellipsoid is

about 7 nm excluding the thickness of water layer. The molar mass is then 38.7979*(7/6)^2=52.81 kg/mol assuming the same density, the unit mass of a single particle is then 8.77×10^{-23} kg. Considering the volume of an ellipsoid is $V_{ellipsoid} = \frac{4}{3}\pi abc$, where a, b, c is the length of the three semiaxis. Particle type A have a volume of ~4.42×10^{-26} m^3, this gives a unit density of ~1985 kg/m3, which is comparable with the macroscopic dry density of 800~2000 kg/m^3 for montmorillonite (Torikai et al., 1996).

The energy ratio is 0.0148 eV calculated from $\epsilon_0 = (1-\chi^2)\epsilon_{ee}$, where ϵ_{ee} is 0.1 eV, ϵ_{ff} is 0.5 eV for energy ratio of 1/5 from particle type A. The time scale is ~1.44×10^{-9} s (1.44 ns) calculated from $\tau_0 = \sqrt{\frac{m_0\sigma_0^2}{\epsilon_0}}$.

Appendix 2-C Schematic figure of PaRDF

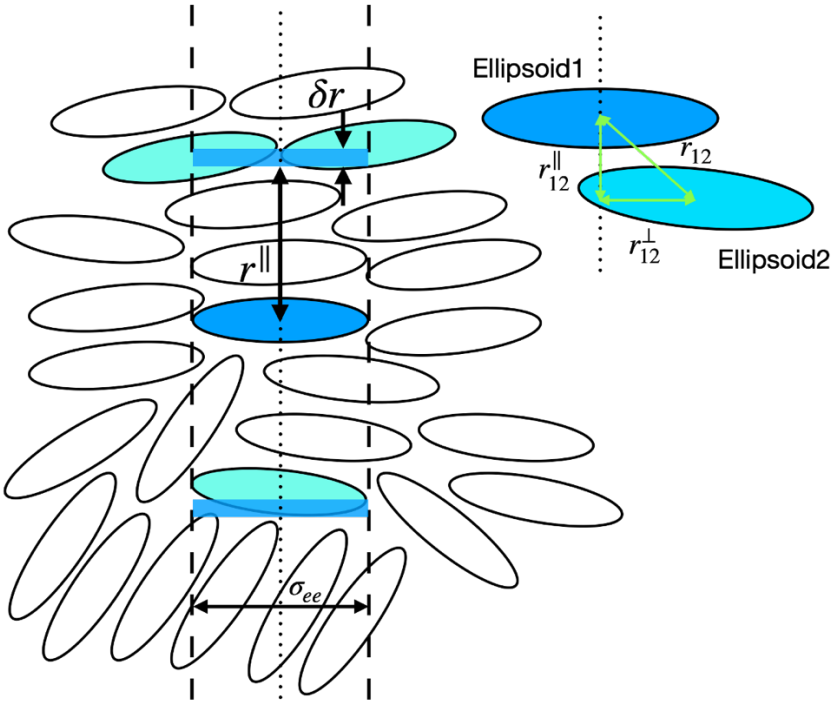

Figure 2.13: A schematic figure of the parallel radial distribution function (PaRDF). The PaRDF gives the normalized probability density of finding another particle (in cyan) along the symmetry axis direction ($r_{12}^{\parallel}$) of the center particle (in blue) at the distance of r. The higher the probability, the higher the peak in the PaRDF. The search is restricted inside a column region where σ_{ee} is the diameter of the searching column.

Appendix 2-D Compression and shear configuration at normal stress of 33.71 MPa

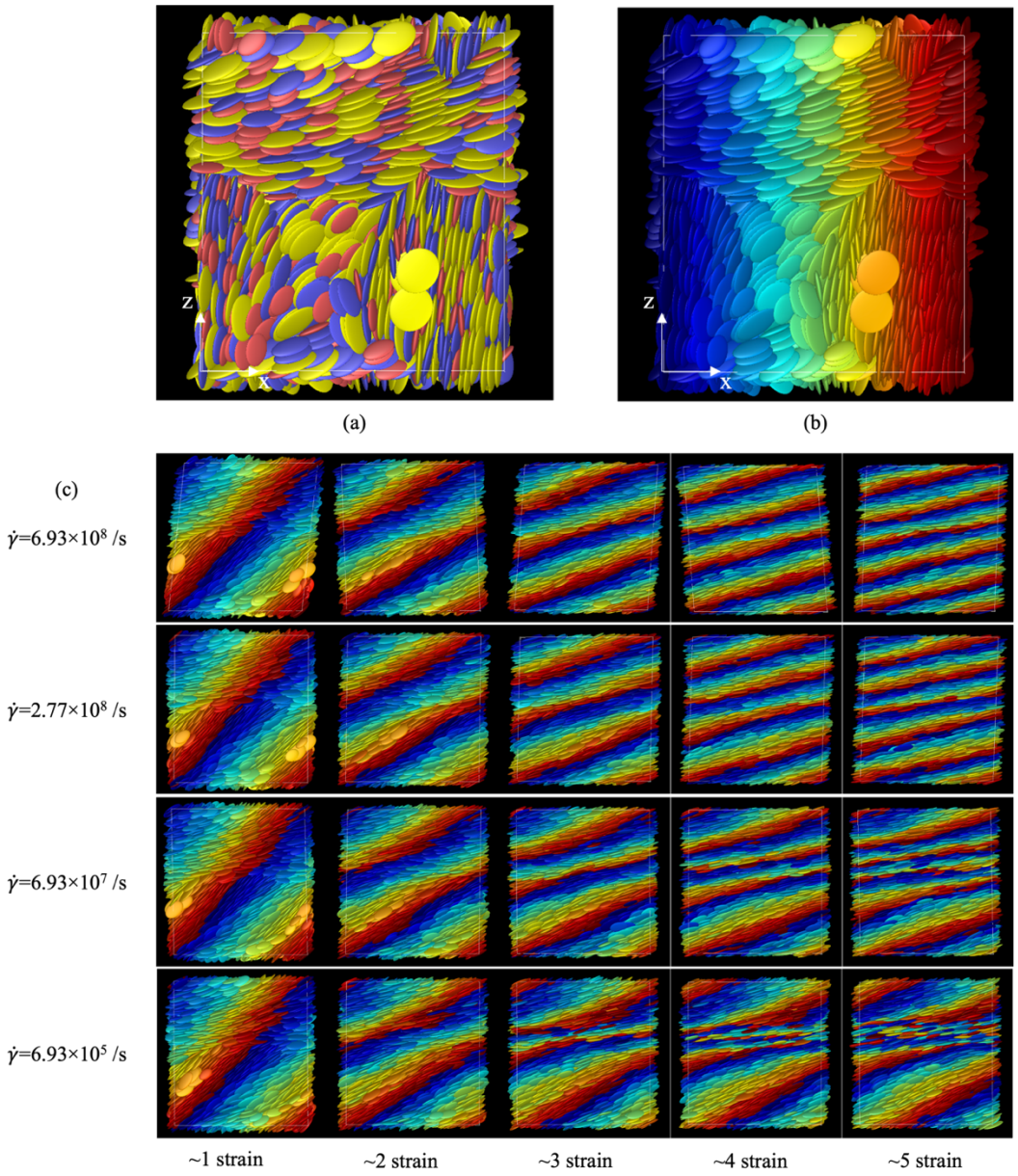

Figure 2.14: Compression and shear configurations at normal stress P = 33.71 MPa, a view on the XZ plane similar to Figure 1. (a) Compressed system colored by different particle aspect ratio, where red, blue, and yellow correspond to particle aspect ratio of 1/5, 1/6, and 1/7. (b) Mixture system colored by the x coordinate of particles at strain of 0, the same coloring is used for (c). (c) Two scenarios are observed with homogeneous shear at high strain rate ($\dot{\gamma} \geq$ 2.77×10^8 /s) and the shear band at low strain rate ($\dot{\gamma} \leq$ 6.93×10^7 /s). Shear localization appear after the strain of 2 and is more obvious at lower strain rate. The highest

shear rate that can exhibit shear band is 10 times higher than that at normal stress P = 5.62 MPa in Figure 1.

Appendix 2-E Correction in strain rate with shear localization

Shear localization is observed at some low strain rate and high normal stress conditions. Thus, the true strain rate should be higher within the sheared zone. In Figure 2.6, we show that the zone of shear localization is associated with the zone of preferred particle orientation (~10°), here the thickness of the preferred orientation zone is used to represent the thickness of the sheared zone in further analysis. The corrected strain rate is defined as:

$$\dot{\gamma}_c = \dot{\gamma} \frac{L_z}{L_{band}} \tag{2.29}$$

where L_z is the total box height and L_{band} is the band thickness at the strain of 10.

The shear stress as a function of corrected strain rate is plotted in Figure 2.15(a). The vertical dashed line shows the applied strain rate before correction and corrected points shifted to the right with higher strain rate. The shear stress-strain relationship is then fitted with Herschel-Bulkley model (Equation 2.12), the residual shear stress and the exponent as a function of normal stress is shown in Figure 2.15. The correction in strain rate do not significantly change the previous result. The residual shear stress shows similar increasing trend with normal stress while the value at the largest normal stress is more underestimated. The exponent n shows a similar decreasing trend with normal stress and the slope is smaller after correction.

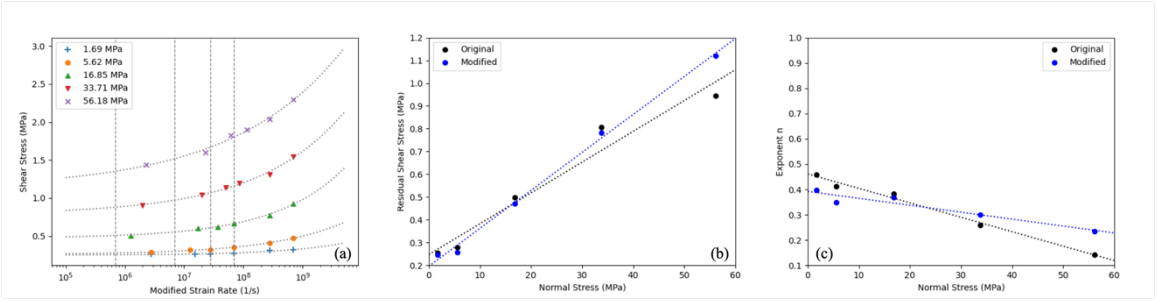

Figure 2.15: (a) Shear stress as a function of modified strain rate at different normal stresses, fitted with Herschel-Bulkley model. Dashed vertical line is the applied strain rate before correction. (b) The original and modified yield stress both increase with normal stress. The dotted line is the approximation with a linear model. (c) The original and modified exponents both decrease with normal stress. The dotted line is the approximation with a linear model.

Appendix 2-F Preferred particle orientation

The structural change can be also probed by the average particle orientation. The angle between the Z axis and the symmetry axis of particle is projected on the XZ plane and the YZ plane. These angles are then averaged for all the particles and denoted by θ_{xz} and θ_{yz}, respectively. The evolution of θ_{xz} and θ_{yz} is shown in Figure 2.16. We find that θ_{xz} approaches 10° at higher strain rate, whereas the angle θ_{yz} approaches 0°. Contrastingly, Brownian dynamics simulation with the Gay-Berne potential at high porosity (72%) shows that both θ_{xz} and θ_{yz} approach 0° at high strain rate (Yamamoto et al., 2005). The difference may be attributed to the dilute configuration, at which the particles rotate and wag. Recent simulation on spherocylinder suspension shows that the elongated particles tend to align with the flow direction (θ_{xz} = 0°) at high porosity (Marschall et al., 2020), while the aligned direction is associated with particle shape at denser system (Börzsönyi et al., 2012; Marschall et al., 2020, Nagy et al., 2017). Particle alignment was also reported in a shear experiment (Haines et al., 2013), it suggests phyllosilicate particles rotate to the orientation perpendicular to the maximum principal stress.

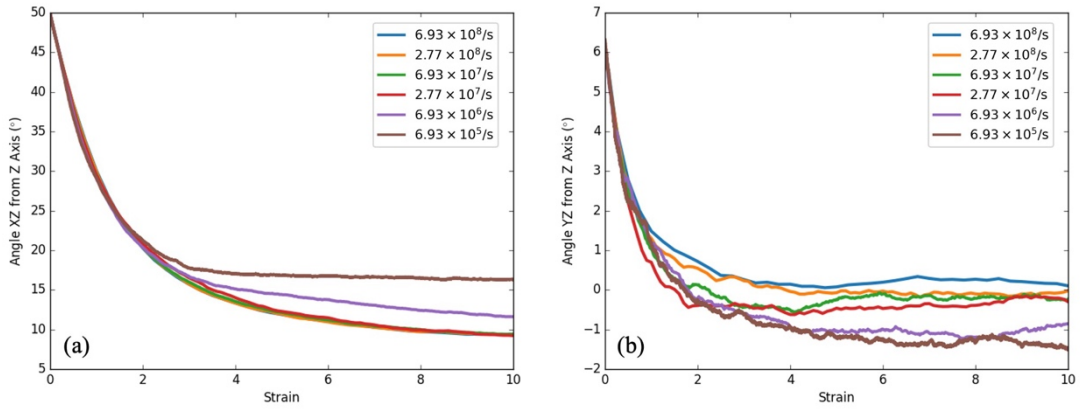

Figure 2.16: Example of angle between the director and the Z-axis as a function of shear strain for all strain rates at the normal stress of 5.62 MPa. (a) The angle between the director and the Z-axis approaches 10° in the XZ plane and (b) approaches 0° in the YZ plane at high strain rate.

Appendix 2-G Effect of normal stress on the shear process

The effect of strain rate on the shear process at the normal stress of 5.62 MPa is given in Figure 2.3. Here, the shear stress and porosity change as a function of strain at different normal stress is given to provide more information on the shear process (Section 2.4.3).

At the low strain rate, the peak in shear stress is reached near the strain of 2. Increasing the

normal stress increased the absolute value in shear stress but did not significantly after the position of the peak (Figure 2.17(a)). Compaction in stage 1 also agrees with the proposed shear process.

At high strain rate, the position of stress peak is clearly advanced to earlier strains comparing to low strain rate (a). The advance is clearer at low normal stress, while peak is closer to the original value near the strain of 2 at higher normal stress (Figure 2.17(b)). The stress peak is close to the dilation (porosity increase) at early strain. Further compaction continues to a longer strain comparing to the low strain rate where the structural change slows down near the strain of 2. Combining with a more homogeneous shear from shear band analysis in Figure 2.10, these features suggest the proposed shear process dividing stage 1 and stage 2 do not apply to higher strain rate.

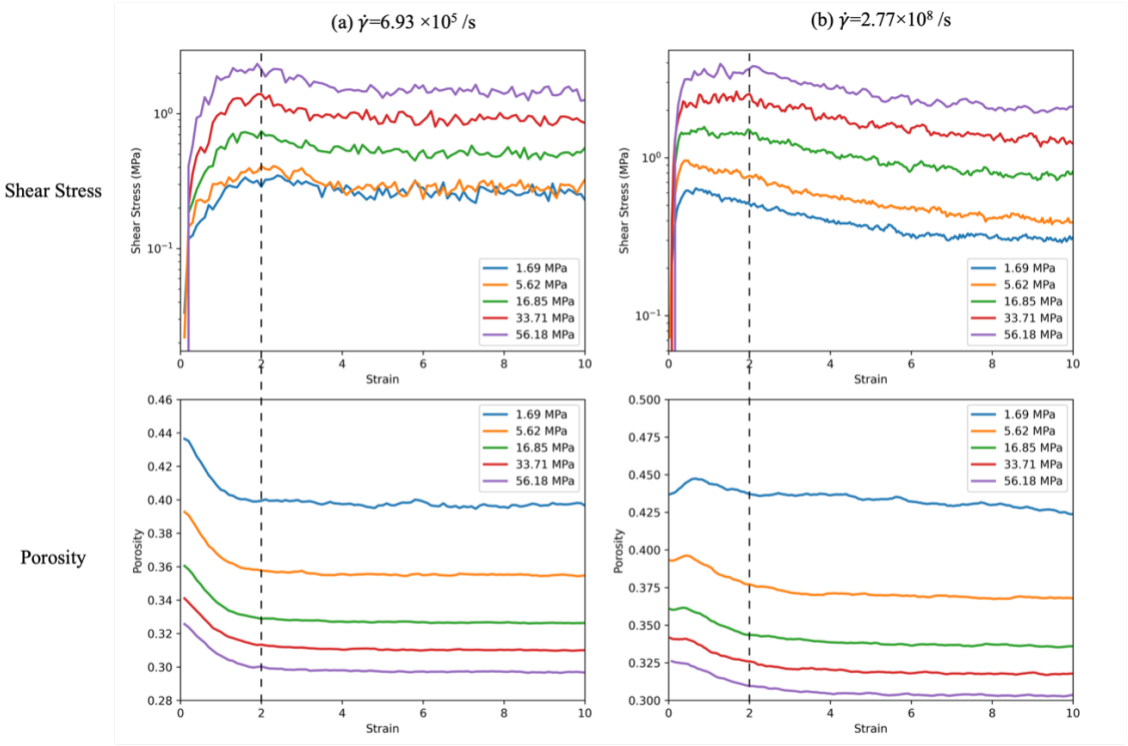

Figure 2.17: The change in shear stress and porosity as a function of strain at (a) low strain rate ($\dot{\gamma}$ = 6.93×10^5 /s) and (b) high strain rate ($\dot{\gamma}$ = 2.77×10^8 /s). The changes at different normal stress are shown in different colors.

3 The effect of normal stress and energy anisotropy in a 2D system

3.1 Introduction

3.1.1 Shortcomings of the 3D model

The simulation in Chapter 2 performed constant strain rate shear in three dimensions. During shear, particles rearrange and align with the flow. The average angle between the Z-axis and the symmetry axis of particles reached approximately 10° in XZ plane and near 0° in YZ plane. While the particle orientation at low strain rates slightly deviates from these values due to shear banding, the overall change indicates 3D structures such as aggregation and flocculation are largely reduced after shear. This suggest the shearing oblate ellipsoid in 3D system may be comparable to shearing ellipse in 2D system if we only focus on the change in shear plane XZ.

Despite the loss of degrees of freedom associated with the Y direction, 2D simulations can reduce the overall computation cost. This allows for simulations with larger system size and averaging over more samples to provide a better understanding of the shear behavior.

3.1.2 Effect of energy anisotropy

The GB potential has been proved to be a useful tool in capture some important behavior of smectite in both compression and shearing. A remaining task is to examine if the GB potential can be directly applied to other plate-like phyllosilicate minerals by adjusting the shape and interaction anisotropy.

As phyllosilicate minerals differ in composition and properties, we focus on illite as it shares a similar T-OT structure with smectite. Both smectite and illite are commonly observed in subduction zones with smectite abundant in the shallow region at low temperature. With increasing depth and temperature, smectite can react with Al^{3+} and K^{+} cations to form illite-smectite mixed-layer minerals and ultimately illite. Illite minerals have a higher surface charge density and can form larger and more stable aggregate compared to montmorillonite (Nadeau, 1985). Recent full atomistic MD simulations shows illite have a stronger mid-range negative potential of mean force comparing to montmorillonite (Zhu et al., 2022). Thus, illite platelets may be represented by GB potential with a larger potential well.

Studies on frictional behavior of simulated gouge using quartz, illite and montmorillonite shows overall strength decreases with clay content in saturated condition while illite has a higher friction of coefficient comparing to montmorillonite (Tembe et al., 2010). The structure of clay minerals during shear can be probed using the X-ray texture goniometry (XTG) method. The alignment of particles is quantified with fabric intensity. Shear

experiments on dry montmorillonite shows fabric intensity increases during shear in the first strain of 5 and then reaches a steady state. The overall fabric intensity increases with normal stress. Crushed illite shale has a slightly higher fabric intensity than montmorillonite under the same normal stress.

3.1.3 The objective of this chapter

Based on the result from Chapter 2 and previous studies, we perform constant strain rate shear in a 2D system, focusing on the effect of normal stress and energy anisotropy. We find that the 2D system is characterized by cluster movement at low normal stress and particle alignment increase at high normal stress. The cluster movement is more obvious with high energy anisotropy. In Section 3.2, we present the setup of the 2D model with improvement based on 3D. In Section 3.3, we present the shear result for different normal stress, strain rate and energy anisotropy. In Section 3.4, we discuss the shear results including comparison with 3D system. In Section 3.5, we summarize the results.

3.2 Method

3.2.1 Gay-Berne parameter

We conduct constant strain rate shear in a 2D system with focus on the shear plane. Several simulation setup and model parameters are improved or modified comparing to the 3D system in Chapter 2.

We use ellipse with aspect ratio of 1/4, 1/5, and 1/6 with the same thickness σ_0. The effect of energy anisotropy is investigated by using the same well depth in edge-to-edge configuration and change energy ratio κ'. A lower energy ratio gives a deeper potential well in face-face configuration. We use default energy ratio of 1/4, 1/5, and 1/6 assuming the energy anisotropy increases with the particle diameter for clay platelets (Ebrahimi et al., 2014). The energy ratio of 1 is used for low anisotropy cases and 1/8, 1/10, and 1/12 for high anisotropy cases.

The choices of parameter (υ, μ) in Equation (2.26) used to calculate interaction anisotropy are changed to (1, 2), following the convention for probate ellipsoid (Luckhurst and Simmonds, 1993; de Miguel et al., 1996). The particle type with aspect ratio 1/5 and energy ratio 1/5 is used as a reference component with mass = 1 and soft contact distance σ_0 = 1.55 nm. The potential well of $1.342\varepsilon_0$ in face-face configuration corresponds to the free energy of 0.5 eV in full atomistic simulations near the second layer of crystalline hydrates (Shen & Bourg, 2011). The Gay-Berne parameters used in the 2D simulation are given in Table 3-1.

Parameters	Value
Length scale σ_0 (nm)	1.55
Particle thickness σ_{ff} (nm)	1.55
Particle diameter σ_{ee} (nm)	6.2, 7.75, 9.3
Aspect ratio κ	1/4, 1/5, 1/6
Energy scale ϵ_0 (eV)	0.3726
Energy ratio κ'	1/4, 1/5, 1/6 (default)
	1,1,1 (low anisotropy)
	1/8, 1/10, 1/12 (high anisotropy)

Table 3-1 2D Gay-Berne potential parameters.

3.2.2 Simulation setup

Translational and rotational equations of motion are integrated using the velocity Verlet algorithm with a dimensionless time step $\delta t^* = 0.01$ if not specified. To optimize the computational time, the interaction potentials are truncated at a cutoff of $7\sigma_0$.

The initial condition is created with 2500 particles (three types with similar population) on the simple square 2D lattice. Eight samples with different initial structures are prepared. The samples are compressed to designed dimensionless normal stress P*= 0.1, 0.3, 0.6, 1, 2, 3 (P= 1.60, 4.81, 9.82, 16.03, 32.06, 48.09 MPa) following the similar procedures as in 3D case from Section 2.2. After equilibrium at each normal stress, the system is sheared at different strain rate $\dot{\gamma}^*$ = 0.0001, 0.0004, 0.001, 0.004, 0.01 (1.68×10^6, 6.72×10^6, 1.68×10^7, 6.72×10^7, 1.68×10^8 /s) for 20 strains. The following results are reported in real unit for comparison with experimental data. The main results focused on case with default energy ratios of 1/4, 1/5 and 1/6 at the lowest strain rate 1.68×10^6 /s. The effect of energy anisotropy is discussed separately.

3.3 Result

3.3.1 Development during shear

Figure 3.1 shows an example of configuration at the shear strain of 20 at the lowest strain rate (1.68×10^6 /s) under different normal stress. The color coding represents the absolute value of the angle between the symmetry axis of the particle along the thickness direction and the Y-axis. At low normal stress, particles with similar orientations form clusters and persist even after significant strains. However, at higher normal stress, these clusters gradually disappear as particles align more with the flow. The cluster formation at low normal stress is not observed in 3D systems at similar normal stress.

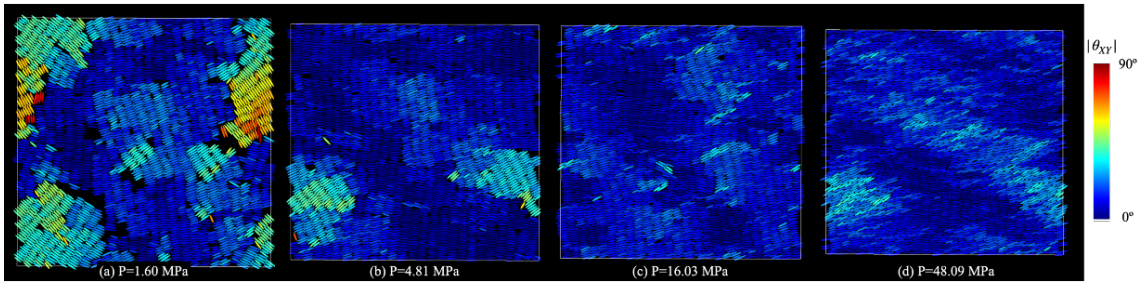

Figure 3.1: An example of shear configuration after the shear of 20 strain at the lowest strain rate of 1.68×10^{6} for normal stress (a) 1.60, (b) 4.81, (c) 16.03, and (d) 48.09 MPa. The color represents the absolute value of the angle between the symmetry axis of the particle along the thickness direction and the Y axis.

Figure 3.2(a) shows the shear stress evolution during a shear strain of 20 at the lowest strain rate 1.68×10^{6} /s, with values time-averaged every 1×10^{4} step. The results for eight samples are shown in different colors, with the black line indicating the sample-averaged value. For normal stress greater than 1.6 MPa, shear stress initially rise to a peak and then gradually decrease to a residual value. It should be noted that the peak shear stress occurs near the strain of 200% in 3D cases, while the peak stress is reached near 400% in 2D cases. At the lowest normal stress of 1.60 MPa, the peak stress appears earlier, with less pronounced peak and subsequent decrease.

The change in volume fraction during shear is shown in Figure 3.2(b). The system shows large fluctuation in volume fraction at the lowest normal stress P=1.60 MPa. The volume fractions continue to increase after the peak in shear stress is reached. These fluctuations are suppressed at higher normal stress, where the position of the shear stress peak is close to the strain at which the residual volume fraction is reached. Thus, the shear development for shear stress and volume fraction at high normal stress is generally consistent with 3D results at low strain rates.

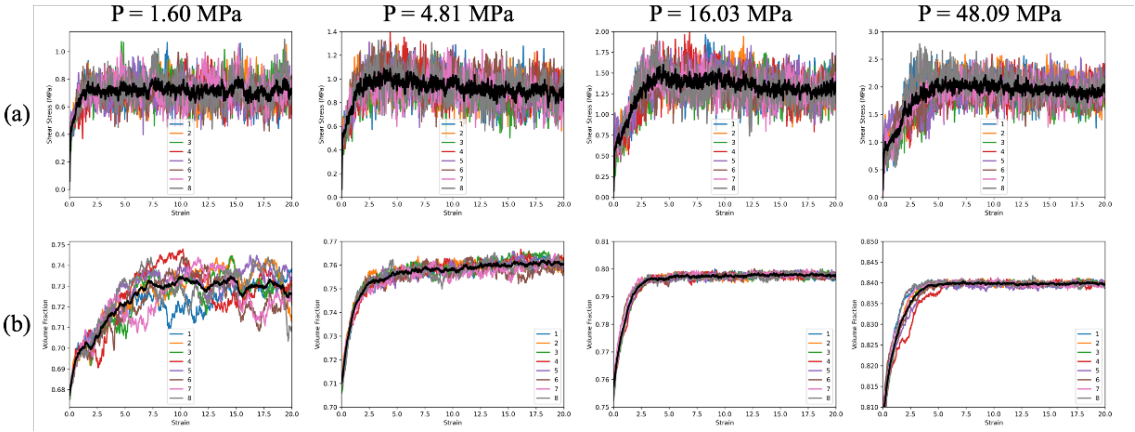

Figure 3.2: Evolution of (a) shear stress and (b) volume fraction during shear at different normal stress at the strain rate 1.68×10^{6}. The value is averaged every 1e4 step for eight samples marked in different color. The black line is the average value over eight samples for each case.

3.3.2 Steady-state rheology

Figure 3.3(a) summarizes the steady-state shear stress as a function of strain rate at different normal stresses. The data indicate that shear stress increases with both strain rate and normal stress, consistent with 3D cases. The shear stress-strain rate relation is fitted with the HB model (Equation 2.7). Residual shear stress increases with normal stress from 0 to about 1.75 MPa. At normal stress lower than 9.62 MPa, the apparent friction coefficient at low normal stress is about 0.126 while the slope is smaller at 0.0188 at higher normal stresses. The exponent n increases with normal stress from 1.60 to 32.06 MPa but decreases when normal stress further increases to 48.09 MPa.

To describe the volume fraction as a function of strain rate, we adopt a power function similar to the HB model in the form:

$$\varphi = \varphi_0 - K_\varphi * \dot{\gamma}^{n_\varphi} \tag{3.1}$$

where φ_0 is the residual volume fraction at zero strain rate limit. The volume fraction increases with normal stress but decreases with strain rate (Figure 3.3(d)). The residual volume fraction gradually increases with normal stress, with the slope slightly decreasing at higher normal stress without out a clear stepwise change. The exponent n_φ increases with normal stress and then decreases at the highest normal stress. The overall trends for both the residual value and the exponent are similar to the change in shear stress.

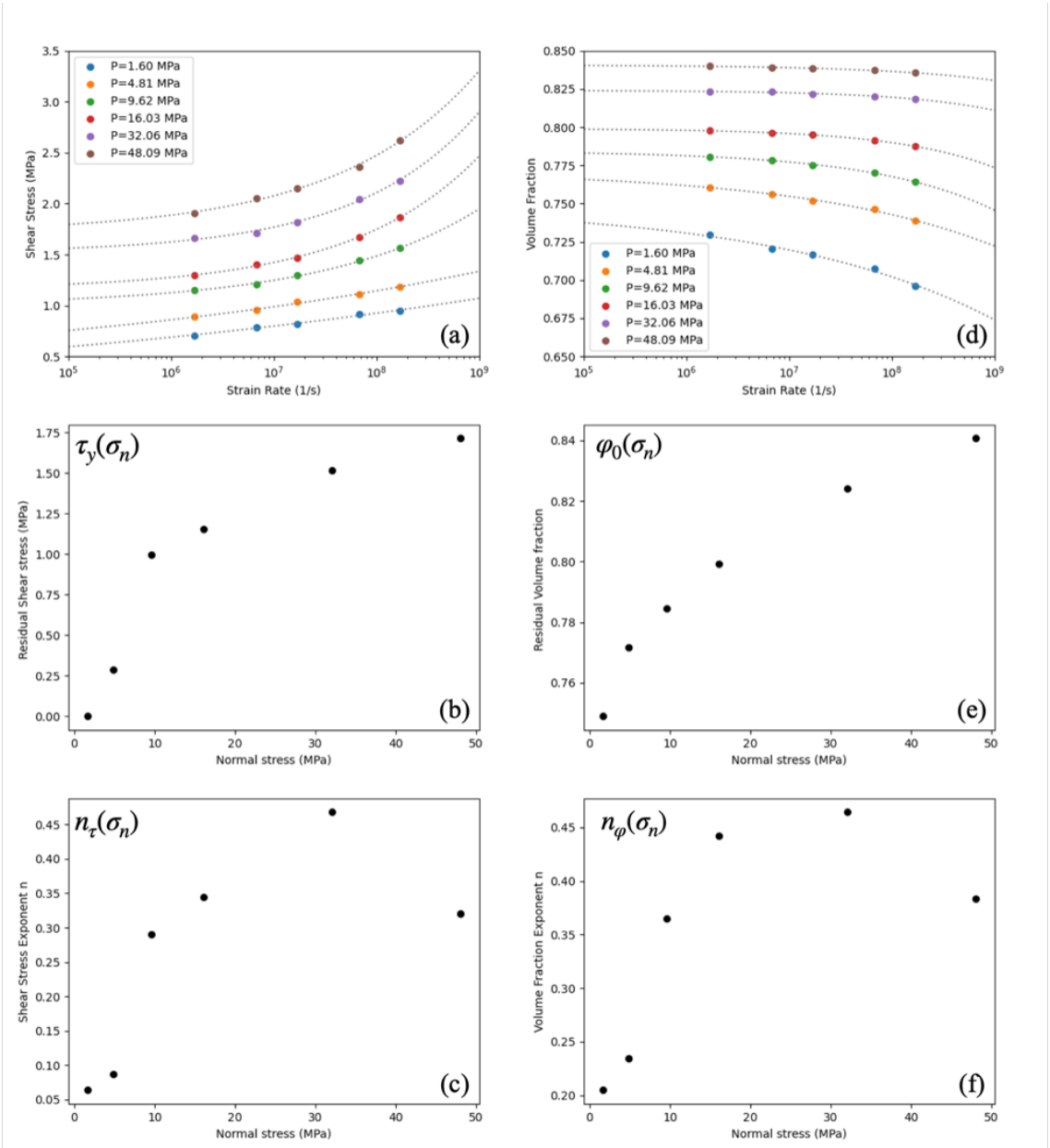

Figure 3.3: The shear stress and volume fraction both can be described with power law function of strain rate. (a) The shear stress as a function of strain rate at different normal stress, fitted with Herschel-Bulkley model. (b) The residual value and (c) exponent as a function of normal stress. (d) The volume fraction as a function of strain rate at different normal stress, fitted with a power function similar to the Herschel-Bulkley model with (e) the residual value and (f) the exponent.

Figure 3.4(a) shows the friction coefficient (the ratio of shear stress and normal stress) as a function of normal stress at different strain rate. The friction coefficient generally decreases with normal stress and increase with strain rate at each normal stress level. At the lowest

normal stress of 1.60 MPa, the friction coefficient increases from above 0.4 to about 0.6 with increasing strain rate. In contrast, the highest normal stress of 48.09 MPa, the friction coefficient is as low as 0.05 with minimal variation upon changing the strain rate.

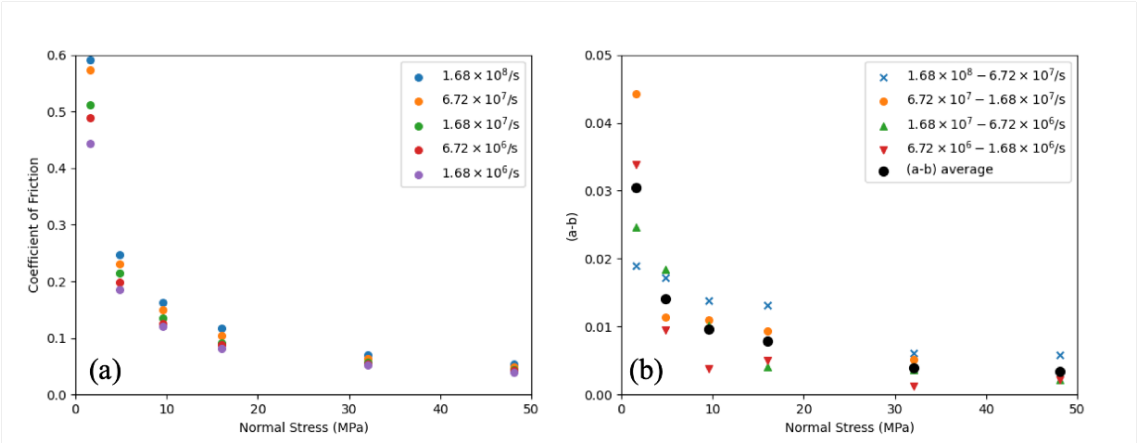

Figure 3.4: (a) The friction coefficient and (b) The velocity dependence of friction (a-b) as a function of normal stress at different strain rate.

The velocity dependence of friction (a-b) decreases with increasing normal stress (Figure 3.4(b)). According to the Herschel-Bulkley model, (a-b) increases with strain rate and decreases with normal stress with positive K and n parameter. For normal stress higher than 10 MPa, the velocity dependence increases with strain rate. However, the trend is not clear at lower normal stress.

3.3.3 Structure analysis

3.3.3.1 Particle orientation

The particle orientation is defined as positive when opposite to the shear direction. Figure 3.5 shows the distribution of particle angles from strain 16 to 20 at the lowest strain rate (1.68×10^{6} /s). The particle angle is stored every 0.1 strain and averaged over eight samples. The dotted line indicates the angle of 0. At the lowest normal stress of 1.60 MPa, particle angles are widely distributed in all directions, with a most probable value of ~3°, which is close to 0. As normal stress increases, the most probable orientation shifts leftward to a positive value to ~7° at 4.81 MPa and to approximately 11.5° at higher normal stress. For normal stress greater than 9.62 MPa, the most probable angle does not change significantly. Additionally, the distribution become narrower with peak value higher at large normal stress. A similar change in orientation was observed by Marschall et al. (2020) for athermal frictionless spherocylinder in suspension. The most probable orientation shifts from 0 to a positive value

with increasing volume fraction. The preferred orientation for particles with the aspect ratio of 5 is about 10° which resembles the value found in this study. However, the overall distribution become wider with lower peaks at larger volume fraction, which is opposite to the result in this study.

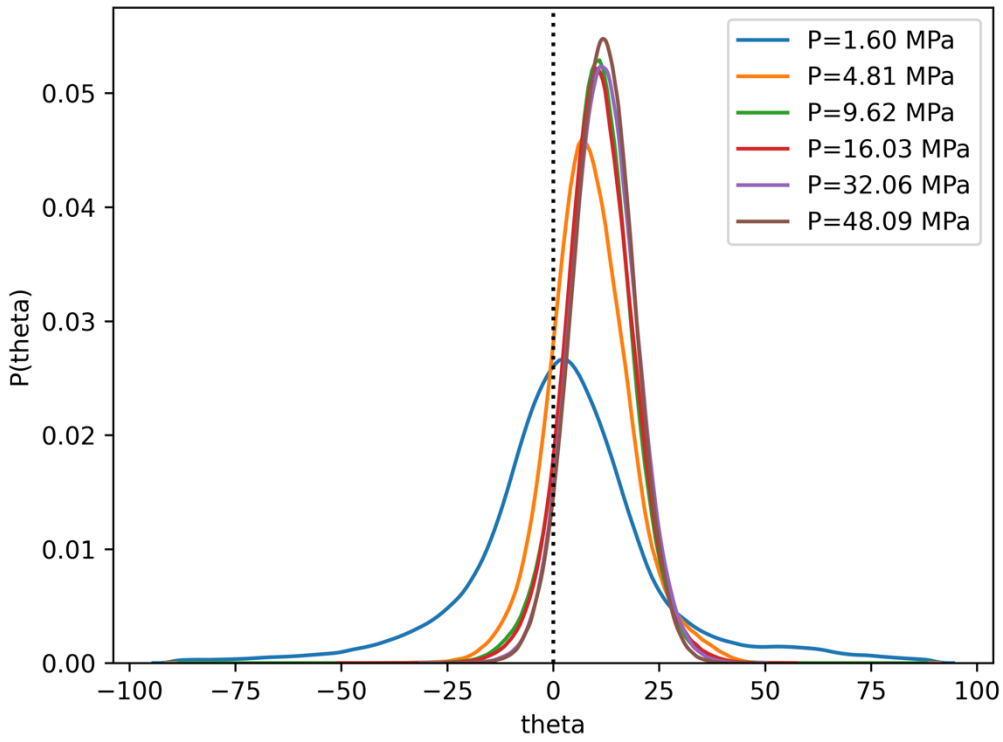

Figure 3.5: The probability density distribution for a particle to be oriented at angle theta at the lowest strain rate 1.68×10^{6}/s for different normal stress. The distribution is taken for strain 16-20 every 0.1 strain for all eight samples. Particle angle of 0 is shown in the dotted line.

3.3.3.2 Radial distribution function

The parallel radial distribution is used to examine the structure of the ellipsoid system along the symmetry axis of particles. Figure 3.6 shows the PaRDF at strain 20 for all eight samples at the shear strain of 20. Higher peak values indicate a greater probability of finding another particle at the corresponding distance along the axis direction. The difference in PaRDF between samples are neglectable, with consistent peak positions and heights. The system shows a short-range positional correlation in the parallel direction at the normal stress of 4.81 MPa (Figure 3.6 (a)). A total of 14 peaks occurred regularly for to a distance of 16, with peak

height decrease from above 8 to near unity. At the higher normal stress of 48.09 MPa, only 6 peaks remained, with peaks split into two starting from the second peak onwards (Figure 3.6 (b)). The results suggest the original column-like stacking in the parallel direction is largely reduced at high normal stress. This peak split is caused by "interdigitation" at high normal stress where particles from neighboring column entering the spacing of the original column (Cienega-Cacerez et al., 2014).

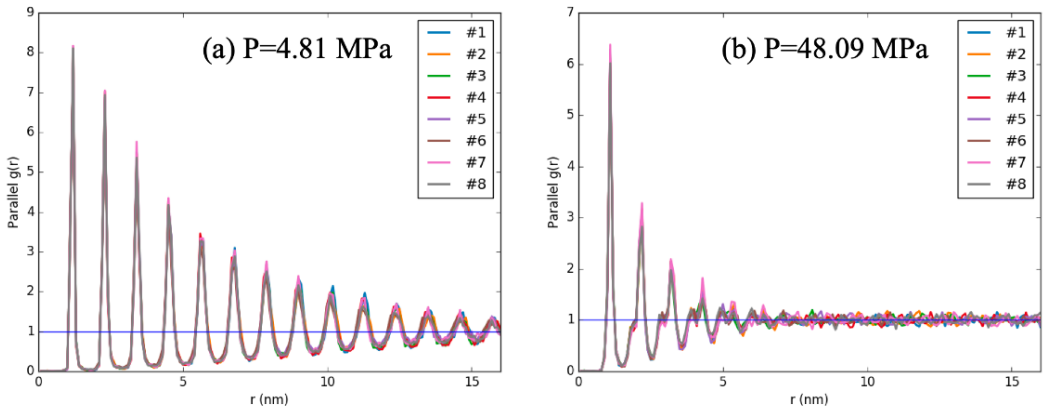

Figure 3.6: The parallel radial distribution in the distance range 0 to 16 at the shear strain of 20 for all eight samples at normal stress (a) 4.81 MPa and (b) 48.09 MPa.

The sample-averaged peak values at strain 20 were extracted for different normal stresses. Only peak value higher than 1.2 is considered as peak heights at larger distance are small and indistinguishable from fluctuations. For split peaks at high normal stress, only the higher peak values are considered. The extracted PaRDF peaks as a function of radius for different normal stress is given in Figure 3.7 (a). The decreasing PaRDF is fitted with Equation (2.9). Generally, the peak height decreases with increasing normal stress, and peak positions shift inward, suggesting compression in axis parallel direction at high normal stress. The characteristic stacking size increases with normal stress from 1.60 MPa to 9.62 MPa and then decrease at higher normal stress (Figure 3.7 (b)).

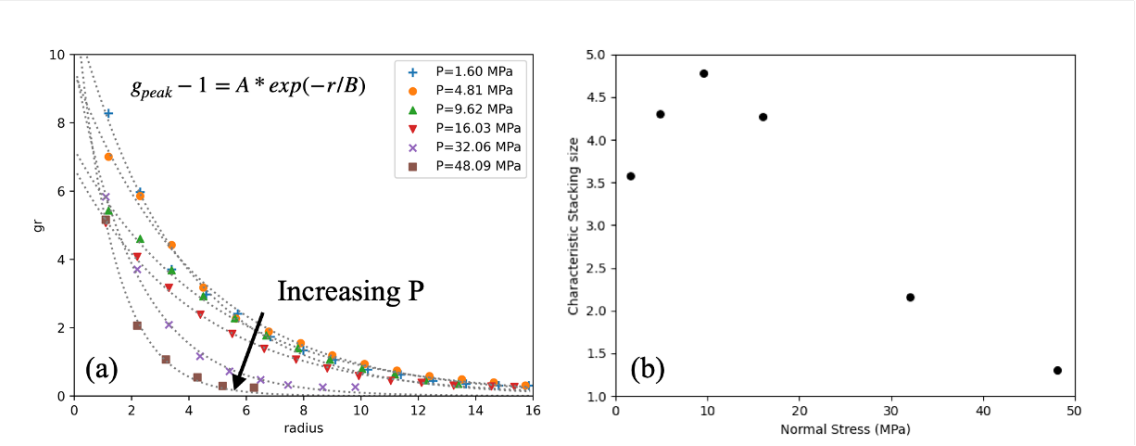

Figure 3.7: The effect of normal stress on PaRDF. (a) The extracted peak values of PaRDF at strain 20 for different normal stress and the characteristic stacking size as a function of normal stress. The data is averaged over all eight samples. The relation is fitted with the exponential function in Equation (2.9). (b) The characteristic stacking size first increases from 3.5 to 5.0 with normal stress and then decreases to below 1.5 at higher normal stress.

3.3.4 Effect of energy ratio

3.3.4.1 Rheology

Figure 3.8 shows that larger energy anisotropy results in higher shear stress, consistent across different normal stress and strain rate applied.

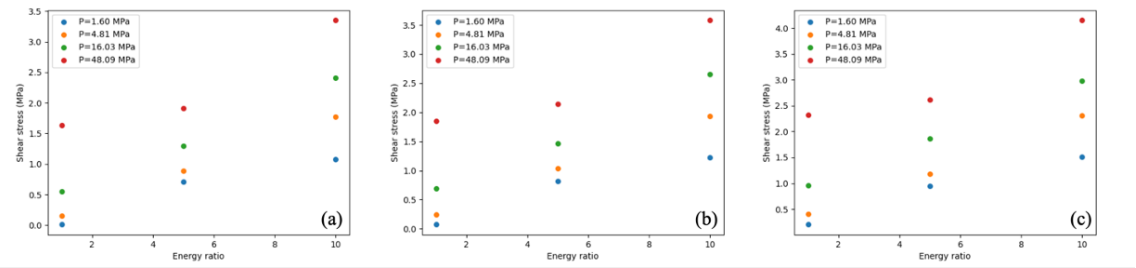

Figure 3.8: Shear stress as a function of energy ratio at different normal stress for strain rate (a) 1.68×10^{6}, (b) 1.68×10^{7}, and (c) 1.68×10^{8} /s.

Shear stress increases with both normal stress and strain rate for all three energy ratio values and can be described by the HB model (Figure 3.9). The residual shear stress also increases with normal stress for all energy ratios, with higher energy ratio resulting in higher residual shear stress. For energy ratio of 1 and 1/4-1/5-1/6, the residual value is near 0 at the lowest normal stress 1.60 MPa (Figure 3.9 (d)).

While Herschel-Bulkley model fits the shear stress-strain relationship well, the exponent n does not show clear relationship with either normal stress or energy ratio. All exponents are smaller than 1, suggesting shear-thinning behavior. For energy ratio of 1/8-1/10-1/12, a drop in exponent n occurs at the normal stress of 16.03 MPa, For energy ratio of 1, the exponent value at the lowest normal stress 1.60 MPa is relatively high. Despite these specific points, the exponent generally increases with normal stress.

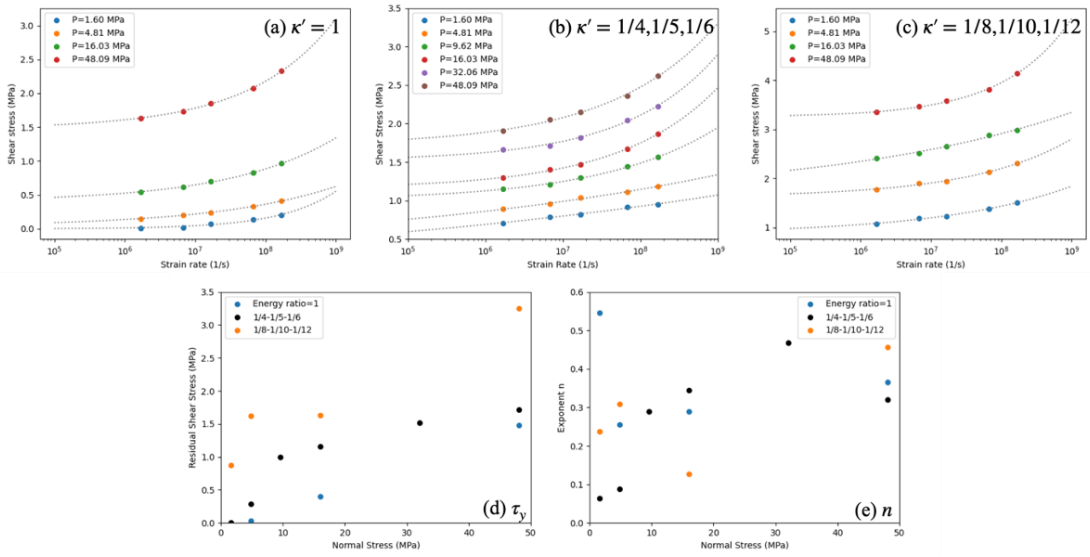

Figure 3.9: The shear stress as a function of strain rate fitted with Herschel-Bulkley model for energy ratio of (a) 1, (b) 1/4-1/5-1/6, and (c) 1/8-1/10-1/12. (d) The residual shear stress and the (e) the exponent as a function of normal stress.

3.3.4.1 Structure

Figure 3.10 shows the examples of shear configuration after shear for different energy ratio at a normal stress of 1.60 MPa and strain rate of 1.68×10^{6}/s. For energy ratio of 1, high particle alignment is achieved at low normal stress similar to structure at high normal stress condition for energy ratio of 1/4-1/5-1/6 as shown in Figure 3.1. As energy anisotropy increases, particles form clusters with neighboring particles of similar orientation. Defining a clear boundary between clusters can be challenging due to the presence of local topological defects connecting misaligned particles. Systems with higher energy anisotropy also exhibit larger pore space between misaligned particles while system with smaller energy anisotropy is denser.

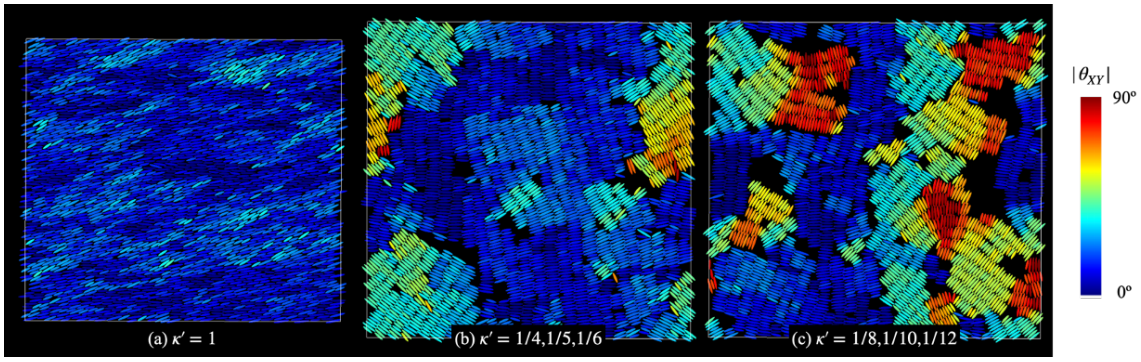

Figure 3.10: Examples of shear configuration after shear at normal stress of 1.60 MPa and strain rate of 1.68×10^{6} /s for energy ratio (a)1, (b)1/4-1/5-1/6, (c) 1/8-1/10-1/12.

Figure 3.11(a) shows the nematic order averaged over the strain of 16 to 20 from the lowest strain rate 1.68×10^{6} /s for different normal stresses and energy ratios. The Energy ratio of 1 achieves the highest nematic order, exceeding 0.9, and is not significantly affected by the normal stress. In contrast, system with larger energy ratio show a clear increasing trend in nematic order with normal stress. Although larger energy ratios result in lower nematic order, all cases can reach similar nematic order at sufficiently high normal stress.

Figure 3.11(b) shows the average particle orientation as a function of normal stress. The horizontal dashed line represents an ideal value of 11.4° at 48.09 MPa with energy ratio of 1. The average orientation close to the ideal value can be achieve at low normal stress at the energy ratio of 1, whereas larger energy ratios show an increasing trend in the average orientation, similar to the nematic order. System with higher energy anisotropy also exhibits a wider distribution in particle angle with lower peaks comparing to system with low energy anisotropy (Figure 3.17 in Appendix 3-A).

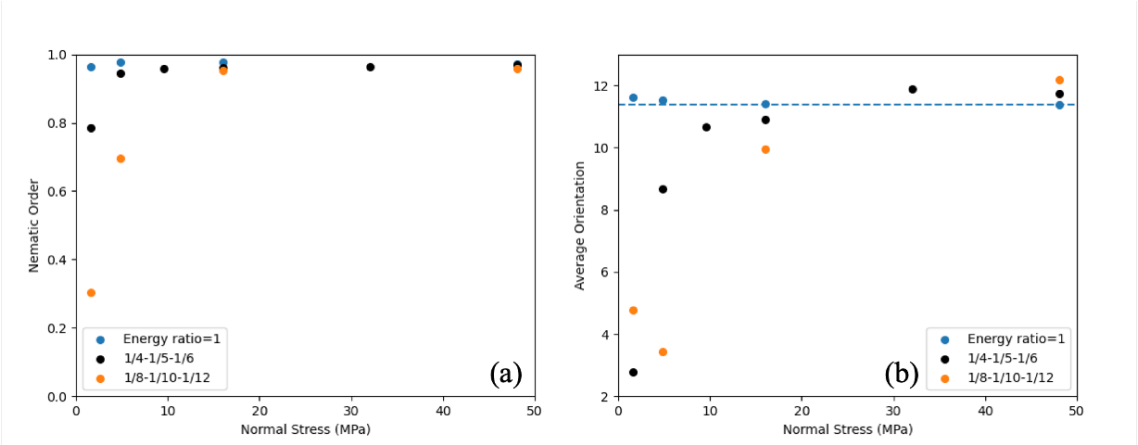

Figure 3.11: (a) the nematic order and (b) the average orientation as a function of normal

stress for different energy ratio.

Figure 3.12 shows the characteristic stacking size as a function of normal stress determined from PaRDF for different energy ratios. The stacking size generally increase with energy anisotropy. The stacking sizes in systems with default energy ratio of 1/4-1/5-1/6 first increase and then decrease with normal stress and the peak is reached near 10 MPa. The similar trend also occurs for the other two normal stress, The position of the highest stacking size shifts slightly to higher normal stresses with increasing energy anisotropy.

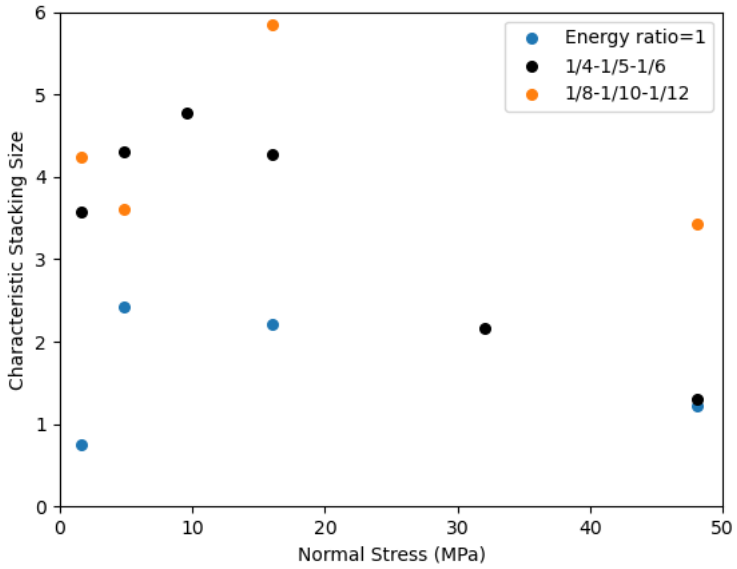

Figure 3.12: The characteristic stacking size as a function of normal stress for different energy ratio.

3.4 Discussion

3.4.1 Relationships between shear response and structural change

3.4.1.1 Connection between volume fraction and structure change

To explore the relationships between shear response and structural changes, we examine case with large fluctuations in nematic order at the lowest normal stress (1.60 MPa). Figure 3.13(a) shows the evolution of shear stress, volume fraction, nematic order, and average orientation during shear. Vertical lines indicate the local minima in nematic order. The position of these local minima in nematic order are close to the local minima in volume fraction and local maxima in average orientation. This correlation suggests that a decrease in volume fraction is

associated with a decrease in nematic order and an increase in average orientation. At 1.60 MPa, the significant decrease in nematic order is caused by rotation of clusters. However, with the drastic decrease and increase in structural change lasts for several strains, the fluctuations in shear stress are relatively small. Thus, no direct connection is observed between transient change in shear stress and change in structural parameters.

A similar comparison is made at higher normal stress 16.03 MPa (Figure 3.13(b)). At the higher normal stress, the correlations between nematic order, volume fraction, and average orientation are less obvious.

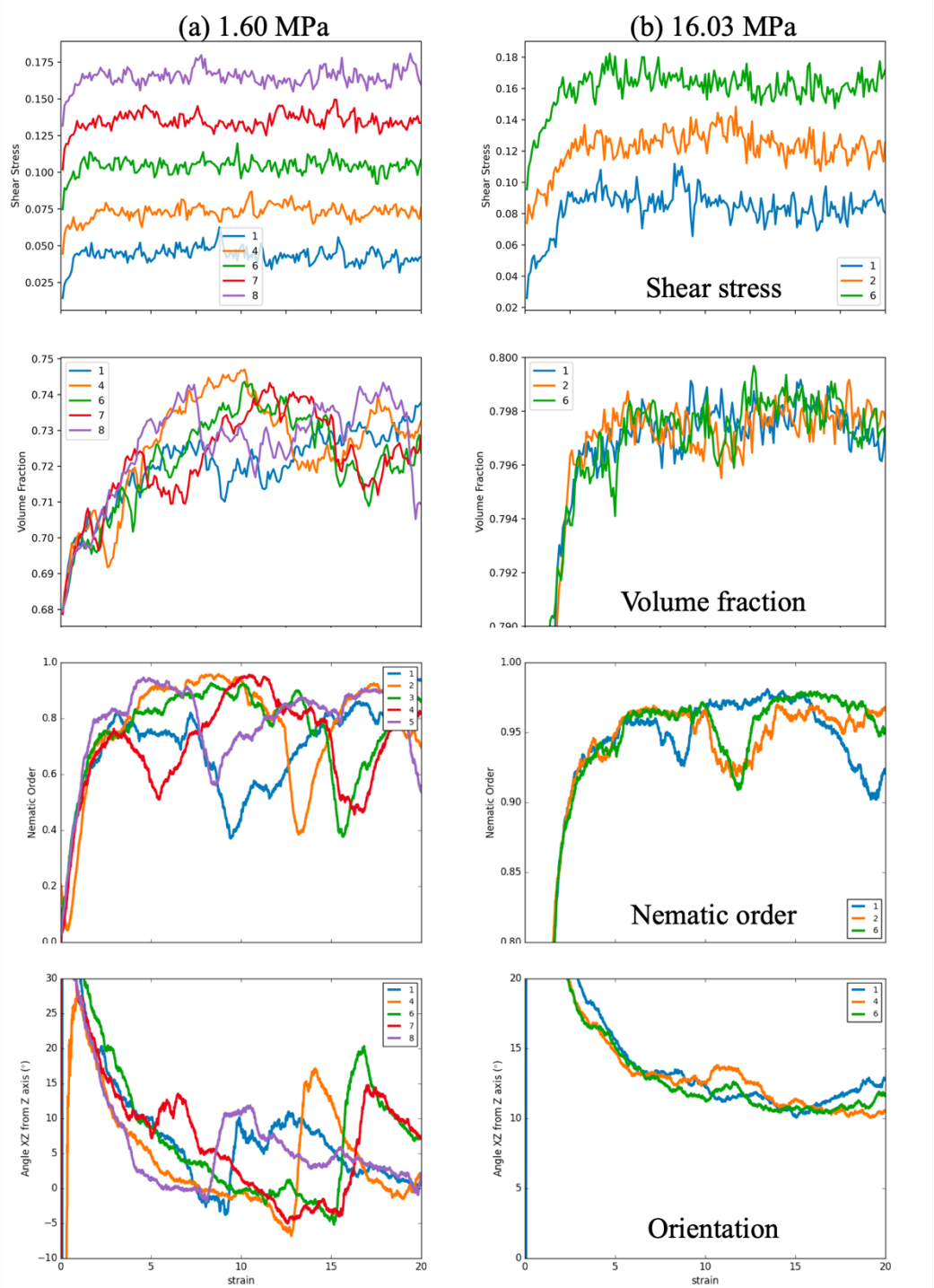

Figure 3.13: Comparison between the shear stress, volume fraction, nematic order and average particle orientation during shear at different normal stress. Only cases with large fluctuations are picked out (case 1, 4, 6, 7, and 8 at 1.60 MPa and case 1, 2, and 6 at 16.03 MPa). Vertical dotted lines mark the position of local minimums in nematic order developments.

3.4.1.2 Connection between shear stress and volume fraction

Transient shear stress as a function of volume fraction during the shear strain of 20 is shown in Figure 3.14(a). the Initial stage of shear represented by the tail starting from lower left, showing an increase in both shear stress and volume fraction. After large strains, both the shear stress and volume fraction concentrate in a region at the upper right corner of the graph. For further analysis, the data points from strain 10 to 20 averaged over every 10^4 steps are shown in Figure 3.14(b). Decrease in shear stress with increase in volume fraction is observed at high normal stress cases. However, the trend is not evident at the lowest normal stress of 1.60 MPa.

The shear stresses are then divided into three groups based the volume fractions, and the probability distribution of shear stress for each group is shown in Figure 3.14(c). At the lowest normal stress, shear stress at different volume fraction shows similar distributions. In contrast, at high normal stress, the distribution shifts to larger shear stress for lower volume fraction group.

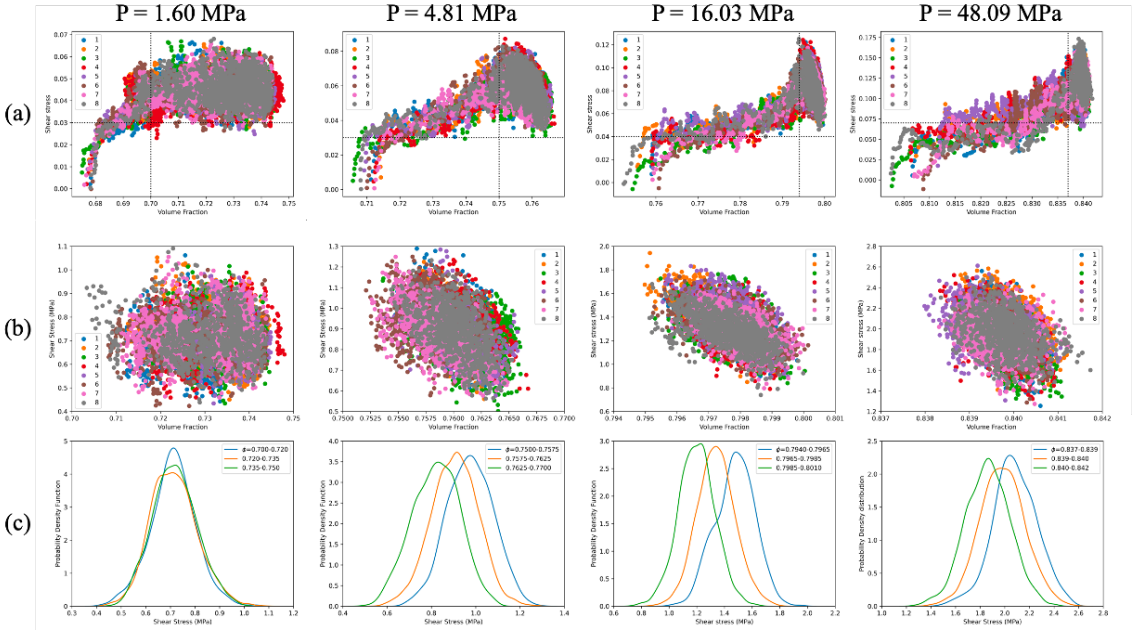

Figure 3.14: (a) The relation between shear stress and volume fraction for 20 strains at different normal stress. The value is averaged every 1e4 step for eight samples marked in different colors. Dotted lines separate the range of stress and volume fraction for strain 10 to 20 on the upper right region. (b) The relation between shear stress and volume fraction from strain 10 to 20 at different normal stress. (c) The probability density distribution of shear stress is shown with all data points divided into three groups based on the corresponding volume fraction.

3.4.1.3 Shear process at different normal stress

At the normal stress of 1.60 MPa, shear stress initially increases and reaches near a steady-state value within the first two strains. However, volume fractions ad nematic order continues to fluctuate throughout the shear process. Visual inspection indicates that the shear process at low normal stress is largely controlled by the collective movement of particle clusters (Figure 3.1).

When temporary clusters form and rotate during shear, the system dilates and nematic order decreases. Conversely, when these temporary cluster disintegrate, the nematic order is restored, and the system become more compact. Despite significant change in nematic order and volume fraction, the connection between the overall shear stress with structure change remains unclear (Figure 3.13, Figure 3.14).

At High normal stress, the system is more compact with diminished collective cluster movement. In this scenario, small dilation within the system may be associated with particle misalignment and temporary shear localizations. Transient shear stress at high normal stress clearly increases with system dilations (Figure 3.14).

The shear process at high normal stress in 2D cases is similar to the process described in 3D cases. Initially, shear stress increase to a peak value near 400% strain, accompanied by significant increase in both volume fraction and nematic order. In the subsequent stage, shear stress decrease to a residual value with relatively small structure changes. However, shear bands are not clearly observed in the 2D system, this will be further discussed in Section 3.4.3.3.

3.4.2 Effect of normal stress in a 2D system

The differences between system at high and low normal stress can be observed from several aspects with a separation point near P=10 MPa. There is a stepwise change in residual shear stress with increasing normal stress (Figure 3.3(b)). The slope is larger for normal stress lower than 10 MPa. Structure analysis shows that the preferred orientation increases from 0 to about 11.5° for normal stress smaller than 10 MPa, and do not significantly change at higher normal stress (Figure 3.5). A similar turning point can also be observed for stacking size (Figure 3.7).

Visual inspection and transient fluctuation in volume fraction and nematic order confirm a cluster-dominated phase at low normal stress. Particles maintain a stacking structure within clusters and exhibit collective rotational or translational movements. The system at higher normal stress is characterized with higher volume fraction, higher nematic order, and reduced stacking size.

These structure changes align with experimental observations of dry montmorillonites

(Saffer and Marone, 2003). The contact area between particles increases with normal stress. At high enough normal stress, complete contact area between particles can be reached in highly aligned clay platelets. The description on the structure evolution and decrease in friction with increasing normal stress is consistent with our simulation result. B, value saturation. Similar phenomena are observed in shear experiment of pelagic clay (Ueda et al., 2024). At high effective normal stress, clear P and Y shear fabric can develop with clay minerals orient parallel to the shear surface. Conversely, random fabrics were developed during shear at low effective normal stress, which is generally consistent with the cluster movement in the current study.

3.4.3 Comparison with 3D results

The shear configuration changed from three dimensions to two dimensions and particle shape changed from disc-like oblate ellipsoids to ellipses. The aspect ratios were adjusted from 1/5, 1/6, and 7 in 3D to 1/4, 1/5, and 1/6 in 2D. In 2D simulations, the energy ratio increased with the aspect ratio, whereas a consistent energy ratio of 1/5 is used for in 3D.

3.4.3.1 Shear resistance

The friction coefficient determined from yield stress was 0.0135 for previous 3D simulation. In 2D the friction coefficient shows a stepwise change from 0.126 at low normal stress to 0.0188 at high normal stress. The higher normal stress value in 2D approximates the 3D results, while the low normal stress value aligns with the friction coefficient of Na-Montmorillonite of 0.15 from shear experiment for normal stress smaller than 100 MPa (Behsen and Faulkner, 2013). Morrow et al. (2017) reported that the friction coefficient of wet Montmorillonite increases with effective normal stress, which contrasts with the result of the present study. The HB model was employed to describe the shear stress as a function of strain rate with velocity-strengthening behavior in both systems. In 3D, the exponent n displayed a declining trend with increasing normal stress, ranging from 0.5 to 0.2. Conversely, in 2D, the exponent n first increase from 0.05 to 0.45 with normal stress and then decrease at normal stress above 32.06 MPa.

3.4.3.2 Structure

Figure 3.15 shows the nematic order and characteristic stacking size as a function of normal stress at the lowest strain rates: 1.68×10^{6} /s in 2D and 6.93×10^{5} /s in 3D. Previous 3D system shows a higher nematic order that slightly decreases with normal stress, while the 2D system exhibits smaller nematic order for normal stresses below 10 MPa. The PaRDF reveals the 2D cases have a more pronounced stacking structure comparing to the 3D system. The

characteristic stacking size first increase and then decrease with normal stress. In 3D, however, the stacking size generally decrease with increasing normal stress.

When comparing the shear resistance and structural properties, the results from 3D simulation align more closely with the higher normal stress conditions in 2D. In both scenarios, the systems are characterized by high nematic order and weak parallel stacking. The low normal stress phase in the 2D system, dominated by cluster movement, is not observed in the 3D system within the same range of normal stress range.

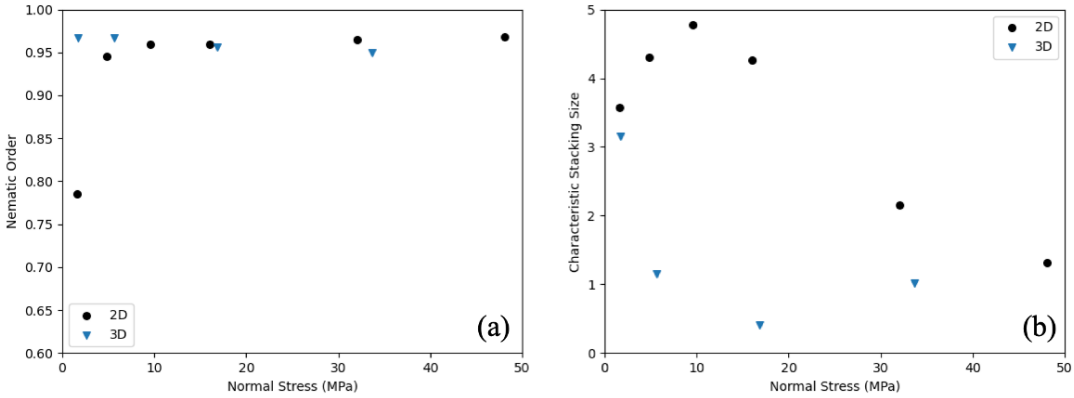

Figure 3.15: The nematic order and the characteristic stacking size at a function of normal stress for 2D and 3D system.

3.4.3.3 Shear localization

In Chapter 2, we demonstrated that shear localization occurs at low strain rates in 3D simulations. However, a clear shear band is not observed in the 2D system under similar strain rate and normal stress conditions. To further analyze this, we conducted additional shear tests in 2D at a lower strain rate of 1.68×10^{5} /s. Due to long computation time, only two samples with different initial structure are tested.

Figure 3.16 shows the velocity and orientation profiles at the normal stress of 16.03 MPa for different strain rates in Case 2. The velocity profiles are averaged over one strain. At high strain rate, the velocity profile is nearly linear, and the particle orientation is homogeneous and close to the preferred orientation of about 10°, which is consistent with 3D results. As the strain rate decreases, fluctuations can be observed in both the velocity and orientation profiles. The extend of fluctuation increases at lower strain rate, preventing the clear identification of stable fast and slow shear zone. Long-lived fluctuations in the velocity profile suggest the possibility of having multiple positions of shear localization along the Z direction, this is not observed in the 3D case. The position of shear bands can be identified from accumulative distance and may depend on initial structure (see Figure 3.18 in Appendix 3-B). Due to large

fluctuation, it is challenging to associate the velocity profile with particle orientation. However, for the new strain rate at 1.68×10^{5} /s, a stable shear band can be overserved. The position of localized shear and preferred orientation matches, aligning with the 3D system.

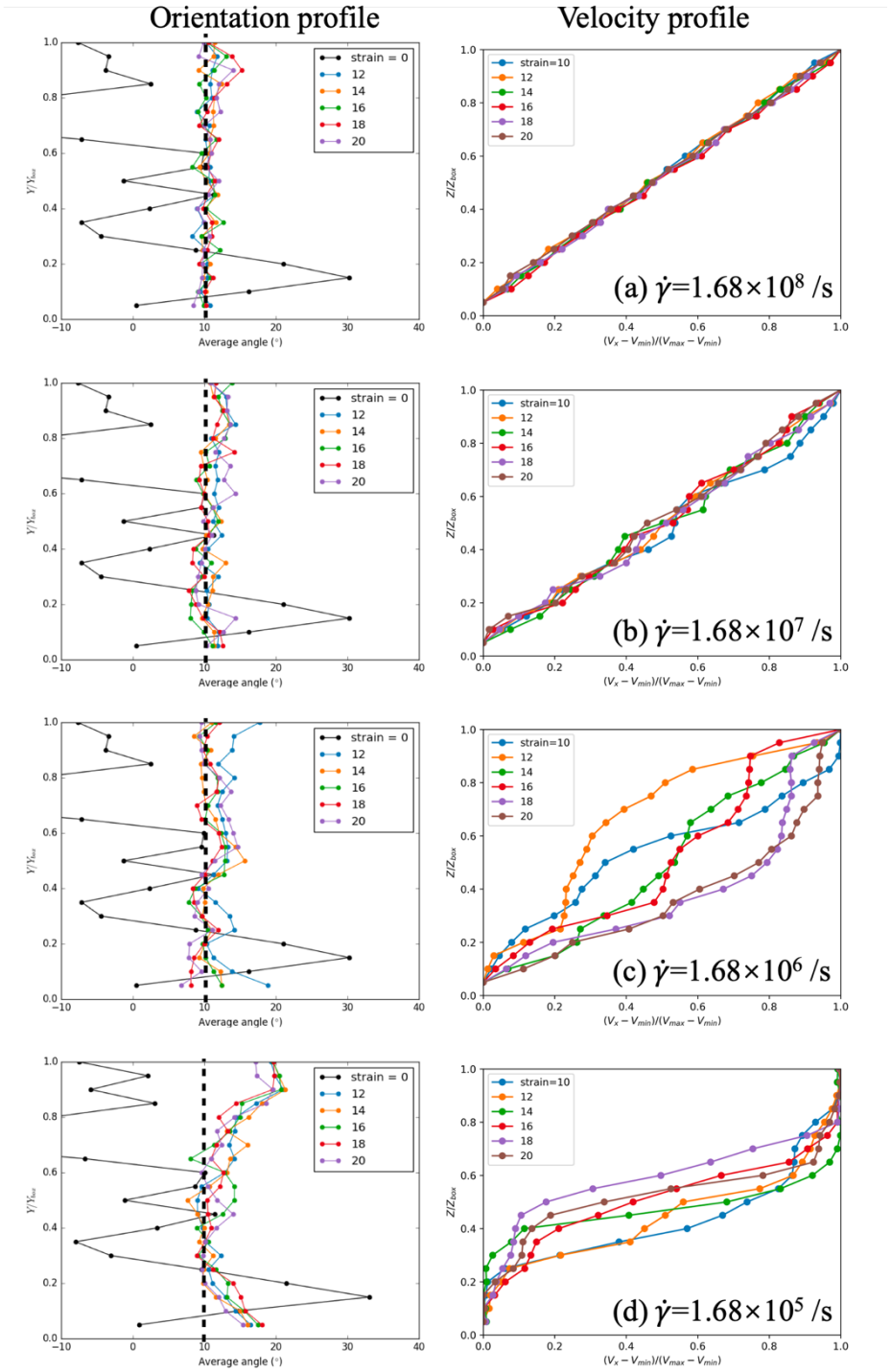

Figure 3.16: Example of orientation profile and velocity profile for strain 10, 12, 14, 16, 18, 20 at the normal stress of 16.03 MPa. The corresponding strain rate is (a) 1.68×10^{8}, (b)

1.68×10^{7}, (c) 1.68×10^{6} and (d) 1.68×10^{5} /s. The velocity profiles are averaged over one strain.

In the 3D system presented in Chapter 2, shear localization can be observed at a higher strain rate ~1×10^{7} /s at the normal stress of 16.85 MPa. The position of the shear band is also relatively stable across a wide range of strain rates. In contrast, a stable shear band in 2D is only observed at the strain rate ~1×10^{5} /s for the normal stress of 16.03 MPa, which is about 100 times slower than in 3D. The fluctuations in velocity profile are reminiscent of long-lived flow inhomogeneities observed in simple yield stress fluid experiments and in a simulation of jammed system with attraction (Divoux et al., 2010; Chaudhuri et al., 2012). Chaudhuri et al. (2012) suggests that these long-lived fluctuations indicate unstable velocity profile due to the proximity to the yield stress regime.

Furthermore, we found the formation of shear localization in 2D depends on the initial structure (see Figure 3.19 and Figure 3.20 in Appendix 3-C). At the strain rate of 1.68×10^{5} /s the velocity profile exhibits only large fluctuation without a stable shear band in Case 1 while stable shear bands are found in Case 2. In these scenarios, the slow shear (or not sheared) region is always associated with a region where the particle orientations show clear deviation from the preferred value. This may suggest the formation of shear band is difficult when the particle orientation is already homogeneous (16.03 MPa and 48.09 MPa in Figure 3.19(c, d)) and possible transient shear localization can occur at multiple position along the height, resulting in fluctuation in velocity profile.

3.4.4 Effect of energy ratio comparing to illite in experiments

Larger energy anisotropy results in a deeper potential well in face-to-face configuration, leading to higher shear stress. Systems with larger energy anisotropy are less aligned and exhibit a wider particle orientational distribution compared to those with smaller energy ratio. However, at high enough normal stress, system with different energy ratios achieve a similar orientation around 11.4°.

Higher energy anisotropy can be linked to larger surface charge densities in clay minerals. The current result on shear stress is consistent with the experimental observation where illite, with a larger surface charge density, shows a greater friction comparing to montmorillonite (Tembe et al., 2010; Ashman and Faulkner, 2023). However, the XTG results from Haines et al. (2013) indicate the crushed illite have a slightly higher fabric intensity than montmorillonite which contradicts our results on nematic order.

Direct comparison between fabric intensity and nematic order is challenging because the scale of our investigated system may be too small comparing to the gouge in experiments. The

macroscopic sample involves the development of shear fabrics with intact aggerate, which our nanometer scale system cannot capture. Haines et al. (2009) shows the fabric intensity increase with depth for different compositions. At shallow depth, the fabric intensity is dominated by compaction and remains low (1~4). At greater depth, below the smectite-illite transformation zone, fabric intensity can exceed 20 for shale and slate. The large increase is mainly controlled by new minerals formed in a preferred orientation in response to differential stress during the diagenetic processes.

In our simulation, nematic order reached over 0.8 even at low normal stress, but the fabric intensities of smectite and illite from experiments remain low. Previous clay simulations suggest the nematic order will decrease at larger system size in compaction (Asadi et al., 2022; Bandera et al., 2021). Additionally, the experiment used dry and crushed clay samples while the simulation assumed saturated condition, the behavior and the structure can be different due to the presence of water.

Zhu et al. (2022) fitted the Gay-Berne potential with the potential of mean force for both illite and smectite using full atomistic MD. They found the energy anisotropy for illite is about 3 times larger than for smectite. However, the GB potential cannot fully describe the width of the potential or the repulsion at small separations for illite. A critical concern is that illite layers can be bonded together by K^+ cations, preventing water molecules from getting into the interlayer space (Carroll and Starkey, 1958). Consequently, the structured water interlayer cannot be formed in illite and K+ cations cannot move freely. Illite platelets are bonded strictly parallel at a shorter separation, which may contribute to the higher fabric intensity for illite from experiment. Additional bonding mechanism may be necessary to accurately describe illite interactions.

3.5 Conclusion

We performed constant strain rate shear simulations in a 2D model clay system, focusing on the effect of normal stress and energy anisotropy. The system exhibited velocity-strengthening across all cases, with varying structure development under different normal stresses. At low normal stress, shear is primarily governed by movement of particle clusters, leading to system dilation and decreased nematic order. In contrast, at higher normal stress, particles are more aligned, and the cluster structure and parallel stacking are diminished. The most probable particle orientation shifts from 0 to a positive angle near 11°. We found that higher shear stress occurs at lower volume fractions, which may be associated with misalignment and temporary shear localization within the system.

The behavior of the 2D system at high normal stress is in good agreement with the previous 3D result in small apparent friction, a decreasing exponent in the HB model with increasing

normal stress, and structural characteristics of high nematic order and low parallel stacking size. However, the low normal stress phase, characterized by cluster movement, is not identified in previous 3D system. Both 2D and 3D system show shear localization at sufficiently low strain rates and homogeneous shear at high strain rates. In the 2D system, the stable shear band are observed at much lower strains rate compared to the 3D system. At intermediate strain rate, the 2D system is characterized by long-lived fluctuation in velocity profile.

Higher energy anisotropy results in higher shear resistance and lower particle alignment. At low normal stress, the nematic order decreases with increasing energy anisotropy, and the most probable angle is closer to zero. All systems achieve the preferred orientation near 11° at sufficiently high normal stress.

The results indicate that simply using a higher energy anisotropy cannot fully represent the behavior of illite minerals comparing to smectite. More study on particle interaction is needed to extend the model of smectite to other phyllosilicate minerals.

Appendix 3-A The effect of energy ratio on particle angle distribution

System with higher energy anisotropy have a wider distribution in particle angle comparing to system with low energy anisotropy at low normal stress (Figure 3.17). The peak is slightly lower for high energy anisotropy.

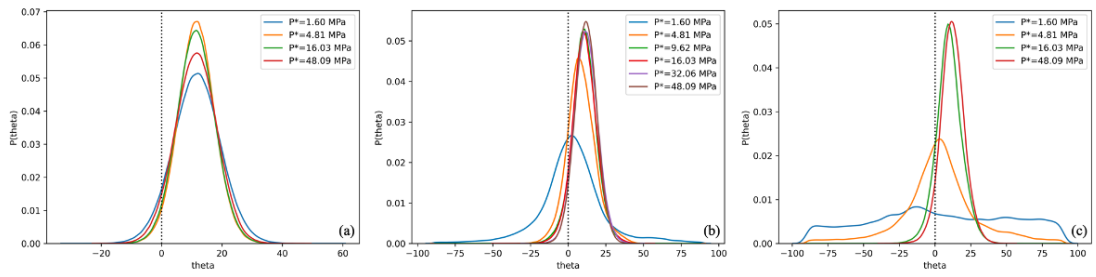

Figure 3.17: Probability density distribution for a particle to be oriented at angle theta for different normal stress with energy ratio (a) 1, (b) 1/4-1/5-1/6, (c) 1/8-1/10-1/12.

Appendix 3-B Accumulative distance profile

Figure 3.18 compares the velocity profile averaged over 1 strain and accumulative distance profile for three cases at a normal stress of 4.81 MPa and a strain rate of 1.68×10^{6} /s. The accumulative distance profile is derived from velocity profiles at different strains. Averaging over longer strains generally reduces larger fluctuations, though all accumulative distance profiles at strain of 20 deviate from a linearity. In case 1 and 8, the accumulative distance

profiles reveal two fast shear regions, corresponding to the relatively stable positions of the shear bands observed in the velocity profile. In contrast, case 3 exhibits a smoother accumulative distance profile without distinct fast and slow shear region. The result suggests the 2D system can display more than one shear band. The stability of shear band positions after long strains may depend on the initial structure over the investigated period. Shifting transient shear band (fluctuations) can disappear when averaged over a longer time window. The difference between the 2D and 3D system may result from the system size, as the height in the 3D system is about 75 nm, while the height in the 2D system is about 165 nm. Considering the 3D system exhibits one shear band with periodic boundary conditions, it may display multiple shear bands at larger system size.

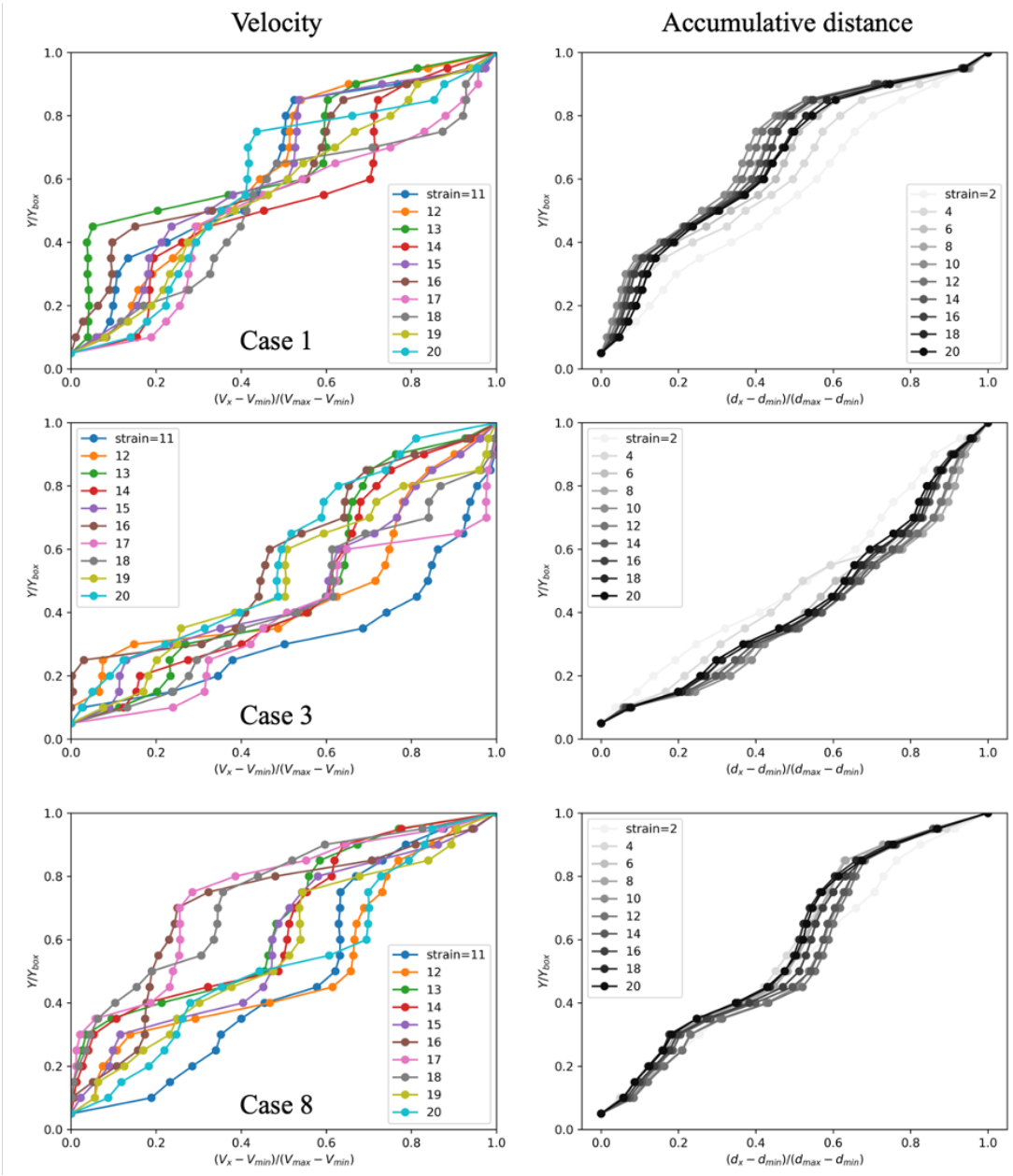

Figure 3.18: Example of velocity profile and accumulative distance profile at the normal stress of 4.81 MPa and strain rate of 1.68×10^{6} /s for Case 1, 3, and 8. The velocity profiles are averaged over one strains.

Appendix 3-C Velocity profile and orientation profile at strain rate of 1.68×10^{5} /s

The shear localization depends on the structure in each case. In Case 1, the shear band is only clear at 4.81 MPa where there is obvious deviation from preferred orientation (Figure 3.19(b)), but only large fluctuation at higher normal stress when the orientation is all near the preferred orientation (Figure 3.19(c, d)). Velocity profiles show clear sheared zone and

unsheared zone in Case 2 (Figure 3.20).

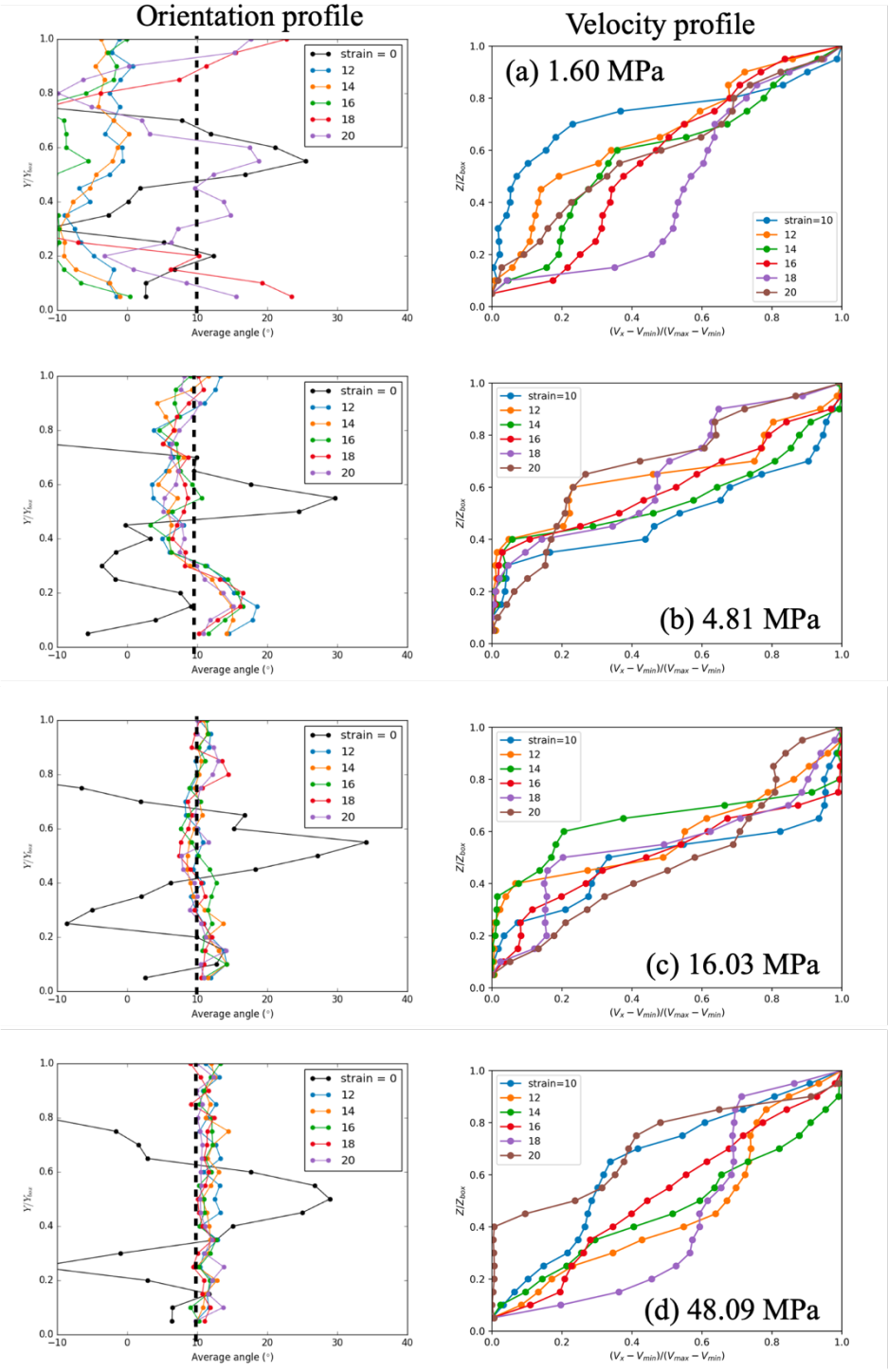

Figure 3.19: Orientation profile and velocity profile for strain 10, 12, 14, 16, 18, 20 at the strain rate of 1.68×10^{5} /s for Case 1. The corresponding normal stress is (a) 1.60, (b) 4.81, (c) 16.03, and (d) 48.09 MPa.

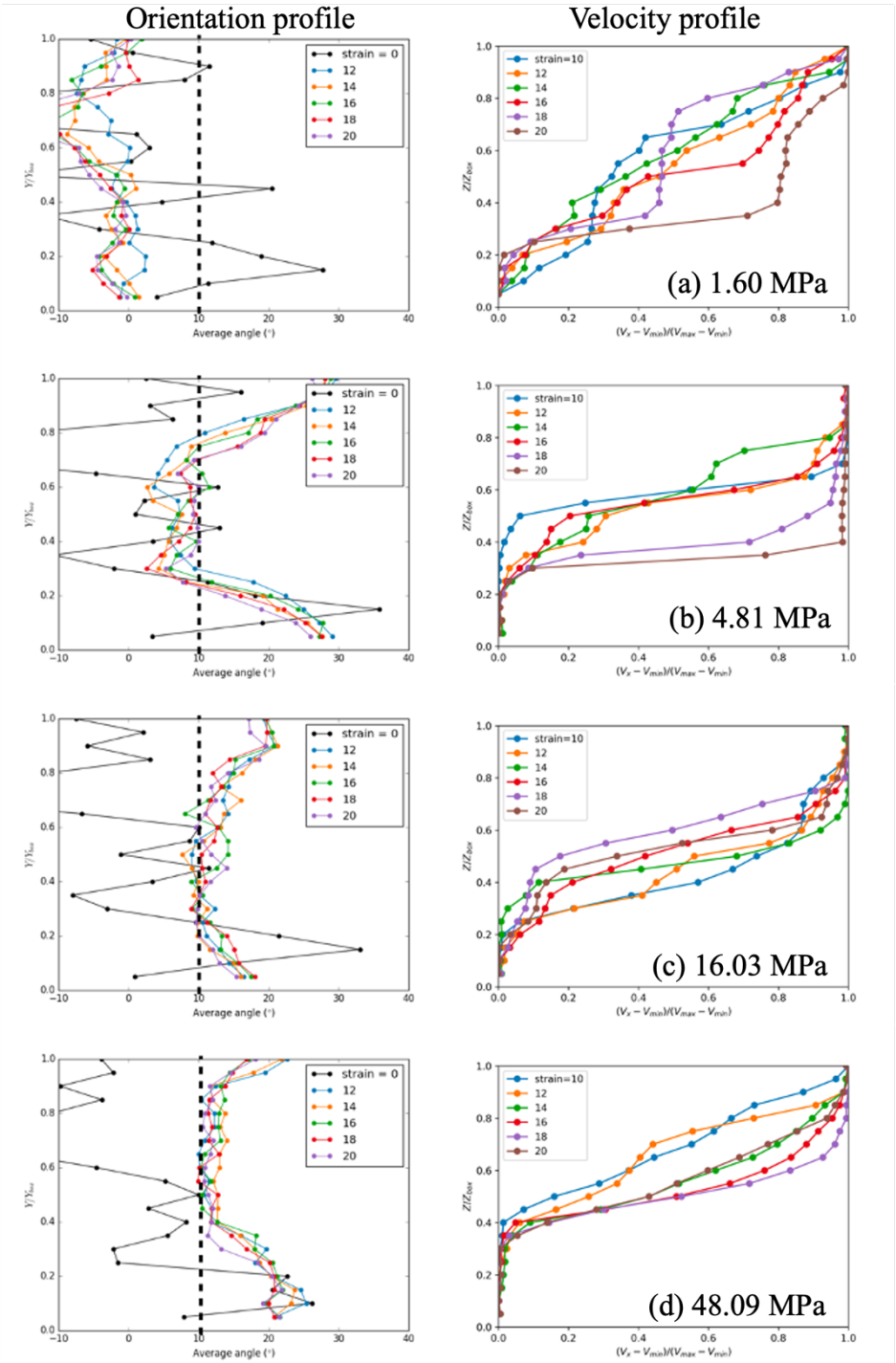

Figure 3.20: Orientation profile and velocity profile for strain 10, 12, 14, 16, 18, 20 at the strain rate of 1.68×10^{5} /s for Case 2. The corresponding normal stress is (a) 1.60, (b) 4.81, (c) 16.03, and (d) 48.09 MPa.

4 Shear instability in a confined 2D system

4.1 Introduction

4.1.1 Shortcoming of previous chapters

In the previous chapters, the steady-state rheology was studied using constant strain rate in bulk shear. Periodic boundaries were used to avoid the effect of system walls. However, in the natural fault zones, shear is driven by the relative motion of the plate walls. Consequently, shear in the confined system with moving plates should be considered for a more realistic representation. The studied system exhibited yield stress fluid behavior, where the system can flow beyond a critical stress. Numerical studies have shown this behavior may govern possible earthquake generation in clay-rich fault (Kameda and Hamada, 2022). While unstable flow phenomena such as shear banding and fluctuations in velocity profiles have been observed in previous chapters, it is important to examine whether our system can exhibit instability under boundary-driven shear configurations.

4.1.2 The objective of this chapter

In this chapter, we focus on examining the rheology and stability in a confined system with a moving upper plate. We test two shear configurations: first, by applying a constant force to pull the upper plate; second, by pulling a spring attached to the upper plate at a constant velocity. The setup of the model is presented in Section 4.2. In Section 4.3, we present the results on yield stress measurement and stick-slip behavior. In Section 4.4, we discuss the results obtained and possible theoretical explanations. In Section 4.5, we summarize our findings.

4.2 Method

4.2.1 Preparation of a confined system

The three types of ellipsoid particles and Gay-Berne potential with aspect ratio 1/4-1/5-1/6 and energy ratio 1/8-1/10-1/12 is used to represent clay platelets inside the gouge. A new type of plate particle is used to build the upper and lower plate with diameter of $5\sigma_0$. The energy scale for plate particles is set to $\epsilon_{wall} = 5\epsilon_0$ with energy ratio of 1, providing a uniform strong attraction between the wall and clay platelets. Interaction between plate particles is neglected. The parameters used in the 2D confined system are shown in Table 4-1. Translational and rotational equations of motion are integrated using the velocity Verlet algorithm with a dimensionless time step $\delta t = 0.01$ if not specified. To optimize the

computational time, the interaction potentials are truncated at a cutoff of $7\sigma_0$.

Parameters	Value
Length scale $\boldsymbol{\sigma_0}$ (nm)	1.55
Clay thickness $\boldsymbol{\sigma_{ff}}$ (nm)	1.55
Clay diameter $\boldsymbol{\sigma_{ee}}$ (nm)	6.2, 7.75, 9.3
Plate particle diameter $\boldsymbol{\sigma_{wall}}$ (nm)	7.75
Aspect ratio $\boldsymbol{\kappa}$	1/4, 1/5, 1/6
Energy scale $\boldsymbol{\epsilon_0}$ (eV)	0.3726
Clay energy ratio $\boldsymbol{\kappa'}$	1/8, 1/10, 1/12
Plate particle energy ratio $\boldsymbol{\kappa_{wall}'}$	1

Table 4-1 Gay-Berne potential parameters in 2D confined system

The system is periodic in X direction and non-periodic in Y direction. The plate particles are generated on a 2D square lattice with number density of 0.1, where particles overlap. Surface roughness is made by moving certain columns of plate particles 1 lattice unit inward. The strong interaction and roughness on the plates aim to prevent wall slip and promote adjacent gouge particles to move together with the plate. Clay Particles are generated on the square lattice with a number density of 0.02. The system consists of 420 plate particles (210 each for upper and lower plate) and 1236 clay particles with a similar population for all three types.

The position of the lower plate particles is fixed throughout the simulation. The upper plate is treated as a rigid aggregate, with the total force experienced by the upper plate particles are averaged over the entire plate. The system is compressed by applying a constant dimensionless force F= 1 in Y direction on each particle, which provides an equivalent normal stress of 35.48 MPa. The system is first compressed and equilibrium for a period of t = 3000 and then sheared for more than 10 strain with upper plate moving at a constant velocity 0.007. The resulting configuration is used in the following shear tests.

4.2.2 Shear tests by pulling the upper plate

We perform two types of shear tests by applying force load on the upper plate, with and without a spring.

In the constant force pulling test, we apply a constant force in the X direction on the upper plate and monitor the sliding velocity of the upper plate (Figure 4.1(a)). Each stage lasts for $t = 2\times10^4$ (2×10^6 MD step). The average pulling force applied on each plate particle is ramped from 0.08 to 0.13 and back to 0.08 with an interval of 0.01. Cases with average force 0.105, 0.11 and 0.115 are later monitored for longer period of $t = 2\times10^5$. Higher average pulling force

in the range of 0.15 to 0.3 is also tested with an interval of 0.05.

In the second part, we attach one end of a spring to the upper plate and then pull the other end of the spring at constant velocity of 0.01 for t = 4×10^5 (Figure 4.1(b)). The spring constant k of 100, 1, and 0.1 is used. This configuration simulates the stress accumulation on the plate at a constant rate. The total force experienced by the top plate and the sliding velocity is monitored.

For further analysis of the stick-slip motion, longer shear is performed with time step δt = 0.005 for t= 1×10^6 with spring constant k=0.1 at F=0.1, 0.5, 1, and 5 (normal stress 3.55 MPa, 17.74 MPa, 35.48 MPa, 177.42 MPa) and for t= 2×10^6 with spring constant k=0.01 at F=1 (35.48 MPa).

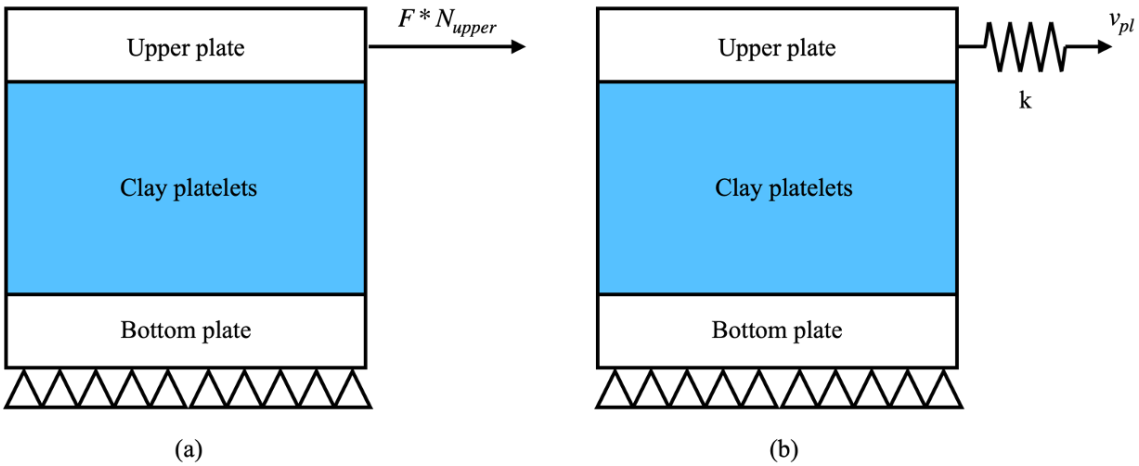

Figure 4.1: Schematic figure for two shear configurations. (a) A constant pulling force is applied in the X direction on the upper plate, the average force F is applied on N_{upper}=210 particles. (b) Force is applied by pulling a spring with spring constant k at constant speed v_{pl}=0.01.

4.3. Result

4.3.1 Initial shear

The shear configuration after initial shear is shown in Figure 4.2(a). The nematic order for the center region 10 unit away from the plate have reached above 0.9 after shear (Figure 4.2 (b)). The average particle angle is in the range 10~12 degrees, which is consistent with the preferred orientation obtained from Chapter 3 (Figure 4.2(c)). The size of the confined system is 94.8683 in X dimension and the Y dimension is about 110 after compression.

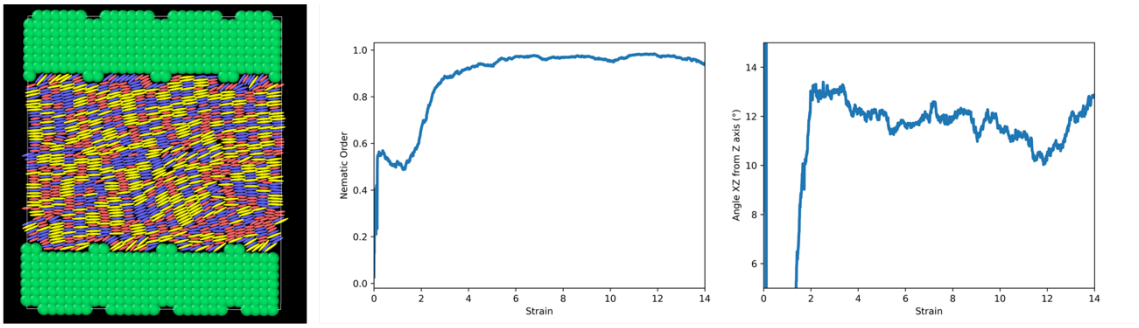

(a) (b) (c)

Figure 4.2: Confined system after initial shear. (a) system configuration, wall particles and platelets with three aspect ratios are in different colors. (b) The nematic order and (c) the average particle orientation of the center part of the system during shear.

4.3.2 Constant force

The change in plate velocity as a function of time is shown in Figure 4.3. The velocity is time averaged every 100t. The plate velocity is fluctuating near 0 and cannot slide for average forces smaller than 0.1. When a larger force is applied, the plate velocity fluctuates in a positive range. At the largest average force 0.13, the plate velocity is clearly positive but distributed over a wide range from 0 to 0.2.

Slightly different behavior between ramping up and ramping down can be observed showing signs of hysteresis. The plate velocity fluctuates in a more positive range at average force 0.1 and 0.11 when ramping down. Conversely, the fluctuation at an average force of 0.12 is reduced during ramping down. The overall trend indicates that a yield force exists in the range 0.1~0.12, below which the system cannot flow.

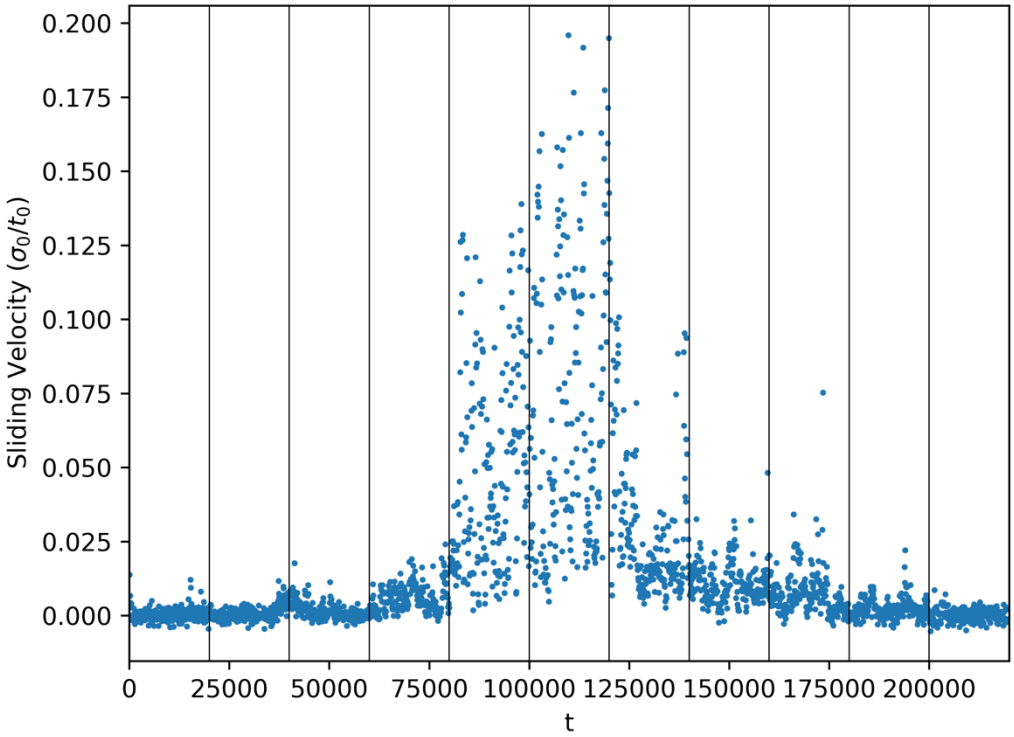

Figure 4.3: Sliding velocity vs. time with average pulling force ramping up from 0.08 to 0.13 and then ramping back to 0.08 with an interval of 0.01. The solid line denotes the duration of each stage for $t = 2\times10^4$.

The velocity distribution at each pulling force is shown in Figure 4.4. A near symmetric peak with the most probable velocity near 0 can be found for average force 0.08 and 0.09. A slight positive peak can be found for average force 0.1 and 0.11 but with scattered values at higher values. At higher average force, the velocity distribution shows a positive peak with a long tail on the positive side.

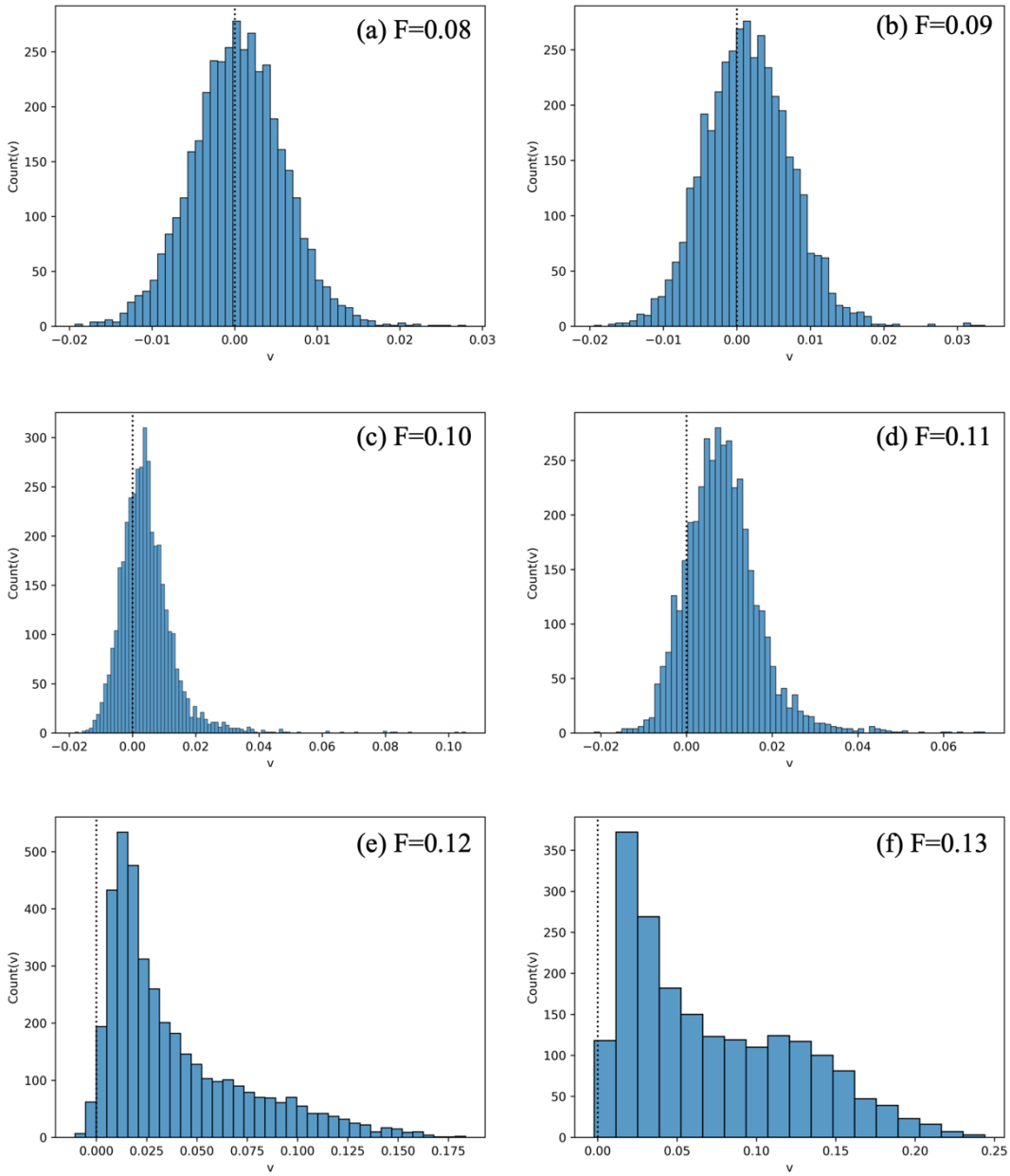

Figure 4.4: sliding velocity distribution of the upper plate at average pulling force (a) 0.08, (b) 0.09, (c) 0.10, (d) 0.11, (e) 0.12, and (f) 0.13.

To measure the yield force of the system, we applied average force 0.105, 0.11 and 0.115 to the upper plate and extend the duration to a long period of $t = 2\times10^5$ to reduce the effect of hysteresis during force ramping. The plate velocity as a function of time and the velocity distribution for different applied forces in shown in Figure 4.5. The velocity is time averaged every 100t. Only velocity in the latter half of the shear is considered in the velocity distribution. The system at average force 0.105 generally cannot flow but experienced one velocity increase

near t=1.25×10^5, then returned to fluctuations near 0. The corresponding velocity profile shows a clear peak near 0 with a few higher value points. When larger average force 0.11 and 0.115 is applied, the system initially showed a velocity near 0 but then become unstable after longer waiting time. At force 0.11, the velocity peak is still close to zero and a long positive tail start to appear. At force 0.115, the peak is clearly positive with no negative values, and the distribution is more continuous.

We define the static yield force as the smallest force applied on the upper plate that initiates system sliding. From the observed velocity evolutions and distributions, the upper plate starts to slide (albeit in an unstable manner) when the average force applied is above a yield value in between 0.105 and 0.11. Given the number of particles in the upper plate (N_{upper}=210), the static yield force is between 22.05~23.1.

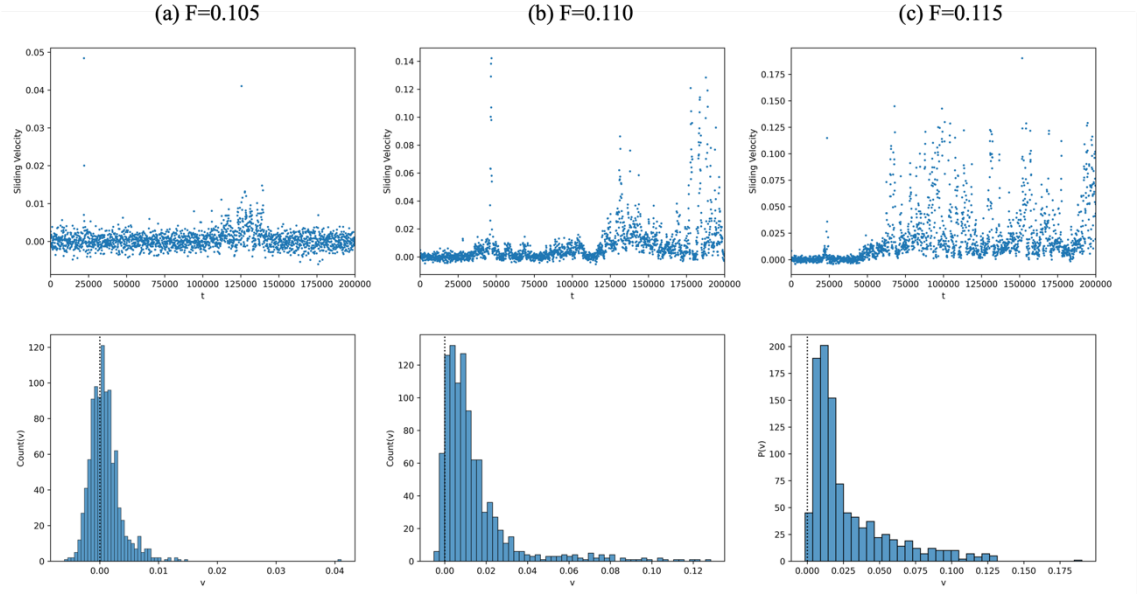

Figure 4.5: Sliding velocity of the upper plate vs. time (top row) and velocity distribution on the second half of the shear (bottom row) for average pulling force (a) 0.105, (b) 0.110 and (c) 0.115. The velocity is time averaged every 100t.

Configurations at higher applied force is further tested by ramping in the range of 0.15 to 0.3. The plate velocity as a function of time is shown in Figure 4.6(a). The velocity is time averaged every 100t. The sliding velocity is generally stable in each stage and increases with the applied force. The velocity distribution at high pulling forces shows a single positive peak without a long tail on either side (Figure 4.6(b)). Only the initiation stage experienced a suddenly drop in velocity at the lowest applied force of 0.15. No clear hysteresis is observed during ramping up and down. The force as a function of the sliding velocity can be characterized using the following equation in a form similar to the Herschel-Bulkley model:

$$F = F_0 + K * v^n \tag{4.1}$$

where F_0 is the yield force, K and n are constants. Using data from the high velocity and high pulling force end, we estimated a dynamic yield force at zero strain rate (Figure 4.6(c)). The fitting gives a relationship of $F = 18.698 + 47.559 * v^{0.715}$. The yield force obtained from this dynamic model (18.698) is slightly lower than the static yield force (22.05~23.1) obtained from constant force pulling.

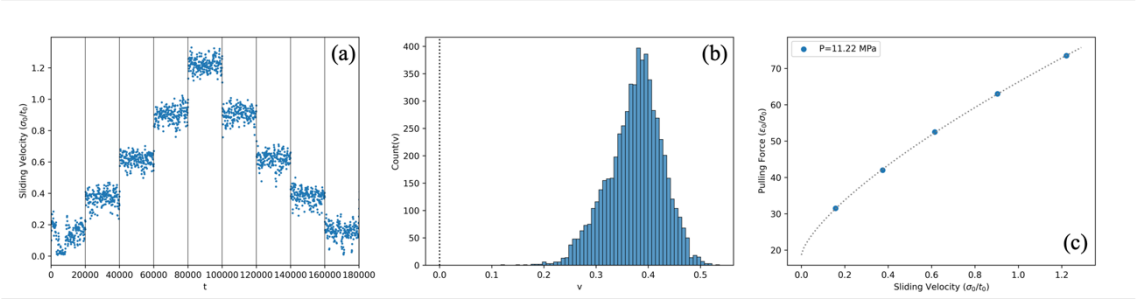

Figure 4.6: Force ramping up and down in the range of 0.15~0.30. (a) Sliding velocity of the upper plate vs. time. (b) Velocity distribution at average pulling force 0.20. (c) Force-velocity relationship fitting following Equation (4.1).

4.3.3 Pulling with a spring

4.3.3.1 Effect of spring constant

In this setup, the system is sheared by pulling a spring attached to the upper plate at a constant velocity. Consequently, the resulting pulling force applied on the upper plate increase linearly with time. The frictional force and sliding velocity as a function of time for different elastic modulus is shown in Figure 4.7.

The sliding behavior varies with the spring constant used. At the highest spring constant k=100, the pulling force is fluctuating in a wide range while the sliding velocity of the upper plate is stably fluctuating around 0.01, in accordance with the pulling velocity of the spring. For the lowest spring constant k=0.1, the pulling force first increases linearly with step and then experience stick-slip motion throughout the following period. The fluctuating frictional force falls in a specific range bounded by the higher static yield stress and the lower dynamic yield stress. During the stick-slip motion, each stress drop correspond to a sudden increase in the sliding velocity of the upper plate.

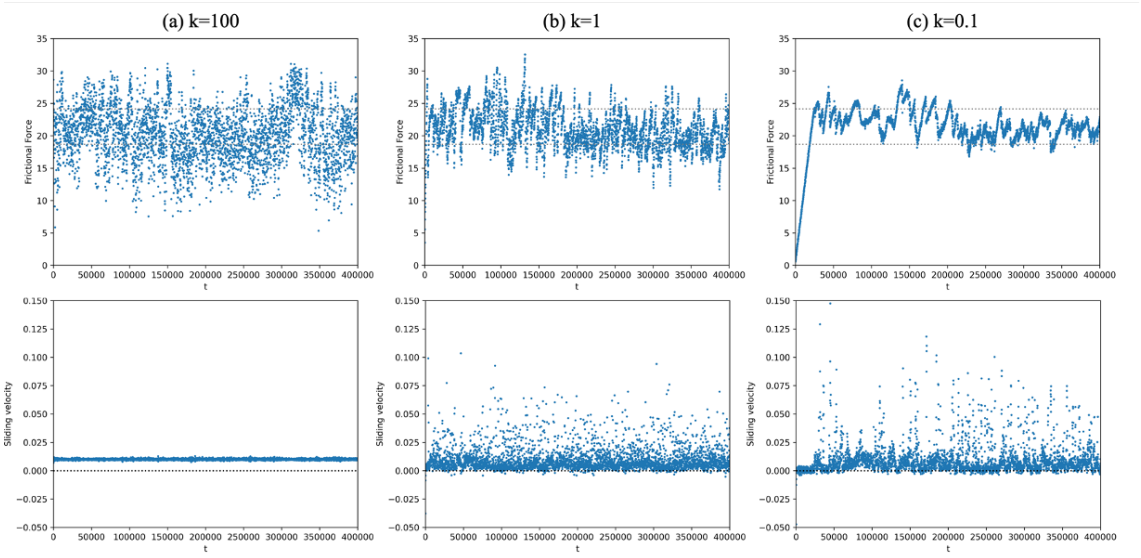

Figure 4.7: Frictional force in X direction (top row) and sliding velocity (bottom row) of the upper plate when the load force is applied by pulling a spring with spring constant (a) 100, (b) 1, and (c) 0.1 at a constant velocity of 0.01. For low spring constant (b, c), the frictional force fluctuates in the range close to the higher static yield stress and lower dynamic yield stress (grey dotted line in frictional force). The velocity fluctuates around 0.01 (the pulling velocity of spring) for high spring constant (a) and become unstable for low spring constant (b, c, d). The black dotted line corresponds to sliding velocity of 0.

Two extended simulations are conducted for spring constants k=0.1 and k=0.01, as shown in Figure 4.8. The values are time averaged every 500t. The peaks and valleys in frictional force F_{t1} are identified as local maxima and minima within the bin $\{F_{t1-m}, F_{t1-m+1}, \cdots, F_{t1}, \cdots F_{t1+m}\}$ after the fluctuation is averaged over time. We use m=5 for k=0.1 and m=50 for k=0.01, resulting in bin sizes of 11 and 101, respectively. The identified peaks and valleys in force are marked in red and black, respectively. The choice of bin size may influence the determination of peaks and valleys in stick-slip motion, and is discussed in Appendix 4-A.

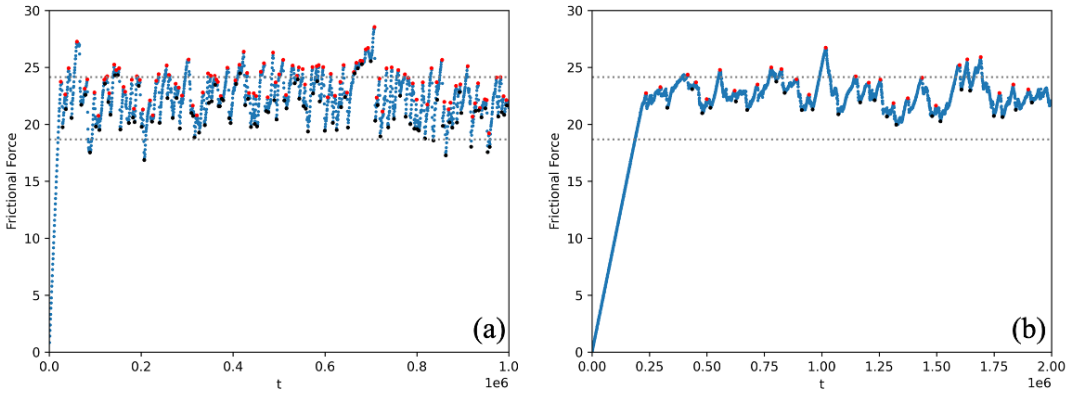

Figure 4.8: Frictional force experienced by the upper plate when the load force is applied by pulling a spring with spring constant (a) 0.1, (b) 0.01 at a constant velocity of 0.01. The dynamic and static yield stress are shown in grey dotted lines. The identified force peaks and valleys are marked in red and black, respectively.

Figure 4.9 compares the change in force, system height and sliding velocity in the time window t = 1×10^6 ~1.25×10^6 with spring constant k=0.01. Three slip events can be identified in the presented range, where a drop in pulling force corresponds to a decrease in system height and larger sliding velocity. However, change in system height are also observed between events with no clear unstable slip. Noted that the fluctuations in system height are generally smaller than 1, corresponding to the thickness of one particle.

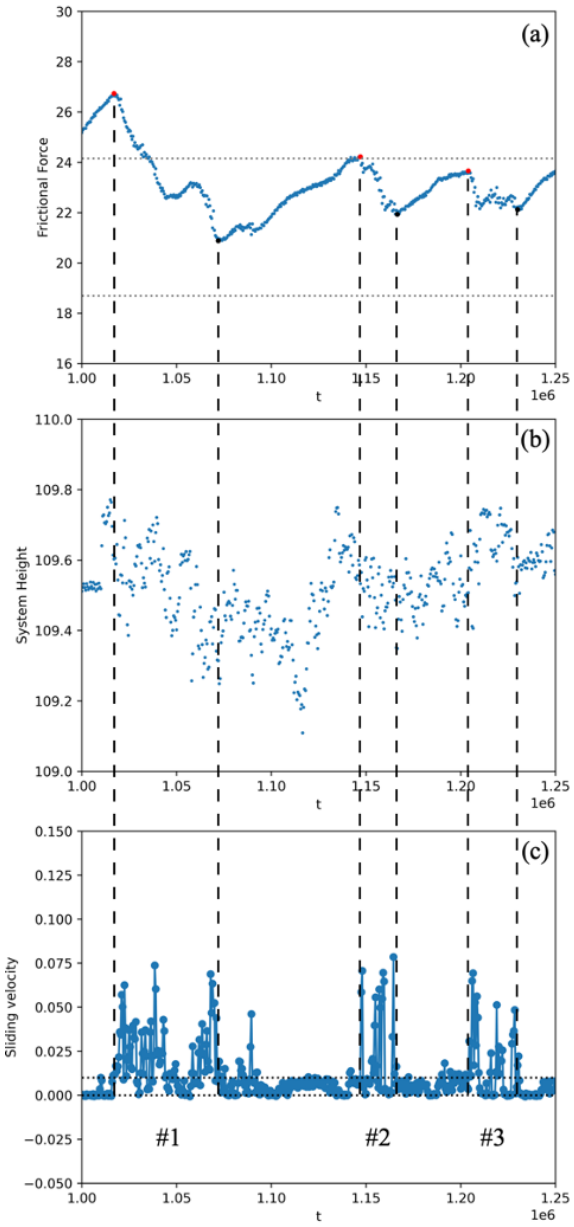

Figure 4.9: Zoomed view of (a) friction force, (b) system height, and (c) sliding velocity evolution during stick-slip motion in time window t = 1×10^6 ~1.25×10^6 with spring constant k=0.01. Three slip events can be identified with vertical dashed lines corresponding to the peak and valley in frictional force. The grey dotted lines in (a) correspond to static and dynamics yield stresses. The black dotted line in (c) corresponds to the velocity of 0 and the spring pulling velocity of 0.01.

The force drops and time duration of each slip event are defined as the differences in force and time between the corresponding force valley and the preceding force peak. Average values

are summarized in Table 4-2. The average peak forces are 23.754 for k=0.1 and 23.790 for k=0.01, close to the previous measured static yield force of 23.1. The resulting average peak stress is near 4 MPa. The average stress drop slightly decreases from 0.46 to 0.38 MPa at lower spring constant, suggesting that the stress drop ins not strictly the gap between the dynamic and static yield stress. The average duration increases from 3087 to 23870.

Spring constant k	Peak stress	Stress drop	Duration
0.1	4.01 MPa	0.46 MPa	3087
0.01	4.02 MPa	0.38 MPa	23870

Table 4-2 The average values of peak stress, stress drop and duration of slip events measured during stick-slip motion with spring constant 0.1 and 0.01.

4.3.3.2 Effect of normal stress

Shear configurations at different normal stresses at $t=2\times10^5$ are shown in Figure 4.10. The color represents the initial x coordinate of the clay particles before shear. At normal stress of 3.55 MPa, the system exhibits typical wall slip behavior with shear localized near the upper plate. At the normal stress of 17.74 MPa, the shear zone become wider, with particles near the lower plate being less affected. At the normal stress of 35.48 MPa, the shear permeates the entire system height.

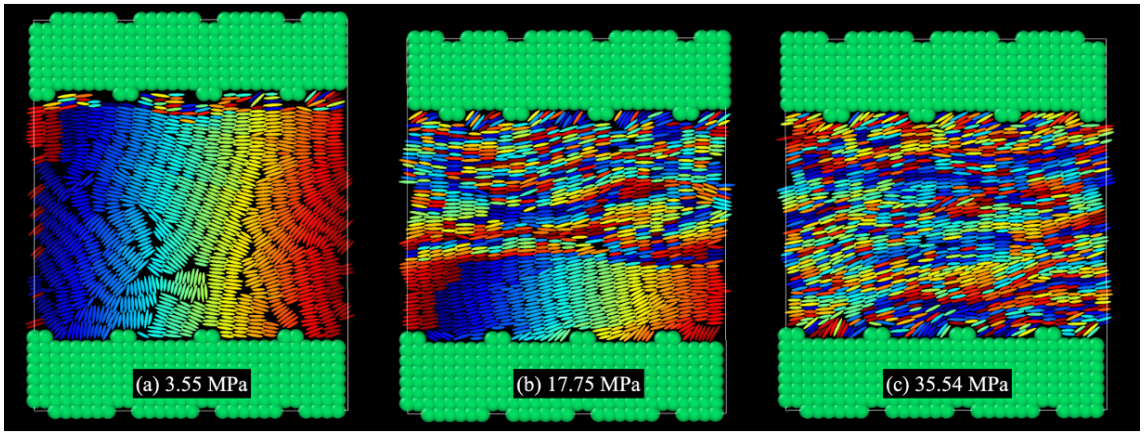

Figure 4.10: Shear configurations after shear for $t=2\times10^5$ at normal stress (a) 3.55 MPa, (b) 17.75 MPa, and (c) 35.54 MPa. The upper plate is pulling with a spring (k=0.1) at constant velocity 0.01. The color represents the initial x coordinate of the clay particles before shear. The shear is localized close to the upper plate (wall slip) at low normal stress and the shear zone become wider at higher normal stress.

The effect of normal stress on slip events are shown in Figure 4.11. The average peak stress

increases with normal stress. The average stress drop generally decreases, and the duration of slip events increases at higher normal stress.

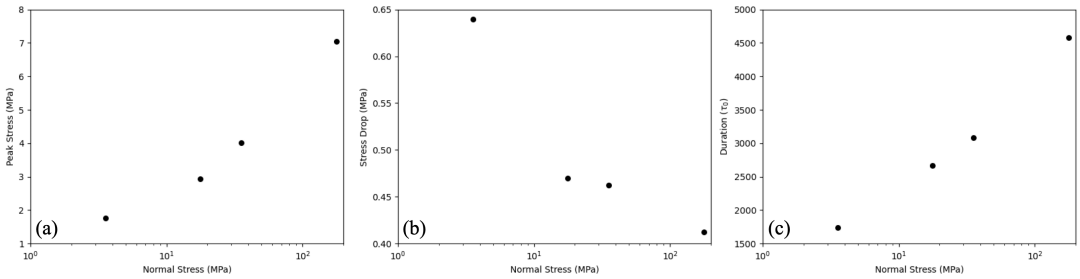

Figure 4.11: Average values of peak stress, stress drop and duration of slip events as a function of normal stress during stick-slip motion with spring constant 0.1.

4.4 Discussion

4.4.1 Comparison with bulk shear

The results from Chapter 2, using the same energy ratio 1/8-1/10-1/12 indicate a yield stress near 3 MPa under normal stress in the range 16.03~48.09 MPa. The yield force of 18.7 from pulling tests gives a yield stress value of 3.15 MPa at the normal stress of 35.48 MPa, which is slightly higher than the estimated value from bulk shear. The exponent n of 0.7 is higher than the value of 0.3 obtained from Chapter 2, suggesting the shear stress is more sensitive to strain rate change in the confined system.

This discrepancy could be due the assumed background Couette flow in the bulk shear system. At high strain rate, the bulk system exhibits a linear velocity profile following the background flow. Figure 4.12 shows the normalized velocity profile during ramping average pulling force in the range from 0.15 to 0.3 in a confined system. The upper and lower four points indicate the range of the upper and lower plate, respectively. The shape of the velocity profile remains similar across different pulling forces. Flow is generally localized in the region close to the upper plate and the lower half exhibit near-zero velocity. The shear in the confined system have largely deviate from the homogeneous shear assumed in bulk system. although it differs from wall slip as particles still move with the plate.

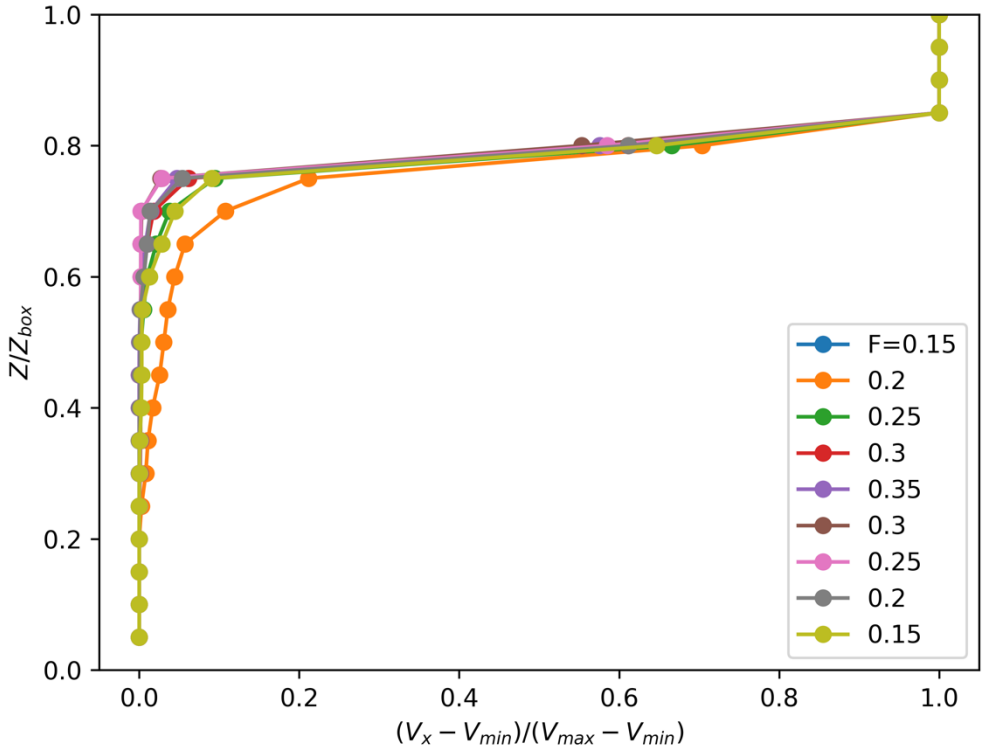

Figure 4.12: Normalized velocity profile with constant average force ramping in the range 0.15~0.35. The upper/lower four points correspond to the upper and lower plates in the confined system.

4.4.2 Comparison with different stick-slip phenomenon

Nanoscale stick-slip behavior has been observed for hydrated montmorillonite using full atomistic MD (Wei et al., 2021). The setup involved a close system with interlayer water confined by two plates with montmorillonite structure. The friction load fluctuated periodically at sliding velocity < 0.001 Å/fs. The slip distance in each stick-slip circle is generally consistent with the periodic atomic lattice of the montmorillonite plate. At higher sliding velocity, the fluctuation is negligible. A similar study suggests the stick-slip behavior is controlled by formation and breakage of hydrogen bound between confined water molecules (Abbassi et al., 2020). As detailed structure of the molecules are not presented in the current studies, the above mechanism cannot explain the repeating stick-slip motion in the confined GB system.

Stick-slip behavior is also observed in confined model glass Lennard-Jones systems when the plate is pulled at a constant low velocity (Varnik et al., 2003). The shear stress fluctuates within a range, with the static yield stress as the upper limit. Despite differences in the shear

application methods, these results align with the current study. The result indicates that the Herschel-Bulkley model cannot predict a higher static yield stress at zero strain rate and the instability occurred at low strain rates, including stick-slip motion and shear banding.

However, in the current model, stick-slip motion occurred at a large layer thickness (~50 particle thickness), whereas in the glass system it only appears when the sheared layer is a few particle diameters thick. Additionally, the model glass system exhibits linear velocity profile above the static yield stress, our current model continues to show localized shear above the static yield stress (Varnik et al., 2003).

4.4.3 Possible cause of unstable shear

4.4.3.1 Non-monotonic flow curve based on thixotropy

Shear instability such as stick-slip and shear localization occur at low strain rate in the GB system, consistent with observations from various yield stress materials (Bonn et al., 2017). The instability at low strain rates contradicts with the assumption of homogeneous shear and stable viscosity in steady state as assumed in simple rheology models such as the HB model.

One explanation for yield stress involves thixotropy, where aging and shear rejuvenation affect the system's microstructure (Møller et al., 2006). The degree of microstructure formed in the system is described by a single structural parameter λ, which increases with time (aging) and can be destructed by shear (rejuvenation). In the simplest form, the time evolution of λ can be written as:

$$\frac{d\lambda}{dt} = \frac{1}{\tau_s} - \alpha\lambda\dot{\gamma} \tag{4.2}$$

where τ_s is the characteristic time for microstructure build-up, and α is a constant.

We also consider the viscosity η increases with λ, the shear stress is then:

$$\sigma = \eta\dot{y}, \eta = \eta_0(1 + \beta\lambda^n) \tag{4.3}$$

where β and $n > 0$ are constants. At steady state ($\frac{d\lambda}{dt} = 0$), λ reaches a constant value with $\lambda = \frac{1}{\alpha\tau_s\dot{\gamma}}$, and the resulting steady-state shear stress is:

$$\sigma_{ss} = \eta_0(1 + \beta(\alpha\tau_s\dot{\gamma})^{-n})\dot{y} = \eta_0\dot{y} + \eta_0\beta(\alpha\tau_s)^{-n}\dot{\gamma}^{1-n} \tag{4.4}$$

For sufficiently high strain rates, the system behaves as a Newtonian fluid:

$$\sigma_{ss} = \eta_0\dot{y} \tag{4.5}$$

At low strain rates, the shear stress follows:

$$\sigma_{ss} \propto \dot{\gamma}^{1-n} \tag{4.6}$$

For $0 < n < 1$, shear stress monotonically increases with strain rate without showing a yield

stress. When $n > 1$, shear stress shows a negative strain rate dependence on at low strain rate end and a critical yield stress occurs. An example flow curve is given for $\sigma_{ss} = \dot{y} + 0.1 * \dot{\gamma}^{-0.3}$, with $\eta_0 = 1$ and n=1.3 (Figure 4.13). The steady state flow curve shows a minimum critical stress below which no flow occurs. A critical strain rate can also be defined where smaller strain rate gives a negative slope and correspond to negative viscosity and unstable flow.

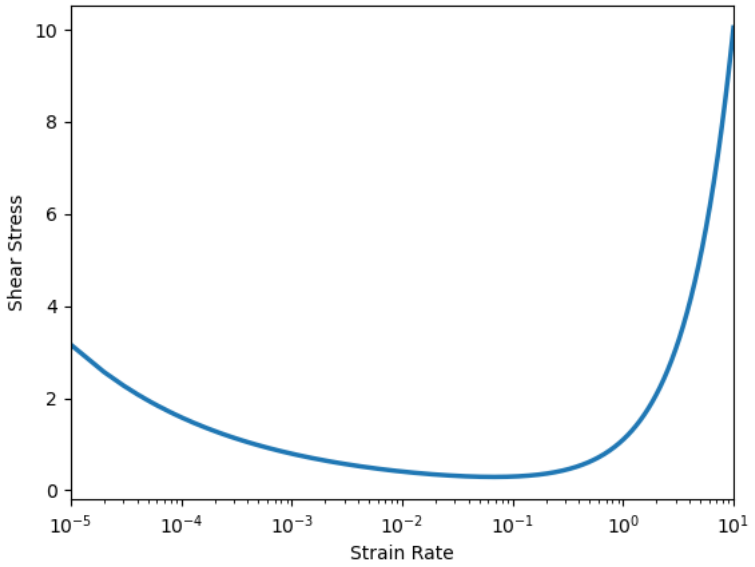

Figure 4.13: Example flow curve of $\sigma_{ss} = \dot{y} + 0.1 * \dot{\gamma}^{-0.3}$ based on thixotropy.

This model partially explained the challenges in yield stress measurement by linking it to the structure parameter λ, which depends on the previous shear history of the material. The negative slope of the non-monotonic flow curve at low strain rates correspond to the existence of shear banding and stick-slip and is in qualitative agreement with some experimental observations (Coussot et al., 2002; Møller et al., 2008).

4.4.3.1 Static and dynamic yield stress

The above model predicts unstable flow on the negative branch of flow curve at low strain rates. Yet this negative slope is not consistently observed for some systems (Varnik et al., 2003; Chaudhuri et al., 2012). Chapter 2 and 3 also show the global flow curve can still be described by the Herschel-Bulkley model even for strain rate as low as 10^{-3} and 10^{-4}. Moreover, the non-monotonic flow curve cannot cover the shear localization and fluctuating velocity profile on the positive branch from previous Chapter 2 and Chapter 3. Additionally, the above model does not explain the shear-thinning nature in the HB model and only predicts the Newtonian behavior at high strain rates.

A simpler scenario proposed by Berthier (2003) describes a monotonic flow curve with a finite dynamic yields stress coexists with a static branch for stress lower than a static yield stress:

$$\begin{gathered} \dot{\gamma} = 0 : \sigma \in [0, \sigma_y^s] \\ \dot{\gamma} > 0 : \sigma = \sigma_y + K\dot{\gamma}^n \\ (\sigma_y < \sigma_y^s) \end{gathered} \tag{4.7}$$

where the static yield stress σ_y^s is higher than the dynamic yield stress σ_y. The strain rate is bivalued in the shear stress range between the static yield stress and the dynamic yield stress $\sigma \in [\sigma_y, \sigma_y^s]$. This explains the separation of a flow phase and an arrested phase at low strain rate observed in model glass system (Varnik et al., 2003). Despite the discrepancy mentioned in Section 4.4.2, this scenario aligns with findings in the current study.

In the context of a pulling spring, the system initially climbs on the static branch during stick phase. When the applied force exceeds the static yield force, the system suddenly slips. The force required to flow drop to a lower value (higher than the dynamic yield force). We assume the static yield force in each stick-slip circle may depends on the local microstructure. After each slip phase, the force begins to accumulate with a different local structure. Thus, the force peak for each stick phase is not a constant value but fluctuates within the range between the static and dynamic yield forces.

It is important to note that while several models have been proposed to include the unstable regime in the flow curve, the physical origin at microscopic level remain incompletely understood, including the timescales of microstructure evolution and its controlling factors (Bonn et al., 2017; Coussot and Ovarlez, 2010). On the other hand, precise measurement of static yield stress and dynamic yield stress can also be difficult (Xu and O'Hern, 2006; Peyneau and Roux, 2008). More work is needed to achieve a comprehensive understanding of various unstable flow behaviors.

4.4.4 Comparison to shear experiment

Clay gouges are generally sheared at sliding velocities of μm/s level in friction experiments, exhibiting velocity-strengthening behavior. When clay is described as a yield stress material, instability occurs only at low strain rates, with corresponding stress close to the static yield stress. Shear experiments conducted at μm/s level velocities are likely in the stable region on the dynamic branch, whereas detecting instability requires even lower sliding velocity. Ikari (2019) conducted shear experiments on clay-rich samples at velocities comparable to tectonic plate driven rates (cm/yr). They observed slow slip resulting from intermediate instability, which may be seen as a laboratory counterpart to slow slip events, a type of slow earthquake.

A recent experimental study on wet montmorillonite observed frictional instability at a

sliding velocity of 0.1 μm/s (Volpe et al., 2024). The sample showed stick-slip motion at low normal stress (5~50 MPa) and forcing velocity, together with global rate-strengthening behavior (positive (a-b)). The largest stress drop, about 40 kPa, occurred at s normal stress of 12.5 MPa. The stress drop generally decreases at both smaller and larger normal stresses. At a normal stress of 100 MPa, stick-slip motion is not observed. Image analysis of the microstructure and stress suggests that the slip is driven by the structural and stress heterogeneities in thin shear zones close to the upper plate. At higher normal stress, the shear zone become thicker with shear distributed throughout the sample.

The boundary-driven model system also shows stick-slip motion with global rate-strengthening behavior, consistent with experimental results. Slip instability is observed for normal stress in the range 3.55~177.4 MPa, with the stress drop decreasing as normal stress increases. While stress drop approaches zero at 100 MPa in experiments, the decrease in the simulation is less obvious with stress drop still close to 400 kPa at 177.4 MPa (Figure 4.11). The largest stress drop observed in experiments is about 40 kPa, similar to the stress drop in some shallow slow slip events (Shreedharan et al., 2023). The stress drop in the simulation is about 400~600 kPa, which is ten times higher than in experiments. This may be due to the large spring constant (~1×10^4 MPa/mm) and sliding velocity (~0.26 m/s) used in the model system, whereas the stiffness of the loading system in the experiment is 2.96 MPa/mm and the sliding velocity is 0.1 μm/s. Our result shows lower stress drop can be achieved by using a lower spring constant.

Regarding system structure, the simulation shows wall slip at low normal stress, with shear restricted to a thin region close to the upper plate, and the sheared zone become wider at high normal stress (Figure 4.10). The result is in good alignment with experimental observations. The localization at low normal stress contrasts with the trend observed in bulk shear in previous chapters and may be due to the way shear is applied. In the bulk system, the shear is driven by a background at a relatively high strain rate range, whereas shear is driven by the movement of the upper plate in a confined system.

4.5 Conclusion

We investigated the yield stress and stability of a confined GB system with shear applied by loading force on the upper plate. The system cannot flow below a static yield force and experience unstable flow for force slightly above the critical value. A dynamic yield force, slightly lower than the static yield force, can be estimated from stable sliding region at higher applied forces.

When the force is applied through a spring, the upper plate experienced stick-slip motion. The results indicate that the GB system has the potential to generate shear instability under

boundary-driven shear configurations. While the Herschel-Bulkley model effectively captures rate-strengthening behavior at high strain rate end, it fails to account for the instability during shear startup and at low strain rates. The model based on static and dynamic yield stress provides a qualitative explanation for the observed stick-slip motion when pulling with the spring.

Increasing normal stress results in a lower stress drop and longer slip duration, while a lower spring constant result in a similar peak stress with a smaller stress drop and longer slip duration. At low normal stress, shear is localized near the upper plate, and the shear zone become wider as the normal stress increases. The results on shear instability and localized shear zone align with experimental studies on wet montmorillonite under low normal stress and sliding velocity conditions.

Appendix 4-A Effect of bin size on stress drop and duration of slip event

The peaks and valleys of force are determined by identifying the local maximum and minimum within a bin size of 2m+1. Both the average stress drop and the average duration of slip events increase with m (Figure 4.14). Determining an appropriate bin size can be difficult in the current system. A large bin size may overlook changes over short durations, while a small bin size may be affected by local fluctuations. For consistency, m=5 is used for all systems with a spring constant of k=0.1, and m=50 is used for system with k=0.01, as the increase in force is ten times slower. These parameters generally capture the position of the force peak and valley during stick-slip motion (Figure 4.8 and Figure 4.9).

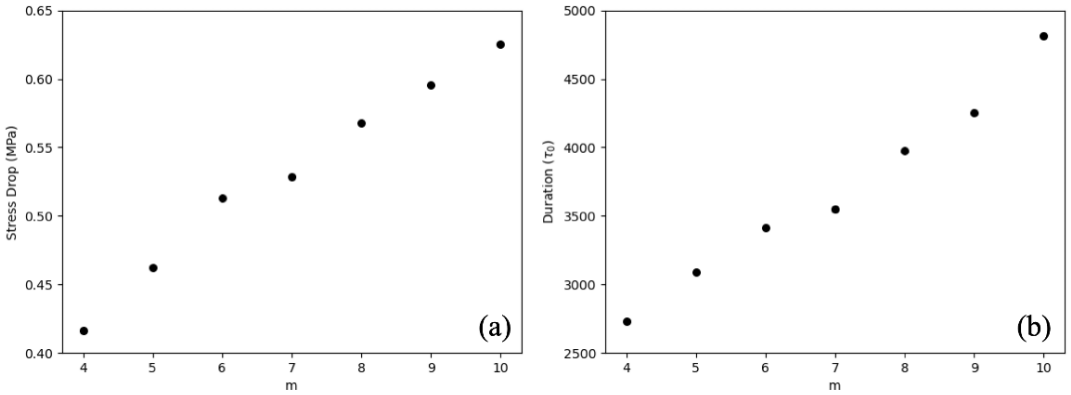

Figure 4.14: Change in average stress drop and average slip duration at different m values.

5 General discussion

5.1 Implications on natural fault

5.1.1 Shear localization

Shear bands are observed at low strain rates during shear. With the "low" strain rate in our simulations being higher than typical experimental values, this implies that shear bands should be ubiquitous in natural smectite clay, irrespective of their velocity-strengthening friction. This idea is supported by shear experiments showing a tendency for shear banding in clay gouges (Moore and Lockner, 2007; Haines et al., 2013). The thickness of the shear bands formed in our simulations is comparable to the size of a single particle, typically tens of nanometers. While measuring shear band thickness in practice is challenging, experiments on clay-rich gouges have shown smooth boundary layers of sub-micron thickness with particles perfectly parallel to the shear surface (Haines et al., 2013). Saturated montmorillonite samples exhibit sharp, polished, planar surfaces even for Riedel shear, which accommodates a small amount of strain (Moore and Lockner, 2007). This may suggest that shear band thickness in experiments can be as small as the size of a single particle.

Given the high strain rates in our simulations, shear is likely predominantly controlled by localized shear bands at realistic strain rates in natural clay-rich faults. Shear experiments performed at μ m/s sliding velocities are likely on the dynamic branch of the flow curve, where shear bands coexist with global velocity-strengthening friction. The emergence of inhomogeneous shear is inherently a sign of unstable flow at low strain rate conditions.

5.1.2 Fluctuating velocity profile

Our results indicate that shear processes are controlled by cluster movement at low effective normal stress with low particle alignment. This cluster structure persists after prolonged strain but will eventually be replaced by a highly aligned, dense structure at high normal stress with increasing depth. Previous friction experiments suggest high alignment of clay minerals corresponds to the concept of "contact saturation", where mineral surfaces are nearly in complete contact, and real contact does not evolve with changes in velocity (Ikari et al., 2007; Saffer and Marone, 2003). Contact saturation is consistent with the experimental observation of the frictional parameter b being close to 0, indicating that smectite clay is inherently velocity strengthening with (a-b)>0. However, our simulation results suggest that unstable flow can persist at high particle alignment, where multiple possible shear bands may result in long-lived fluctuations in the velocity profile. This is likely to occur when multiple fabrics become throughgoing and well developed with accumulated shear strain in clay-rich faults

(Kenigsberg et al., 2019).

5.1.3 Stick-slip motion

Finally, we confirmed that the model clay system can exhibit stick-slip motion at boundary-driven conditions. Stick-slip motion in smectite gouge may only be observed at sliding velocities much lower than the μm/s driven rate in conventional friction experiments (Ikari, 2019). Our results suggest that smectite may inherently exhibit instability at very low driven rates and should be considered for natural clay-rich gouge at low temperature, low depth condition (Volpe et al., 2024). Other processes, such as gouge lithification and the introduction of material heterogeneity, may also become important with increasing temperature at greater depths (Ikari et al., 2009; Marone and Saffer, 2007).

Considering the low coefficient of friction, the strength of smectite-rich faults should be fundamentally controlled by the yield stress of the material, and should not be neglected (Kameda and Hamada, 2020). Stress changes in stick-slip motion may only fluctuate close to the static yield stress and the overall stress drop is low. This is supported by the extremely low stress drop of very low frequency earthquakes in the shallow part of the subduction zone (Ito and Obara, 2006). Recent studies suggest that the low stress drop and short recurrence time of slow slip events in shallow clay-rich regions may result from the low frictional healing rates of weak phyllosilicates (Shreedharan et al., 2023). More studies are needed to understand the characteristics of slip events in the model clay system and to associate them with slow earthquakes in natural fault zone systems.

5.2 Limitations of the model

5.2.1 Shape and interactions

Natural clay platelets have a much larger aspect ratio than those used in the present model. A typical size distribution (in diameter) of Na-montmorillonite ranges from 5 to 750 nm with an average of 250 nm (Michot et al. 2004). Consequently, this study primarily addresses the smaller end of the natural clay platelet size distribution. This limitation may lead to an underestimation of shear stress during the initial stage of shear, as the rearrangement and rotation of larger platelets are more difficult. A larger aspect ratio could result in more prevalent shear localization.

In terms of particle interaction, the Gay-Berne potential functions are adopted in this study with implicit solvent and ions. While calibrated from full atomistic MD simulation under equilibrium conditions, the Gay-Berne potential may not fully reflect the capture of dynamic shear (Ebrahimi et al., 2014). Dynamic shear can induce various structural changes, such as

the reduction of water interlayers, which would decrease lubricity and increase shear resistance (Moore and Lockner, 2007). Caution is needed when applying the Gay-Berne potential to other phyllosilicate minerals, as the interaction shape and bonding characteristics can be different.

5.2.2 Limitations in time and size

In general, MD simulations have inherent limitations in terms of time and length scales compared to real systems. The timescale limitation results in an unrealistically high strain rate (Ewen et al., 2018). The strain rates investigated in this study are therefore much higher than those in typical experiments, where the gouge thickness is a few mm and the loading rate is on the order of μ m/s. At sufficiently high strain rates, various thermal effects may occur such as thermal pressurization of pore fluid (Ujiie et al., 2013). These effects are not considered in the present simulation, where the temperature is kept constant during shear.

The system size in this study is limited to the nanometer scale. Previous experimental studies suggest that the formation of various fabrics and shear bands plays a key role in reducing the macroscopic frictional strength in clay-rich gouges (Haines et al., 2013; Collettini et al., 2019; Kenigsberg et al., 2019). Such large-scale fabrics cannot be formed in small simulation systems. Fabric formation also depends on the presence of larger and stronger minerals, such as quartz (Tesei et al., 2012; Collettini et al., 2019). Such mineral heterogeneity is not considered in the current system.

Since the computational cell in the present simulation is only tens of nanometers, it can be interpreted as a magnification of a region including a shear band in an experimental specimen or in a natural fault. The true strain rate at the shear band, estimated from experiments or natural faults, can be as large as 10^5 /s when the slip velocity is 1 mm/s, and the shear band thickness is 10 nm. Therefore, high strain rates in the present simulation may not be so unrealistic. In such a situation, the frictional heat may not be negligible as discussed above. However, at least in the present parameter range, the comparable (a-b) values with experiments may partially support the validity of the present simulation.

6 Summary and Future studies

6.1 Summary

Smectite clay is described as a low friction mineral with velocity-strengthening behavior, which typically does not generate earthquakes. However, when mixed with water, the clay-water mixture can exhibit thixotropic behavior as a yield stress fluid, potentially displaying instability. Fabric analysis reveals that shear in clay-rich gouge is governed by thin shear planes. This thesis aims to connect the diverse macroscopic behaviors of clay with their underlying particle-level mechanisms. We achieve this through molecular dynamics simulations of a simple model clay system composed of ellipsoid particles interacting via the Gay-Berne potential. Our model successfully reproduces key features of the clay system in terms of rheology and structure, including unstable flow behaviors under various conditions.

In Chapter 2, our 3D clay system demonstrates velocity-strengthening behavior which can be effectively described by the Herschel-Bulkley model. We observed shear banding at low strain rates, where particles within the shear zone aligned in a preferred orientation. This suggests that clay-rich faults are predominantly controlled by thin shear bands under realistic strain rates. Structural analysis quantifies the development of the system using nematic order and parallel radial distribution function. We find that at low strain rates, the shear process involves two stages: 1) Particle rearrangement to align with shear when the shear stress increases to the maximum value. 2) Shear banding occurs when the shear stress decreases to the steady-state value. These findings are consistent with the experimental observations.

In Chapter 3, we show the 2D clay system under high normal stress shows similar structural and rheological characteristics to the 3D system. However, at low normal stress, shear is characterized by collective cluster movements leading to significant fluctuations in volume and particle alignment. Stable shear bands occur at much lower strain rate in the 2D system, with intermediate strain rates governed by long-lived, fluctuating nonlinear velocity profiles. We demonstrate that increased energy anisotropy enhances shear resistance while promoting cluster formation.

In Chapter 4, we investigate the instability of a confined 2D clay system with a moving upper plate. The system exhibits stick-slip motion when the upper plate is pulled with a spring that has a sufficiently low spring constant. The stress during stick-slip fluctuates close to the static yield stress. Increasing normal stress results in a lower stress drop and longer slip duration. At low normal stress, shear is localized near the upper plate, and the shear zone becomes wider as the normal stress increases.

Our findings suggest the typical characteristics of clay gouge, including velocity strengthening behavior and fabric development, can be captured effectively by our simple

model clay system. We argue that the shear behavior of model clay can be described using a yield stress fluid model, alongside conventional considerations of sliding friction. Despite the monotonic global flow curve indicating that the shear stress increases with finite strain rates, the clay system can display instability, including shear banding and stick-slip motion at low strain rates and during shear startup.

6.2 Future studies

6.2.1 More realistic mineral-water system in a wide range of water content

The current study assumes rigid particles with small aspect ratios. However, real clay particles can deform and bend elastically and have much larger aspect ratios (Mouzon et al., 2016). Future research should investigate the effect of particle size and deformability on the fabric evolution and instability in clay systems. In natural fault zones, clays are often mixed with other minerals like quartz (Bedford et al., 2022). It is crucial to determine whether integrating our model with previous studies on granular materials can provide deeper insights into these mixed systems.

Additionally, the role of water was considered primarily through the Gay-Berne potential and background Couette flow in bulk shear. Incorporating hydraulic effects for non-spherical particles can bridge the gap between our findings at high volume fractions and those observed at low volume fractions (Yamamoto et al., 2005; Marschall et al., 2020). Since unstable flow in dilute clay suspension can be elucidated within the framework of aging and shear rejuvenation of microstructure, further studies are needed to unify our understanding of unstable flow in the clay-water systems across varying volume fractions (Pignon et al., 1996).

6.2.2 Further understand of unstable flow for different anisotropy and adhesion.

The Gay-Berne potential introduces shape and energy anisotropy based on the isotropic Lennard-Jones (LJ) potential. Previous simulation studies on unstable flow mainly focus on isotropic potential such as those in model glassy systems (Varnik et al., 2003). The current model, with aspect ratios near 1/5, reproduced similar shear band and stick-slip motion at low strain rates. It is crucial to investigate how anisotropy in shape and potential affects shear band formation and the yielding process. Further examination of microstructural change can provide insights into both yield stress and the shear-thinning behavior of yield stress materials (Oyama et al., 2021). Chaudhuri et al. (2012) suggests that discontinuities in flow curves are associated with particle adhesion. Exploring particle systems with tunable adhesion can deepen our understanding of unstable flow behaviors in diverse particle systems.

Reference

Aminpour, P., & Sjoblom, K. J. (2019). Multi-scale modelling of kaolinite triaxial behaviour. *Géotechnique Letters*, *9*(3), 178-185.

Anderson, E. M. (1905). The dynamics of faulting. *Transactions of the Edinburgh Geological Society*, 8(3), 387-402.

Asadi, F., Zhu, H. X., Vandamme, M., Roux, J. N., & Brochard, L. (2022). A meso-scale model of clay matrix: the role of hydration transitions in geomechanical behavior. *Soft Matter*, *18*(41), 7931-7948.

Ashman, I. R., & Faulkner, D. R. (2023). The effect of clay content on the dilatancy and frictional properties of fault gouge. *Journal of Geophysical Research: Solid Earth*, *128*(4), e2022JB025878.

Baille, W., Tripathy, S., & Schanz, T. (2010). Swelling pressures and one-dimensional compressibility behaviour of bentonite at large pressures. *Applied Clay Science*, *48*(3), 324-333.

Bandera, S., O'Sullivan, C., Tangney, P., & Angioletti-Uberti, S. (2021). Coarse-grained molecular dynamics simulations of clay compression. *Computers and Geotechnics*, *138*, 104333.

Bayesteh, H., & Hoseini, A. (2021). Effect of mechanical and electro-chemical contacts on the particle orientation of clay minerals during swelling and sedimentation: A DEM simulation. *Computers and Geotechnics*, *130*, 103913.

Bedford, J. D., Faulkner, D. R., & Lapusta, N. (2022). Fault rock heterogeneity can produce fault weakness and reduce fault stability. *Nature Communications*, *13*(1), 326.

Behnsen, J., & Faulkner, D. R. (2012). The effect of mineralogy and effective normal stress on frictional strength of sheet silicates. *Journal of Structural Geology*, *42*, 49-61.

Behnsen, J., & Faulkner, D. R. (2013). Permeability and frictional strength of cation‐exchanged montmorillonite. *Journal of Geophysical Research: Solid Earth*, *118*(6), 2788-2798.

Berthier, L. (2003). Yield stress, heterogeneities and activated processes in soft glassy materials1. *Journal of Physics: Condensed Matter*, *15*(11), S933.

Bird, P. (1984). Hydration-phase diagrams and friction of montmorillonite under laboratory and geologic conditions, with implications for shale compaction, slope stability, and strength of fault gouge. *Tectonophysics*, *107*(3-4), 235-260.

Bonn, D., Denn, M. M., Berthier, L., Divoux, T., & Manneville, S. (2017). Yield stress materials in soft condensed matter. *Reviews of Modern Physics*, *89*(3), 035005.

Börzsönyi, T., Szabó, B., Wegner, S., Harth, K., Török, J., Somfai, E., ... & Stannarius, R. (2012). Shear-induced alignment and dynamics of elongated granular particles. *Physical Review E*, *86*(5), 051304.

Boukpeti, N., White, D. J., Randolph, M. F., & Low, H. E. (2012). Strength of fine-grained soils at the solid–fluid transition. *Géotechnique*, *62*(3), 213-226.

Brace, W. F., & Byerlee, J. D. (1966, September). Recent experimental studies of brittle fracture of rocks. In *ARMA US Rock Mechanics/Geomechanics Symposium* (pp. ARMA-66). ARMA.

Brown, K. M., A. Kopf, M. B. Underwood, and J. L. Weinberger (2003), Compositional and fluid pressure controls on the state of stress on the Nankai subduction thrust: A weak plate boundary, Earth Planet. Sci. Lett., 214, 589–603.

Brown, W. M., Petersen, M. K., Plimpton, S. J., & Grest, G. S. (2009). Liquid crystal nanodroplets in solution. *The Journal of chemical physics*, *130*(4).

Busselez, R., Cerclier, C. V., Ndao, M., Ghoufi, A., Lefort, R., & Morineau, D. (2014). Discotic columnar liquid crystal studied in the bulk and nanoconfined states by molecular dynamics simulation. *The Journal of Chemical Physics*, *141*(13).

Byerlee, J. (1978). Friction of rocks. Rock friction and earthquake prediction, 615-626.

Cadene, A., Durand-Vidal, S., Turq, P., & Brendle, J. (2005). Study of individual Na-montmorillonite particles size, morphology, and apparent charge. *Journal of colloid and interface Science*, *285*(2), 719-730.

Caprion, D., Bellier-Castella, L., & Ryckaert, J. P. (2003). Influence of shape and energy anisotropies on the phase diagram of discotic molecules. *Physical Review E*, *67*(4), 041703.

Carpenter, B. M., Marone, C., & Saffer, D. M. (2011). Weakness of the San Andreas Fault revealed by samples from the active fault zone. *Nature Geoscience*, *4*(4), 251-254.

Carrier, B. (2013). *Influence of water on the short-term and long-term mechanical properties of swelling clays: experiments on self-supporting films and molecular simulations* (Doctoral dissertation, Université Paris-Est).

Carroll, D., & Starkey, H. C. (1958, February). Effect of sea-water on clay minerals. In *Clays and Clay Minerals (National Conference on Clays and Clay Minerals)* (Vol. 7, pp. 80-101). Cambridge University Press & Assessment.

Caswell, T. A., Lee, A., Droettboom, M., de Andrade, E. S., Hoffmann, T., Klymak, J., et al. (2022). matplotlib/matplotlib: Rel: V3.6.1 (v3.6.1) [Software]. Zenodo. https://doi.org/10.5281/zenodo.7162185

Chaudhuri, P., Mansard, V., Colin, A., & Bocquet, L. (2012). Dynamical flow arrest in confined gravity driven flows of soft jammed particles. *Physical review letters*, *109*(3), 036001.

Chester, F. M., Rowe, C., Ujiie, K., Kirkpatrick, J., Regalla, C., Remitti, F., ... & Expedition 343 and 343T Scientists. (2013). Structure and composition of the plate-boundary slip zone for the 2011 Tohoku-Oki earthquake. *Science*, *342*(6163), 1208-1211.
Cienega-Cacerez, O., García-Alcántara, C., Moreno-Razo, J. A., Díaz-Herrera, E., & Sambriski, E. J. (2016). Induced stabilization of columnar phases in binary mixtures of discotic liquid crystals. *Soft Matter*, *12*(4), 1295-1312.
Cienega-Cacerez, O., Moreno-Razo, J. A., Díaz-Herrera, E., & Sambriski, E. J. (2014). Phase equilibria, fluid structure, and diffusivity of a discotic liquid crystal. *Soft Matter*, *10*(18), 3171-3182.
Clausius, R. (1870). XVI. On a mechanical theorem applicable to heat. *The London, Edinburgh, and Dublin Philosophical Magazine and Journal of Science*, *40*(265), 122-127.
Collettini, C., & Sibson, R. H. (2001). Normal faults, normal friction?. *Geology*, 29(10), 927-930.
Collettini, C., Tesei, T., Scuderi, M. M., Carpenter, B. M., & Viti, C. (2019). Beyond Byerlee friction, weak faults and implications for slip behavior. *Earth and Planetary Science Letters*, *519*, 245-263.
Coussaert, T., & Baus, M. (2002). Density-functional theory of the columnar phase of discotic Gay–Berne molecules. *The Journal of chemical physics*, *116*(17), 7744-7751.
Coussot, P., & Ovarlez, G. (2010). Physical origin of shear-banding in jammed systems. *The European Physical Journal E*, *33*, 183-188.
Coussot, P., & Proust, S. (1996). Slow, unconfined spreading of a mudflow. *Journal of Geophysical Research: Solid Earth*, *101*(B11), 25217-25229.
Coussot, P., Nguyen, Q. D., Huynh, H. T., & Bonn, D. (2002). Avalanche behavior in yield stress fluids. *Physical review letters*, *88*(17), 175501.
de Bono, J. P., & McDowell, G. R. (2022). Some important aspects of modelling clay platelet interactions using DEM. *Powder Technology*, *398*, 117056.
de Miguel, E., Martín del Rio, E., Brown, J. T., & Allen, M. P. (1996). Effect of the attractive interactions on the phase behavior of the Gay–Berne liquid crystal model. *The Journal of chemical physics*, *105*(10), 4234-4249.
Delhorme, M., Jönsson, B., & Labbez, C. (2014). Gel, glass and nematic states of plate-like particle suspensions: charge anisotropy and size effects. *RSC advances*, *4*(66), 34793-34800.
Deng, X., & Underwood, M. B. (2001). Abundance of smectite and the location of a plate-boundary fault, Barbados accretionary prism. *Geological Society of America Bulletin*, *113*(4), 495-507.

Derjaguin, B. V. (1941). Theory of the stability of strongly charged lyophobic sol and of the adhesion of strongly charged particles in solutions of electrolytes. *Acta phys. chim. URSS*, 14, 633.
Dieterich, J. H. (1978). Time-dependent friction and the mechanics of stick-slip. *Pure and Applied Geophysics*, 116, 790–806.
Dijkstra, M., Hansen, J. P., & Madden, P. A. (1995). Gelation of a clay colloid suspension. *Physical review letters*, *75*(11), 2236.
Divoux, T., Tamarii, D., Barentin, C., & Manneville, S. (2010). Transient shear banding in a simple yield stress fluid. *Physical review letters*, *104*(20), 208301.
Ebrahimi, D., Whittle, A. J., & Pellenq, R. J. M. (2014). Mesoscale properties of clay aggregates from potential of mean force representation of interactions between nanoplatelets. *The Journal of Chemical Physics*, *140*(15).
Ebrahimi, D., Whittle, A. J., & Pellenq, R. J. M. (2016). Effect of polydispersity of clay platelets on the aggregation and mechanical properties of clay at the mesoscale. *Clays and Clay Minerals*, 64(4), 425-437.
Emmerich, K., F. Wolters, G. Kahr, and G. Lagaly (2009), Clay profiling: The classification of montmorillonites, *Clays Clay Miner.*, 57, 104–114.
Evans, D.J., & Morriss, G.P. (2007). *Statistical mechanics of nonequilbrium liquids*. ANU Press.
Ewen, J. P., Heyes, D. M., & Dini, D. (2018). Advances in nonequilibrium molecular dynamics simulations of lubricants and additives. *Friction*, *6*, 349-386.
Faulkner, D. R., Lewis, A. C., & Rutter, E. H. (2003). On the internal structure and mechanics of large strike-slip fault zones: field observations of the Carboneras fault in southeastern Spain. *Tectonophysics*, *367*(3-4), 235-251.
Fulton, P. M., Brodsky, E. E., Kano, Y., Mori, J., Chester, F., Ishikawa, T., ... & Expedition 343, 343T, and KR13-08 Scientists. (2013). Low coseismic friction on the Tohoku-Oki fault determined from temperature measurements. *Science*, *342*(6163), 1214-1217.
Furukawa, Y., Watkins, J. L., Kim, J., Curry, K. J., & Bennett, R. H. (2009). Aggregation of montmorillonite and organic matter in aqueous media containing artificial seawater. *Geochemical transactions*, *10*, 1-11.
Gay, J. G., & Berne, B. J. (1981). Modification of the overlap potential to mimic a linear site–site potential. *The Journal of Chemical Physics, 74*(6), 3316-3319.
Gilbert, B., Comolli, L. R., Tinnacher, R. M., Kunz, M., & Banfield, J. F. (2015). Formation and restacking of disordered smectite osmotic hydrates. *Clays and Clay Minerals*, *63*(6), 432-442.

Gupta, V., Hampton, M. A., Stokes, J. R., Nguyen, A. V., & Miller, J. D. (2011). Particle interactions in kaolinite suspensions and corresponding aggregate structures. *Journal of Colloid and Interface Science*, *359*(1), 95-103.

Güven, N. (1992). Molecular aspects of clay-water interactions.

Haines, S. H., Kaproth, B., Marone, C., Saffer, D., & Van der Pluijm, B. (2013). Shear zones in clay-rich fault gouge: A laboratory study of fabric development and evolution. *Journal of Structural Geology*, *51*, 206-225.

Ho, T. A., Criscenti, L. J., & Greathouse, J. A. (2019). Revealing transition states during the hydration of clay minerals. *The journal of physical chemistry letters*, *10*(13), 3704-3709.

Hunter, J. D. (2007). Matplotlib: A 2D graphics environment. *Computing in Science and Engineering*, 9(3), 90–95.

Ide, S., Beroza, G. C., Shelly, D. R., & Uchide, T. (2007a). A scaling law for slow earthquakes. *Nature*, *447*(7140), 76-79.

Ikari, M. J., & Hüpers, A. (2021). Velocity-weakening friction induced by laboratory-controlled lithification. *Earth and Planetary Science Letters*, *554*, 116682.

Ikari, M. J., Saffer, D. M., & Marone, C. (2007). Effect of hydration state on the frictional properties of montmorillonite - based fault gouge. *Journal of Geophysical Research: Solid Earth*, *112*(B6).

Ikari, M. J., Saffer, D. M., & Marone, C. (2009). Frictional and hydrologic properties of clay - rich fault gouge. *Journal of Geophysical Research: Solid Earth*, *114*(B5).

Ikari, M. J., Marone, C., & Saffer, D. M. (2011). On the relation between fault strength and frictional stability. *Geology*, *39*(1), 83-86.

Ikeda, A., Berthier, L., & Sollich, P. (2013). Disentangling glass and jamming physics in the rheology of soft materials. *Soft Matter*, *9*(32), 7669-7683.

Ito, Y., & Obara, K. (2006). Very low frequency earthquakes within accretionary prisms are very low stress - drop earthquakes. *Geophysical Research Letters*, *33*(9).

Jeppson, T. N., & Tobin, H. J. (2015). San Andreas fault zone velocity structure at SAFOD at core, log, and seismic scales. *Journal of Geophysical Research: Solid Earth*, *120*(7), 4983-4997.

Kameda, J., Shimizu, M., Ujiie, K., Hirose, T., Ikari, M., Mori, J., ... & Kimura, G. (2015). Pelagic smectite as an important factor in tsunamigenic slip along the Japan Trench. *Geology*, *43*(2), 155-158.

Kameda, J., & Hamada, Y. (2022). Stick-slip behavior of a clayey crustal fault. *Physical Review Research*, *4*(1), 013211.

Kenigsberg, A. R., Rivière, J., Marone, C., & Saffer, D. M. (2019). The effects of shear strain, fabric, and porosity evolution on elastic and mechanical properties of clay - rich fault gouge. Journal of Geophysical Research: Solid Earth, 124, 10,968–10,982.
Kenigsberg, A. R., Rivière, J., Marone, C., & Saffer, D. M. (2020). Evolution of elastic and mechanical properties during fault shear: The roles of clay content, fabric development, and porosity. *Journal of Geophysical Research: Solid Earth*, *125*(3), e2019JB018612.
Kutter, S., Hansen, J. P., Sprik, M., & Boek, E. (2000). Structure and phase behavior of a model clay dispersion: A molecular-dynamics investigation. *The Journal of Chemical Physics*, *112*(1), 311-322.
Larson, R. G. (1999). *The structure and rheology of complex fluids* (Vol. 150). New York: Oxford university press.
Likos, W. J., & Lu, N. (2006). Pore-scale analysis of bulk volume change from crystalline interlayer swelling in Na+-and Ca2+-smectite. *Clays and Clay Minerals*, *54*(4), 515-528.
Lin, Z.-Y., Hatano, T. (2024). Rheology and Structure of Model Smectite Clay: Insights from Molecular Dynamics (Version 1.0) [Software]. Zenodo.
https://doi.org/10.5281/zenodo.10597892
Lockner, D. A., Morrow, C., Moore, D., & Hickman, S. (2011). Low strength of deep San Andreas fault gouge from SAFOD core. *Nature*, *472*(7341), 82-85.
Luckhurst, G. R., & Simmonds, P. S. J. (1993). Computer simulation studies of anisotropic systems: XXI. Parametrization of the Gay-Berne potential for model mesogens. *Molecular Physics*, *80*(2), 233-252.
Manga, M., & Bonini, M. (2012). Large historical eruptions at subaerial mud volcanoes, Italy. *Natural Hazards and Earth System Sciences*, *12*(11), 3377-3386.
Marcial, D., Delage, P., & Cui, Y. J. (2002). On the high stress compression of bentonites. *Canadian Geotechnical Journal*, *39*(4), 812-820.
Marone, C. (1998). Laboratory-derived friction laws and their application to seismic faulting, *Annual Review of Earth and Planetary Sciences*, 26, 643–696.
Marone, C., & Saffer, D. M. (2007). Fault friction and the upper transition from seismic to aseismic faulting. In *The seismogenic zone of subduction thrust faults* (pp. 346-369). Columbia University Press.
Marschall, T. A., Van Hoesen, D., & Teitel, S. (2020). Shear-driven flow of athermal, frictionless, spherocylinder suspensions in two dimensions: Particle rotations and orientational ordering. *Physical Review E, 101*(3), 032901.
Mitchell, J. K., & Soga, K. (2005). *Fundamentals of soil behavior* (Vol. 3, p. USA). New York: John Wiley & Sons.

Michot, L. J., Bihannic, I., Porsch, K., Maddi, S., Baravian, C., Mougel, J., & Levitz, P. (2004). Phase diagrams of Wyoming Na-montmorillonite clay. Influence of particle anisotropy. *Langmuir*, *20*(25), 10829-10837.
Møller, P. C., Mewis, J., & Bonn, D. (2006). Yield stress and thixotropy: on the difficulty of measuring yield stresses in practice. *Soft matter*, *2*(4), 274-283.
Møller, P. C. F., Rodts, S., Michels, M. A. J., & Bonn, D. (2008). Shear banding and yield stress in soft glassy materials. *Physical Review E—Statistical, Nonlinear, and Soft Matter Physics*, *77*(4), 041507.
Moore, D. E., & Lockner, D. A. (2007). Friction of the smectite clay montmorillonite: A review and interpretation of data. *The seismogenic zone of subduction thrust faults*, 317-345.
Morrow, C., B. Radney, and J. Byerlee (1992), Frictional strength and the effective pressure law of montmorillonite and illite clays, in Fault
Mechanisms and Transport Properties of Rocks, edited by B. Evans and T.-F. Wong, pp. 69–88, Elsevier, New York.
Morrow, C. A., Moore, D. E., & Lockner, D. A. (2017). Frictional strength of wet and dry montmorillonite. *Journal of Geophysical Research: Solid Earth*, *122*(5), 3392-3409.
Mouzon, J., Bhuiyan, I. U., & Hedlund, J. (2016). The structure of montmorillonite gels revealed by sequential cryo-XHR-SEM imaging. *Journal of Colloid and Interface Science*, *465*, 58-66.
Nadeau, P. H. (1985). The physical dimensions of fundamental clay particles. *Clay Minerals*, *20*(4), 499-514.
Nagy, D. B., Claudin, P., Börzsönyi, T., & Somfai, E. (2017). Rheology of dense granular flows for elongated particles. *Physical Review E*, *96*(6), 062903.
Niemeijer, A., Marone, C., & Elsworth, D. (2010). Fabric induced weakness of tectonic faults. *Geophysical Research Letters*, *37*(3).
Odriozola, G., Romero-Bastida, M., & Guevara-Rodriguez, F. D. J. (2004). Brownian dynamics simulations of Laponite colloid suspensions. *Physical Review E*, *70*(2), 021405.
Pagano, A. G., Magnanimo, V., Weinhart, T., & Tarantino, A. (2020). Exploring the micromechanics of non-active clays by way of virtual DEM experiments. *Géotechnique*, *70*(4), 303-316.
Okuda, H., Kitamura, M., Takahashi, M., & Yamaguchi, A. (2023). Frictional properties of the décollement in the shallow Nankai Trough: constraints from friction experiments simulating in-situ conditions and implications for the seismogenic zone. *Earth and Planetary Science Letters*, *621*, 118357.

Olsson, P., & Teitel, S. (2012). Herschel-Bulkley shearing rheology near the athermal jamming transition. *Physical review letters*, *109*(10), 108001.
Oyama, N., Mizuno, H., & Ikeda, A. (2021). Instantaneous normal modes reveal structural signatures for the herschel-bulkley rheology in sheared glasses. *Physical Review Letters*, *127*(10), 108003.
Paineau, E., Philippe, A. M., Antonova, K., Bihannic, I., Davidson, P., Dozov, I., ... & Michot, L. J. (2013). Liquid–crystalline properties of aqueous suspensions of natural clay nanosheets. *Liquid Crystals Reviews*, *1*(2), 110-126.
Pellenq, R. M., Caillol, J. M., & Delville, A. (1997). Electrostatic attraction between two charged surfaces: A (N, V, T) Monte Carlo simulation. *The Journal of Physical Chemistry B*, *101*(42), 8584-8594.
Perdigon-Aller, A. C., Aston, M., & Clarke, S. M. (2005). Preferred orientation in filtercakes of kaolinite. *Journal of colloid and interface science*, *290*(1), 155-165.
Perrin, G., Rice, J. R., & Zheng, G. (1995). Self-healing slip pulse on a frictional surface. *Journal of the Mechanics and Physics of Solids*, *43*(9), 1461-1495.
Peyneau, P. E., & Roux, J. N. (2008). Frictionless bead packs have macroscopic friction, but no dilatancy. *Physical Review E—Statistical, Nonlinear, and Soft Matter Physics*, *78*(1), 011307.
Pignon, F., Magnin, A., & Piau, J. M. (1996). Thixotropic colloidal suspensions and flow curves with minimum: Identification of flow regimes and rheometric consequences. *Journal of rheology*, *40*(4), 573-587.
Quirk, J. P. (1986). Soil permeability in relation to sodicity and salinity. *Philosophical Transactions of the Royal Society of London. Series A, Mathematical and Physical Sciences*, *316*(1537), 297-317.
Rabinowicz, E., & Mutis, A. (1965). Effect of abrasive particle size on wear. *Wear*, 8(5), 381-390.
Ragouilliaux, A., Herzhaft, B., Bertrand, F., & Coussot, P. (2006). Flow instability and shear localization in a drilling mud. *Rheologica acta*, *46*, 261-271.
Ren, Y., Yang, S., Andersen, K. H., Yang, Q., & Wang, Y. (2021). Thixotropy of soft clay: A review. *Engineering Geology*, *287*, 106097.
Ruina, A. (1983). Slip instability and state variable friction laws. *Journal of Geophysical Research*, 88(B12), 10359–10370.
Ruzicka, B., Zaccarelli, E., Zulian, L., Angelini, R., Sztucki, M., Moussaïd, A., ... & Sciortino, F. (2011). Observation of empty liquids and equilibrium gels in a colloidal clay. *Nature materials*, *10*(1), 56-60.

Saffer, D. M., & Marone, C. (2003). Comparison of smectite-and illite-rich gouge frictional properties: application to the updip limit of the seismogenic zone along subduction megathrusts. *Earth and Planetary Science Letters*, *215*(1-2), 219-235.
Schneider, T., & Stoll, E. (1978). Molecular-dynamics study of a three-dimensional one-component model for distortive phase transitions. *Physical Review B*, 17(3), 1302.
Sibson, R. H. (1985). A note on fault reactivation. *Journal of Structural Geology*, 7(6), 751-754.
Shen, X., & Bourg, I. C. (2021). Molecular dynamics simulations of the colloidal interaction between smectite clay nanoparticles in liquid water. *Journal of Colloid and Interface Science*, *584*, 610-621.
Shinoda, W., Shiga, M., & Mikami, M. (2004). Rapid estimation of elastic constants by molecular dynamics simulation under constant stress. *Physical Review B*, *69*(13), 134103.
Shreedharan, S., Saffer, D., Wallace, L. M., & Williams, C. (2023). Ultralow frictional healing explains recurring slow slip events. *Science*, *379*(6633), 712-717.
Skadsem, H. J., Leulseged, A., & Cayeux, E. (2019). Measurement of drilling fluid rheology and modeling of thixotropic behavior. *Applied Rheology*, *29*(1), 1-11.
Stukowski, A. (2009). Visualization and analysis of atomistic simulation data with OVITO–the Open Visualization Tool. *Modelling and simulation in materials science and engineering*, *18*(1), 015012.
Summers, R., & Byerlee, J. (1977, May). A note on the effect of fault gouge composition on the stability of frictional sliding. In *International Journal of Rock Mechanics and Mining Sciences & Geomechanics Abstracts* (Vol. 14, No. 3, pp. 155-160). Pergamon.
Takemura, S., Baba, S., Yabe, S., Emoto, K., Shiomi, K., & Matsuzawa, T. (2022). Source Characteristics and Along‐Strike Variations of Shallow Very Low Frequency Earthquake Swarms on the Nankai Trough Shallow Plate Boundary. *Geophysical Research Letters*, *49*(11), e2022GL097979.
Tembe, S., Lockner, D. A., & Wong, T. F. (2010). Effect of clay content and mineralogy on frictional sliding behavior of simulated gouges: Binary and ternary mixtures of quartz, illite, and montmorillonite. *Journal of Geophysical Research: Solid Earth*, *115*(B3).
Tesei, T., Collettini, C., Carpenter, B. M., Viti, C., & Marone, C. (2012). Frictional strength and healing behavior of phyllosilicate‐rich faults. *Journal of Geophysical Research: Solid Earth*, *117*(B9).
Thompson, A. P., Aktulga, H. M., Berger, R., Bolintineanu, D. S., Brown, W. M., Crozier, P. S., ... & Plimpton, S. J. (2022). LAMMPS-a flexible simulation tool for particle-based materials modeling at the atomic, meso, and continuum scales. *Computer Physics Communications*, *271*, 108171.

Thuresson, A., Jansson, M., Plivelic, T. S., & Skepö, M. (2017). Temperature response of charged colloidal particles by mixing counterions utilizing Ca2+/Na+ montmorillonite as model system. *The Journal of Physical Chemistry C*, *121*(14), 7951-7958.
Torikai, Y., Sato, S., & Ohashi, H. (1996). Thermodynamic properties of water in compacted sodium montmorillonite. *Nuclear technology*, *115*(1), 73-80.
Ueda, M., Ujiie, K., Takahashi, M. (2024). Geological and experimental investigations of slow slop in the Japan Trench subduction zone. *Abstracts of Japan Geoscience Union (JpGU) Meeting 2024.*
Ujiie, K., Tanaka, H., Saito, T., Tsutsumi, A., Mori, J. J., Kameda, J., ... & Expedition 343 and 343T Scientists. (2013). Low coseismic shear stress on the Tohoku-Oki megathrust determined from laboratory experiments. *Science*, *342*(6163), 1211-1214.
Underwood, T. R., & Bourg, I. C. (2020). Large-scale molecular dynamics simulation of the dehydration of a suspension of smectite clay nanoparticles. *The Journal of Physical Chemistry C*, *124*(6), 3702-3714.
Varnik, F., Bocquet, L., Barrat, J. L., & Berthier, L. (2003). Shear localization in a model glass. *Physical review letters*, *90*(9), 095702.
Verwey, E. J. W. (1947). Theory of the stability of lyophobic colloids. *The Journal of Physical Chemistry*, *51*(3), 631-636.
Vitek, V., & Egami, T. (1987). Atomic level stresses in solids and liquids. *physica status solidi (b)*, *144*(1), 145-156.
Volpe, G., Collettini, C., Taddeucci, J., Marone, C., & Pozzi, G. (2024). Frictional instabilities in clay illuminate the origin of slow earthquakes. *Science Advances*, *10*(26), eadn0869.
Wei, P. C., Zhang, L. L., Zheng, Y. Y., Diao, Q. F., Zhuang, D. Y., & Yin, Z. Y. (2021). Nanoscale friction characteristics of hydrated montmorillonites using molecular dynamics. *Applied Clay Science*, 210, 106155.
Wojatschke, J., Scuderi, M. M., Warr, L. N., Carpenter, B. M., Saffer, D., & Marone, C. (2016). Experimental constraints on the relationship between clay abundance, clay fabric, and frictional behavior for the C entral D eforming Z one of the S an A ndreas F ault. *Geochemistry, Geophysics, Geosystems*, *17*(10), 3865-3881.
Wu, F. T., Blatter, L., & Roberson, H. (1975). Clay gouges in the San Andreas fault system and their possible implications. *Earthquake Prediction and Rock Mechanics*, 87-95.
Xu, N., & O'Hern, C. S. (2006). Measurements of the yield stress in frictionless granular systems. *Physical Review E—Statistical, Nonlinear, and Soft Matter Physics*, *73*(6), 061303.

Yamamoto, T., Suga, T., & Mori, N. (2005). Brownian dynamics simulation of orientational behavior, flow-induced structure, and rheological properties of a suspension of oblate spheroid particles under simple shear. *Physical Review E*, *72*(2), 021509.
Yokota, Y., & Ishikawa, T. (2020). Shallow slow slip events along the Nankai Trough detected by GNSS-A. *Science Advances*, *6*(3), eaay5786.
Zaccarelli, E. (2007). Colloidal gels: Equilibrium and non-equilibrium routes. *Journal of Physics: Condensed Matter*, *19*(32), 323101.
Zhang, X. W., Kong, L. W., Yang, A. W., & Sayem, H. M. (2017). Thixotropic mechanism of clay: A microstructural investigation. *Soils and Foundations*, *57*(1), 23-35.
Zhu, H., Whittle, A. J., & Pellenq, R. J. M. (2022). Potential of mean force for face–face interactions between pairs of 2: 1 clay mineral platelets. *Langmuir*, *38*(43), 13065-13074.